





**Developing novel high strength 4xxx filler alloys for aluminum fusion welding of AA6xxx alloys**

**By**

**Mohamed Ahmed**

**Under the supervision of Prof. X.-Grant Chen and co-supervision of Prof. Mousa Javidani**

**Manuscript-Based Thesis presented to the University of Quebec at Chicoutimi with a view to obtaining the degree of Philosophie doctor (Ph. D.) in engineering.**

**Defended on 22 March 2024**

**Board of examiners:**

**Professor: Emad Elgallad**, Department of Applied Sciences at UQAC, President of the board of examiners,

**Professor: Ehab Elsharkawi**, Engineering, Saint Mary's University ,Halifax, External member of examiners

**Professor: X.-Grant Chen**, department of Applied Sciences at UQAC, Internal member of examiners

**Professor: Mousa Javidani**, Department of Applied Sciences at UQAC, Internal member of examiners

**Professor: Zhan Zhang**, Department of Applied Sciences at UQAC, Internal member of examiners

Québec, Canada

© Mohamed Ahmed, 2024

## Résumé

Les alliages d'aluminium sont utilisés dans de nombreuses applications et comme remplacements des pièces en acier en raison de sa résistance élevée au rapport de poids et de la résistance à la corrosion. Avec l'implantation des alliages d'aluminium dans de nombreuses utilisations industrielles, l'assemblage des différentes pièces pour former l'ensemble de l'assemblage et de la structure à haute résistance sont l'un des problèmes les plus cruciaux dans les applications industrielles telles que les automobiles, les avions et la construction navale. Les composants en aluminium, nécessitant souvent un assemblage, sont généralement soudés par fusion à l'aide de diverses techniques telles que le soudage à l'arc au gaz métallique (GMAW) et le gaz inerte au tungstène (TIG). Le soudage par fusion d'alliages à base d'aluminium traitables à la chaleur, en particulier les alliages 6xxx, présente plusieurs défis, notamment une résistance réduite dans la zone de fusion (FZ), une fissuration induite par soudage, une résistance mécanique réduite dans la zone affectée par la chaleur (HAZ), et une porosité accrue dans le métal de soudure. Ces questions sont liées à la chimie du métal d'apport, à la sensibilité à la fissuration et aux paramètres du procédé de soudage.

Dans la première partie, une étude a été menée sur la performance et la résistance mécanique des joints obtenus grâce à l'utilisation de métaux d'apport Al-Si-Mg récemment développés. Ces charges ont été caractérisées par des teneurs en Mg variant de 0,6 à 1,4 poids. %, et le processus de soudage impliquait un métal de base AA6061 (BM) de 2 mm d'épaisseur. Les résultats ont révélé que les métaux d'apport nouvellement développés ont une excellente soudabilité similaire à celle de l'ER4043. La teneur en Mg dans les ZE des nouvelles charges s'est avérée supérieure à celle de la charge de référence. Les joints soudés ont été fracturés à l'extérieur de la FZ, exactement dans la zone la plus molle de la ZAT montrant la même résistance mais inférieure à celle du BM. Le traitement thermique après soudage (PWHT) a enlevé la HAZ et a récupéré sa résistance. En outre, le PWHT conduit à la formation des précipités  $\beta''$ -MgSi cohérents qui ont porté la résistance des joints traités thermiquement au niveau du BM avec une efficacité de soudage de 100%. De plus, les zones de fusion étaient beaucoup plus fortes que le métal de base et la zone de fusion de la charge de référence en utilisant les nouvelles charges à forte teneur en Mg, indiquant ainsi leur potentiel significatif pour le soudage de structures en aluminium à haute résistance.

Dans la deuxième partie, deux charges nouvelles ont été conçues et préparées en augmentant la teneur en Mg dans les métaux de charge 4xxx, et les effets du Mg sur les propriétés mécaniques et de fatigue ont été étudiés dans des conditions soudées et PWHT. Les feuilles AA6061-T6 ont été utilisées comme BM et soudées par GMAW. Les défauts de soudage ont été analysés à l'aide de la radiographie et de la microscopie optique, et les précipités dans les ZPs ont été étudiés à l'aide de la microscopie électronique à transmission (MET). Les propriétés mécaniques ont été évaluées à l'aide des essais de microdureté, de traction et de fatigue. Par rapport à la charge de référence ER4043, les charges avec une teneur accrue en Mg ont produit des joints de soudure avec une microdureté et une résistance à la traction plus élevées. Les joints fabriqués avec des charges ayant une teneur élevée en mg (0,6 à 1,4 % en poids) présentaient des résistances à la fatigue plus élevées et une durée

de vie plus longue que les joints fabriqués avec la charge de référence dans les états tels que soudés et PWHT. Parmi les joints étudiés, les joints avec la charge de 1,4 % Mg en poids présentaient la résistance à la fatigue la plus élevée et la meilleure durée de vie à la fatigue. L'amélioration de la résistance mécanique et des propriétés de fatigue des joints en aluminium a été attribuée au renforcement amélioré de la solution solide par Mg soluté dans l'état tel que soudé et au renforcement accru des précipitations par des précipités  $\beta''$  dans l'état PWHT.

Dans la troisième partie, l'étude a examiné les effets des métaux d'apport Al-Si-Mg nouvellement développés avec des teneurs variables en Mg (0,6 à 1,4 % en poids) et en Mn (0,25 à 0,5 % en poids) sur l'évolution de la microstructure et les performances mécaniques des plaques AA6011-T6 à haute résistance utilisant le soudage à l'arc au gaz. Deux remplisseurs commerciaux, ER4043 et ER4943, ont été utilisés comme références pour la comparaison. Les résultats ont révélé que l'augmentation des teneurs en Mg et en Mn dans les charges nouvelles entraînait des éléments d'alliage suffisamment élevés dans la FZ, entraînant une microdureté plus élevée. Dans des conditions de soudage comme soudé, la région la plus faible du joint était la HAZ. La résistance du joint était presque indépendante du type de charge et était contrôlée par la résistance HAZ. Les teneurs plus élevées en Mg dans les charges nouvelles ont favorisé la précipitation d'une grande fraction volumique de  $\beta''$ -MgSi fin dans la FZ pendant le PWHT, ce qui a entraîné une résistance supérieure et une efficacité de soudage plus élevée par rapport aux charges de référence. La teneur optimale en Mg des charges nouvelles était de 0,6 % en poids. L'augmentation de la teneur en Mn du métal d'apport a eu un effet négligeable. La charge FMg0.6 avec 0,6% Mg a obtenu la meilleure combinaison de résistance et d'allongement, ainsi que l'efficacité de soudage la plus élevée après PWHT, parmi toutes les charges étudiées. Cependant, les charges nouvellement développées ont nui à la résistance aux chocs des joints.

Dans la quatrième partie, les performances de soudage des fils de remplissage ER4043, ER5356 et FMg0.6 nouvellement développés sur le GMAW des plaques AA6011-T6 ont été systématiquement étudiées. Les propriétés de microstructure, mécaniques, de fatigue et de corrosion des soudures AA6011 utilisant trois fils de remplissage ont été analysées et comparées. Les résultats ont révélé que les joints ER4043 et FMg0.6 présentaient des granulométries plus petites dans la FZ par rapport au joint ER5356. PWHT a entraîné la formation de  $\beta$ -Al<sub>2</sub>Mg<sub>3</sub> aux joints de grains du joint ER5356, tandis que la sphéroïdisation du Si eutectique et la fragmentation partielle des composés intermétalliques riches en Fe se sont produites dans les joints ER4043 et FMg0.6. Les joints ER5356 et FMg0.6 soudés présentaient une dureté et une résistance à la traction supérieures à celles du joint ER4043, et leurs fractures se sont produites dans la zone la plus molle affectée par la chaleur, tandis que le joint ER4043 a été fracturé dans la FZ. Parmi tous les joints, le joint FMg0.6 a démontré la résistance la plus élevée et la résistance à la fatigue supérieure dans les conditions soudées et PWHT. Le joint ER5356 présentait la perte de poids la plus élevée à l'état tel que soudé et présentait le taux de corrosion le plus élevé dans l'état PWHT en raison de la précipitation de  $\beta$ -Al<sub>2</sub>Mg<sub>3</sub>. En raison de la fraction volumique élevée de Mg<sub>2</sub>Si primaire dans le joint FMg0.6 soudé, il avait un taux de corrosion plus élevé par rapport au joint

ER4043. Le PWHT a amélioré la résistance à la corrosion du joint FMg0.6. Avec son efficacité de soudage élevée, ses propriétés de fatigue supérieures et sa résistance à la corrosion acceptable, la charge FMg0.6 nouvellement développée est un métal d'apport prometteur pour le soudage d'alliages 6xxx à haute résistance.

## Abstract

Aluminum alloys find widespread application and serve as substitutes for steel components due to their high strength-to-weight ratio and corrosion resistance. With the increasing use of aluminum alloys across various industries, the joining of different parts to create high-strength assemblies and structures emerges as a critical concern in industrial applications such as automotive, aircraft, and shipbuilding. Aluminum components, often necessitating joining, are typically fused together using various techniques such as gas metal arc welding (GMAW) and tungsten inert gas (TIG). Fusion welding of heat-treatable aluminum-based alloys, particularly those in the 6xxx series, presents several challenges, including compromised strength in the fusion zone (FZ), susceptibility to welding-induced cracking, reduced mechanical strength in the heat-affected zone (HAZ), and increased porosity in the weld metal. These challenges are intertwined with factors such as the chemistry of the filler metal, susceptibility to cracking, and the parameters of the welding process.

In the first part, an investigation was conducted into the performance and mechanical strength of joints achieved through the utilization of recently developed Al-Si-Mg filler metals. These fillers were characterized by varying Mg contents ranging from 0.6 to 1.4 wt.%, and the welding process involved a 2 mm thick AA6061 base metal (BM). The results revealed that the newly developed filler metals have excellent weldability similar to that of the ER4043. The Mg content in the FZs of the new fillers was found to be higher than that of the reference filler. The as welded joints were fractured in the softest zone of the HAZ showing the same strength but lower than that of the BM. The post-weld heat treatment (PWHT) removed the HAZ and recovered its strength. Furthermore, the PWHT leads to the formation of coherent  $\beta''$ -MgSi precipitates which brought the strength of the heat-treated joints to the level of the BM with 100% welding efficiency. Furthermore, the FZs of the newly developed fillers were stronger than the BM and the FZ of the reference filler, ER4043, thus indicating their significant potential for welding high strength aluminum structures.

In the second part, two novel fillers were designed and prepared by increasing the Mg content in 4xxx filler metals, and the effects of Mg on the mechanical and fatigue properties were studied under as welded and PWHT conditions. AA6061-T6 sheets were used as the BM and welded by GMAW. The welding defects were analyzed using X-ray radiography and optical microscopy, and the precipitates in the FZs were studied using transmission electron microscopy (TEM). The mechanical properties were evaluated using the microhardness, tensile, and fatigue tests. Compared to the reference ER4043 filler, the fillers with increased Mg content produced weld joints with higher microhardness and tensile strength. Joints made with fillers with high Mg contents (0.6–1.4 wt.%) displayed higher fatigue strengths and longer fatigue lives than joints made with the reference filler in both the as-welded and PWHT states. Of the joints studied, joints with the 1.4 wt.% Mg filler exhibited the highest fatigue strength and best fatigue life. The improved mechanical strength and fatigue properties of the aluminum joints were attributed to the enhanced solid-solution strengthening by solute Mg in the as-welded condition and the increased precipitation strengthening by  $\beta''$  precipitates in the PWHT condition.

In the third part, the study investigated the effects of newly developed Al-Si-Mg filler metals with varying Mg (0.6–1.4 wt.%) and Mn (0.25–0.5 wt.%) contents on microstructure evolution and mechanical performance of high-strength AA6011-T6 plates using gas metal arc welding. Two commercial fillers, ER4043 and ER4943, were used as references for comparison. The results revealed that increasing the Mg and Mn contents in the novel fillers resulted in sufficiently high alloying elements in the FZ, leading to higher microhardness. Under as-welded conditions, the weakest region of the joint was the HAZ. The joint strength was almost independent of the filler type and was controlled by the HAZ strength. The higher Mg contents in the novel fillers promoted the precipitation of a large volume fraction of fine  $\beta''$ -MgSi in the FZ during PWHT, resulting in superior strength and higher welding efficiency relative to the reference fillers. The optimal Mg content of the novel fillers was 0.6 wt.%. Increasing the Mn content of the filler metal had an insignificant effect. The FMg0.6 filler with 0.6% Mg achieved the best combination of strength and elongation, as well as the highest welding efficiency after PWHT, among all fillers studied. However, the newly developed fillers adversely affected the impact toughness of the joints.

In the fourth part, the welding performance of ER4043, ER5356 and newly developed FMg0.6 filler wires on the GMAW of AA6011-T6 plates was systematically investigated. The microstructure, mechanical, fatigue and corrosion properties of AA6011 weldments using three filler wires were analyzed and compared. The results revealed that the ER4043 and FMg0.6 joints exhibited smaller grain sizes in the FZ compared to ER5356 joint. PWHT resulted in the formation of  $\beta$ -Al<sub>2</sub>Mg<sub>3</sub> at the grain boundaries of ER5356 joint, while spheroidization of eutectic Si and partial fragmentation of Fe-rich intermetallics occurred in ER4043 and FMg0.6 joints. The as-welded ER5356 and FMg0.6 joints displayed higher hardness and tensile strength compared to ER4043 joint, and their fractures occurred in the softest heat affected zone, while the ER4043 joint was fractured in the FZ. Among all the joints, the FMg0.6 joint demonstrated the highest strength and superior fatigue strength in both as welded and PWHT conditions. The ER5356 joint exhibited the highest weight loss in the as-welded state and suffered the highest corrosion rate in the PWHT condition due to the precipitation of  $\beta$ -Al<sub>2</sub>Mg<sub>3</sub>. Due to high volume fraction of primary Mg<sub>2</sub>Si in the as-welded FMg0.6 joint, it had a higher the corrosion rate compared to ER4043 joint. The PWHT improved corrosion resistance of FMg0.6 joint. The FMg0.6 filler shows promise for welding high-strength aluminum alloys, attributed to its high welding efficiency and superior fatigue properties, alongside acceptable corrosion resistance.

# Table of contents

Résumé.....	iii
Abstract.....	vi
Table of contents.....	viii
List of Figures.....	x
List of Tables.....	xiii
DEDICATION.....	xiv
ACKNOWLEDGEMENT.....	xv
1. CHAPTER 1: INTRODUCTION.....	1
1.1 Background.....	1
1.2 4xxx fillers.....	2
1.3 Development in the 4xxx fillers.....	3
1.4 Welding of aluminum alloys challenges.....	4
1.5 The post weld heat treatments.....	4
1.6 Definition of the problem.....	5
1.7 Objectives.....	6
1.8 Originality Statement.....	8
1.9 Thesis outlines.....	10
1.10 References.....	12
2. CHAPTER 2: Developing High-Strength Al-Si-Mg Filler Metals for Aluminum Fusion Welding.....	14
2.1 Introduction.....	15
2.2 Experimental procedure.....	17
2.3 Results and discussion.....	20
2.3.1 Weld geometry and imperfection.....	20
2.3.2 Microstructures.....	22
2.3.3 Mechanical properties.....	27
2.3.4 Tensile properties.....	29
2.3.5 TEM analysis.....	32
2.4 Conclusion.....	35
2.5 References.....	37
3. Chapter 3: Welding of AA6061-T6 Sheets Using High-Strength 4xxx Fillers: Effect of Mg on Mechanical and Fatigue Properties.....	40

3.1	Introduction.....	41
3.2	Experimental procedure.....	44
3.3	Results and discussion .....	46
3.3.1	Welding defect analysis.....	46
3.3.2	Mechanical properties.....	48
3.3.3	Fatigue properties .....	53
3.4	Conclusions.....	64
3.5	References.....	66
4.	Chapter 4: Microstructure and mechanical properties of high-strength AA6011 aluminum alloy welding with novel 4xxx filler metals .....	70
4.1	Introduction.....	71
4.2	Experimental Procedure.....	73
4.3	Results and Discussion .....	77
4.3.1	Microstructure.....	77
4.3.2	Mechanical properties.....	82
4.3.3	Comparison of the welding efficiency of various Al-Mg-Si alloys.....	93
4.3.4	Discussion.....	95
4.3.5	Conclusions.....	96
4.4	References.....	98
5.	Chapter 5: Comparison of Mechanical, Fatigue and Corrosion Properties of Fusion-Welded AA6011-T6 Plates Using Three Different Filler Wires .....	103
5.1	Introduction.....	104
5.2	Experimental Procedure.....	107
5.3	Results and discussion .....	111
5.3.1	Microstructure of the Joint.....	111
5.3.2	Microhardness.....	115
5.3.3	The tensile Properties.....	118
5.3.4	Fatigue Properties of the Joint .....	120
5.3.5	Corrosion Resistance of the Joint .....	124
5.3.6	Discussion.....	132
5.4	Conclusions.....	134
5.5	References.....	136
6.	Chapter 6: General conclusions and recommendations .....	142
6.1	General Conclusions .....	142
6.2	Recommendations.....	145

## List of Figures

Figure 2.1. Flowchart of the experimental process.....	19
Figure 2.2. Dimension of the tensile samples for (a) standard and (b) double-edge notched samples (mm).....	19
Figure 2.3. Macro view of a typical joint cross section for the dilution calculation. ....	20
Figure 2.4. (a) XRT image of the weld and (b) macroscopic views of the low and high porosity zones (pores are indicated with red arrows). ....	21
Figure 2.5. Grain morphology of the (a) BM, (b) HAZ, and (c) FZ in the joints welded with Mg1.4 filler. ....	22
Figure 2.6. Predicted phase amounts of (a) ER4043 and (b) Mg1.4 joints under non-equilibrium Scheil condition.....	24
Figure 2.7. SEM images of the FZ of the (a) ER4043 and (b) Mg1.4 joints in the as-welded condition. All phases were identified by SEM-EDX.....	24
Figure 2.8. (a) Mg concentration at the weld surface and weld toe, (b) Mg distribution along the weld centerline and macro images of the black smut (Mg and Al oxides) around the weld bead in (c) ER4043, (d) Mg0.6, and (e) Mg1.4 joints. ....	26
Figure 2.9. SEM images of the FZ in (a) ER4043 and (b) Mg1.4 joints after PWHT. ....	27
Figure 2.10. Microhardness profiles of the welded joints in (a) as-welded condition and (b) after PWHT.....	29
Figure 2.11. (a) Tensile strengths of the standard samples and (b) macro-images of fractured tensile samples under different conditions. The white and red arrows indicate the FZs and the fractures, respectively. ....	30
Figure 2.12. Tensile strengths of the notched samples in (a) as-welded and (b) PWHT conditions. The black and red dash lines in (a) represent the YS and UTS of the standard samples in the as-welded condition, while the blue and green dash lines in (b) show the YS and UTS of the standard samples in the PWHT condition. ....	32
Figure 2.13. Bright-field TEM images of (a) $\beta''$ precipitates in BM, (b) $\beta$ precipitates at 2 mm from the fusion line, and (c) $\beta'$ precipitates at 7 mm from the fusion line in the Mg1.4 joint. ....	34
Figure 2.14. Bright-field TEM images of $\beta''$ precipitates in the FZs of (a) ER4043, (b) Mg0.6, (c) Mg1.4 joints. (d) Quantitative results of the $\beta''$ precipitates.....	35
Figure 3.1. Schematic of the filler wire manufacture and welding process.....	45
Figure 3.2. Dimension of the samples (a) standard samples for tensile and fatigue tests and (b) double-edge notched samples for tensile test [11, 23, 24]. ....	46
Figure 3.3. a) X-ray radiography results, b) macroimage of the cross-section of FMg1.4 joints, c) the optical microimage of porosity in the low porosity zone (The red arrows for gas pores and yellow arrows for shrinkage porosity), and d) the overall area fraction of the pores with XRT and the area fraction of the pores in the low porosity zone with metallographic analysis.....	48
Figure 3.4. (a) Schematic of microhardness profiles and location in as welded and PWHT condition, (b) The average of the microhardness in the FZs and HAZs of three filler joints in as welded and PWHT conditions.....	49
Figure 3.5. (a) tensile strengths of the standard samples and (b) tensile strengths of the notched samples in as welded (AW) and PWHT conditions. The blue and black dotted lines in (b) representing the YS and UTS of BM, respectively.....	52

Figure 3.6. Bright-field TEM images of $\beta''$ precipitates in the FZs of (a) BM, (b) ER4043, (c) FMg0.6 and (d) FMg1.4 joints, (e) Quantitative results of $\beta''$ precipitates. ....	53
Figure 3.7. (a) S-N curves in as welded and (b) in PWHT conditions, (c) the fatigue strength as a function of the UTS in both as welded and PWHT conditions. ....	56
Figure 3.8. (a) SEM image of the fatigue fracture surface showing an example of pores and (b) the projection area of the pores. ....	57
Figure 3.9. Fatigue life as a function of pores size at maximum applied stress of 170 MPa in the as welded condition.....	58
Figure 3.10. SEM images of the fatigue fracture surface in as welded condition at $\sigma_{max}$ of 200 MPa, (a) macroscopic view, (b) the initiation and propagation zones and (c) the final zone for ER4043 joint; (d) macroscopic view, (e) the initiation and propagation zones and (f) the final zone for FMg1.4 joint.....	61
Figure 3.11. SEM images of the fatigue fracture surface in PWHT condition at $\sigma_{max}$ of 200 MPa, (a) macroscopic view, (b) the initiation and slip bands and (c) the final zone for ER4043 joint; (d) macroscopic view, (e) the initiation and slip bands and (f) the final zone for FMg1.4 joint.....	62
Figure 3.12. Fatigue striations during crack propagation in PWHT condition at $\sigma_{max}$ of 200 MPa, (a) evaluation of fatigue striation, and (b) and (c) SEM images showing the striations at 0.5 mm and 1.5 mm from the crack initiation zone for ER4043 joint; (d) and (e) SEM images showing the striations at 0.5 mm and 1.5 mm from the crack initiation zone for FMg1.4 joint; (f) striation width at different distances from the initiation zone. ....	63
Figure 4.1. (a) Dimensions of the extruded BM and (b) Single V-groove joint (mm). ....	75
Figure 4.2. Macroview of a typical cross section joint for the dilution calculation. The areas for the (a) first pass and (b) second pass.....	76
Figure 4.3. (a) Dimensions of the impact samples and their notches. (b) The notch position in the weld zone [17]. ....	76
Figure 4.4. Optical microscopy of the different zones of the as-welded FMg1.4 joint. (a) and (b) show the microstructure in the first and second passes, respectively. (c) The heat affected zone in the first pass by the heat input of the second pass.....	79
Figure 4.5. SEM images showing the microstructures of the second pass: (a) ER4043, (b) FMg0.6, and (C) Mg1.4Mn joints under the as-welded condition; and (d) ER4043, (e) FMg0.6, and (f) Mg1.4Mn joints under the PWHT condition, respectively. ....	79
Figure 4.6. SEM-EDs analysis of the different phases identified in Figure 4.5. ....	80
Figure 4.7. Bright-field TEM images of (a) $\beta''$ precipitates in the BM; (b) $\beta'$ precipitates in ER4043; $\beta''$ precipitates in (c) FMg0.6 and (d) FMg1.4 joints. (e) Quantitative analysis of the precipitates. ....	81
Figure 4.8. Hardness measurements in the joints for (a) first and (b) second passes in the as-welded condition and (c) first and (d) second passes in the PWHT condition. ....	84
Figure 4.9. The tensile properties in the (a) as-welded and (b) PWHT conditions; (c) the welding efficiency in the as-welded and PWHT conditions.....	87
Figure 4.10. Fracture surfaces of the PWHT tensile samples. Porosity in the (a) ER4043 and (b) Mg1.4Mn joints. (c–e) First pass of ER4043, FMg0.6, and Mg1.4Mn joints. (f–h) Second pass of ER4043, FMg0.6, and Mg1.4Mn joints.....	89
Figure 4.11. Impact toughness of the BM, HAV, and FZ of all joints under as welded and PWHT conditions. ....	91
Figure 4.12. Fracture surfaces of the impact samples under as-welded condition: Macroviews of the (a) HAZ and (b) ER4043 joint in the first pass. Macroviews of the (c) HAZ, (d) and	

(e) ER4043 joint in the second pass. Macroviews of the FMg1.4 joint in the (f) first and (g) second passes. ....	92
Figure 5.1. Dimensions of the tensile and fatigue samples in mm. ....	110
Figure 5.2. Schematic drawing of the immersion test, (a) sample dimensions, and (b) the test set up. All dimensions are in mm. ....	111
Figure 5.3. Grain morphologies of the different zones under as welded condition. FMg0.6: (a) BM, (b) and (c) recrystallized zones (RZ) in ER5356 and ER4043 joints, respectively; (d) and (e) the FZs in the 1 <sup>st</sup> and 2 <sup>nd</sup> passes in ER5356 joint, respectively; (f) and (g) the FZs in the 1 <sup>st</sup> and 2 <sup>nd</sup> passes in FMg0.6 joints, respectively; (h) the boundary between the 1 <sup>st</sup> and the 2 <sup>nd</sup> passes in ER4043 joints. The green arrows point to the porosity. ....	114
Figure 5.4. (a) and (b) microstructure of the BM. (c), (d), and (e) microstructures of the 2 <sup>nd</sup> pass of ER5356, ER4043, and FMg0.6 joints under the as welded condition, respectively. (f), (g) and (h) microstructures of the 2 <sup>nd</sup> pass of the ER5356, ER4043, and FMg0.6 joints after PWHT, respectively. All phases were identified with the SEM-EDX. ....	115
Figure 5.5. Microhardness profiles, (a) and (b) for as welded condition in the first and second passes. (c) and (d) after PWHT in the first and second passes. ....	117
Figure 5.6. The tensile properties of the joints: (a) in the as welded condition, and the insets showing the typical fractures occurred in the tensile sample; (b) in the PWHT condition. ....	120
Figure 5.7. The S-N curves of the welded joints, (a) in as welded condition, and (b) in the PWHT conditions. ....	123
Figure 5.8. Fatigue fractures in the PWHT condition: (a), (b) and (c) the initiation, propagation, and final zones of ER5356 joint. (d), (e) and (f) the initiation, propagation, and final zones of ER4043 joint; (g), (h) and (i) the initiation, propagation, and final zones of FMg0.6 joint. ....	123
Figure 5.9. Potentiodynamic polarization curves (a) in as welded, (b) in PWHT conditions, and (c) an example shown The Tafel extrapolation for $I_{corr}$ and $E_{corr}$ estimation. ....	128
Figure 5.10. Macroscopic images of the pitting corrosion in the corroded surfaces of (a) the BM, (e) the HAZ, (b), (c) and (d) the welded joints in the as welded condition; (f), (g) and (h) the welded joints in in the PWHT condition. ....	129
Figure 5.11. Surface morphology of pits after polarization in 3.5 wt.% NaCl solution, (a) BM, (b) HAZ, (c) and (d) 1st pass of ER4043 in as welded and PWHTed cases, respectively, (e) and (f) 2nd pass of FMg0.6 in as welded and PWHTed cases, respectively, and (g) 1st pass of ER5356 in PWHTed case. ....	130
Figure 5.12. Results of the immersion corrosion tests (a) in as welded and (b) in PWHT conditions. ....	132

## List of Tables

Table 2.1. Chemical compositions of the base metal and filler metals. ....	20
Table 2.2. The chemical compositions of the FZs calculated after dilution. ....	20
Table 3.1. Chemical compositions of the base metal and filler wires. ....	46
Table 4.1. Chemical compositions of the base metal and filler metals (wt.%) .....	75
Table 4.2. The welding parameters used. ....	76
Table 4.3. The calculated chemical compositions in the first and second passes (wt.%)....	76
Table 4.4. Comparison of the welding efficiency for various Al-Mg-Si alloy fusion welding in both AW and PWHT conditions. ....	94
Table 5.1: Chemical compositions of BM and three filler wires (wt.%).....	110
Table 5.2: The welding parameters used. ....	110
Table 5.3. The corrosion parameters from the potentiodynamic polarization test. ....	129
Table 5.4. EDs analysis of the corroded BM, HAZ and welded joints .....	130

## DEDICATION

In dedicating this thesis, I pay tribute to the cherished individuals who have been the pillars of strength throughout my academic journey.

My late father, Ramadan Ahmed, whose unwavering support served as a guiding light, remains a source of inspiration even in his absence.

To my mother, Sayda Abdurahman, the cornerstone of my life, your boundless love and encouragement have been my driving force.

My brother, Shaban Ahmed, a constant source of motivation, has played a significant role in my pursuit of success.

To my beloved wife, your steadfast support has been the bedrock of my achievements, and I am profoundly grateful for your unwavering belief in me.

Lastly, to my son, Eyad Ahmed, the beacon of light and joy in my life, your presence has added immeasurable meaning to this academic endeavor.

This thesis is dedicated to the memory of my father and the love and strength of my family, without whom this journey would not have been possible.

## ACKNOWLEDGEMENT

*First and foremost, I would like to thank the Almighty God, by whose mercy I live, have my sustenance, inspiration, and direction for life.*

*I would like to express my sincere gratitude to everyone who helped, encouraged, and supported me during my Ph.D. study at the University of Quebec at Chicoutimi (UQAC).*

*I would like to express my sincere gratitude to Prof. X.-Grant Chen, my supervisor, for providing me with the invaluable opportunity to pursue my Ph.D. studies under his guidance. His mentorship, support, and encouragement have been instrumental in shaping my academic journey.*

*I am also deeply thankful to Prof. Mousa Javidani, my co-supervisor, for his guidance and assistance throughout the planning, development, and writing phases of the research. His expertise and insights have significantly contributed to the quality and depth of this work.*

*A special thanks to Prof. Zhan Zhang and Mr. Zhixing Chen for helping me to conduct SEM and TEM observations. I would like to convey my sincere gratitude to Prof. Khaled Ragab for giving me a chance to make my dream come true. He greatly supported me in settling down in Chicoutimi and adapting to the new environment and culture. He has always been supportive during my study and treated me as his brother.*

*I would also like to thank all the staff in CURAL for their help and support. Special thanks go to our technicians, Mr. Dany Racine, Mr. Samuel Dessureault, Mr. Felix Tremblay for supporting our experiments in CURAL. I am also deeply indebted to all my colleagues and friends in the department for their kind support, scientific discussions, suggestions, and for making my life much more delightful in Chicoutimi: Siamak Nikzad, M. Attia, Jovid Rakhmonov, Quan Shao, Ahmed Algendy, Ali Elashry, Mohamed Hafez, Chaima Hajji, Mohammadreza Mofarrehi, Peng Hu, Liying Cui, Redouane Farid, Henry Agbe, Karthikeyan Rajan, Alyaa Bakr, Abhishek.*

*Finally, but no means least, I would like to thank my beloved wife for her unconditional love and infinite encouragement throughout my PhD research. Most importantly, I could not possibly finish this work without the encouragement and support of my mother and my brother. Warm wishes to my whole family for their unending love and trust throughout my education.*

*This project was financially supported by the Natural Science and Engineering Research Council of Canada (NSERC), Rio Tinto Aluminum through the NSERC Industry Research Chair in the Metallurgy of Aluminum Transformation, and Mathematics of Information Technology and Complex Systems (Mitacs) at Université du Québec à Chicoutimi (UQAC). I would like to thank both organizations for their support during my study.*

# 1. CHAPTER 1: INTRODUCTION

## 1.1 Background

Welding is a fabrication process that joins metals, by causing fusion, melting, or coalescence. This is often achieved by heating the metals to their melting point or using pressure, with or without the addition of filler material, to create a permanent bond between the joined parts. Brazing, an ancient technique, involves using a braze metal that melts at a temperature above 450°C but below the melting point of the components to be joined. This prevents the parent metals from melting. Soldering is a nearly identical process, with the key distinction being that the solder's melting point is below 450°C. When welding involves solely melting and fusing the parent metals, it is termed autogenous welding. However, numerous processes incorporate the addition of a filler metal, introduced in the form of a wire or rod, which melts into the joint. This filler metal combines with the melted base metal to form the fusion zone (FZ) [1].

The fusion welding joint comprises of the FZ, heat affected zones (HAZ) and the adjacent base metal (BM). The mechanical properties of the welded joint depend mainly on two zones, the HAZ and the FZ. The HAZ is formed because the heat input from the welding process leads to decline the strengthening mechanism such as the strain hardening and the precipitation hardening. The reduction in the mechanical properties in HAZ depends mainly on the type of the BM alloy. The strain hardened alloys such as 3xxx and 5xxx can lose the strength via recovery and recrystallization in HAZ. While the heat treatable alloys such as 2xxx and the 6xxx loses their strength by dissociation and coarsening of the precipitation hardening particles such as  $\beta''$  and as  $\beta'$  as well as the recovery and the recrystallization [2].

The FZ strength relies on the level of the welding defects which can be controlled by optimizing the welding parameters. Moreover, the chemical composition of the formed FZ plays the most important role in determining the final strength of the joint. The chemical composition mainly depends on the BM dilution and the type of the used filler alloy.

The demand for high strength weldable 6xxx Al products is continuously increasing in many application such as marine, electric, and transportation industries [3]. The mechanical properties of the 6xxx Al alloys are mainly driven by number density and volume fraction of the nano sized metastable  $Mg_2Si$  precipitates. Therefore, the chemical composition (most specifically Mg and Si content), and the applied heat treatment process are the critical parameters to achieve the desired mechanical properties [4, 5]. Furthermore, as the 6xxx Al products are widely used in car bodies, they are mostly required to be joined by fusion welding process. Various welding techniques have been developed to join the aluminum components, such as gas metal arc welding (GMAW), laser beam welding (LBW) and tungsten inert gas (TIG) [6, 7]. The heat treatable Al-based alloys (i.e., 6xxx) during fusion welding encounter, however, several weldability problems, namely lower strength of fusion zone, cracking during welding, as well as high porosity content in the weld metal [8, 9].

## **1.2 4xxx fillers**

Commercial Al-Si based AA4043 weld wires have been widely used in general-purpose welding of 6xxx Al products. This filler metal is characterized by high fluidity and very good resistance to weld/solidification cracking. However, due to the composition of AA4043 filler metal (Al - 5Si), the mechanical properties of the joints is strongly dependent on dilution with the base metal [10-12]. In a fusion welding process, the Mg of the 6xxx base metal is added to the weld bead, which contribute to strengthening via solution strengthening in the

as welded condition or  $Mg_2Si$  precipitation hardening in the post weld heat treatment (PWHT) condition. However, there are many situations in which the dilution ratio between the base metal and filler wire can fluctuate, and hence influence the strength of the joints [11].

### **1.3 Development in the 4xxx fillers**

The choice of the filler type for aluminum welding relies on their alloying element compatibility with the BM, and the liquid-state properties play a vital role in preventing the hot cracking and ensuring effective dispersion and fusion with the BM. Specifically, for Al-Mg-Si alloys, selecting a suitable filler metal has the potential to improve the strength of the FZ [13].

Among the widely used general-purpose welding filler wires, AA 4043 and AA 5356 stand out. These filler materials were specifically formulated for welding purposes. AA 4043 contains 5% Si, while AA 5356 contains 5% Mg. When welding AA 6061 BM, AA 5356 is the preferred choice due to its generally greater strength and ductility. On the other hand, AA 4043's silicon content enables better flow, increased crack resistance, and improved weldability. AA 4943 (5% Si – 0.4% Mg) combines features from both AA 4043 and AA 5356, offering the advantages of AA 4043 along with increased strength and ductility. AA 4943 is suitable for all applications that utilize 4043, including base alloys 1xxx, 3xxx, 4xxx, and 6xxx. However, it's not recommended for 5xxx series alloys containing more than 2.5% magnesium, as this could lead to the formation of coarse  $Mg_2Si$ , negatively impacting joint strength and ductility [14].

AA 4943 was formulated with magnesium as a strengthening element, providing strength independently of base metal dilution diffusion. The magnesium addition, ranging from 0.1%

to 0.5%, is targeted at achieving a desired  $Mg_2Si$  precipitation level while avoiding the sensitivity peak at 1%  $Mg_2Si$ . The silicon content is held within the range of 5.0-6.0% to retain the free silicon characteristic of AA 4043, crucial for fluidity properties and resistance to hot cracking during solidification. Silicon also contributes to enhanced fracture toughness and fatigue performance [13].

#### **1.4 Welding of aluminum alloys challenges**

Aluminum welding faces challenges primarily due to its high thermal conductivity, electrical conductivity, significant thermal expansion coefficient, tendency to form refractory aluminum oxide, and relatively modest stiffness, as reported by Rajan et al. [15]. Consequently, these factors impose limitations on the welding process, resulting in challenges such as oxide elimination and reduced strength in both the weld and the Heat-Affected Zone (HAZ). These combined factors collectively influence the effectiveness and overall quality of the welds, as outlined in reference [13]. Furthermore, in its molten state, aluminum demonstrates notable solubility towards hydrogen and other gases [3], contributing to the formation of porosity within the weld bead.

#### **1.5 The post weld heat treatments**

The mechanical properties of weld joints are influenced by welding defects, composition, microstructure, and metallurgical states of the weld metal and adjacent base metal. In heat-treatable alloys, the primary contributors to hardness reduction are the loss of precipitates in the weld and overaging in the HAZ. Solution and aging heat treatments can be employed to restore hardness in these regions. For AA 6061, the key welding challenge is the decline in mechanical properties in the FZ and the losing the strength in the HAZ [16]. Post-weld heat treatment (PWHT) is applied to alleviate residual stresses and modify the microstructure,

thereby enhancing the mechanical and chemical properties of the fusion-welded joint. When utilizing a 4xxx fillers with 6061 BM, the weld zone does not respond significantly to the PWHT since there is insufficient Mg content for the precipitation of nano-sized  $\beta''$ -MgSi, the main strengthening phase. Performing post weld age hardening alone does not yield a beneficial effect on tensile properties. While applying the Solutionizing followed by quenching enables the uniform distribution of solute atoms into the solution, forming homogenous distribution of Guinier-Preston (GP) zones upon performing the aging step [17].

### **1.6 Definition of the problem**

Nowadays, using of aluminum alloys in many applications as a replacement to the steel parts and structures makes the welding of these alloys very crucial to the industry. Welding of the heat treatable alloys such as the 6xxx alloys is usually attributed to the loss of the HAZ strength due to dissolving or coarsening the strengthening precipitates. Furthermore, the FZ is usually weak zone in the joint due to the welding defects such as pores and using the commercial fillers metals, ER4043 and ER5356. This kind of fillers has less or no strengthening elements and hence produce FZs of low strength and low efficiency compared to the BM. Furthermore, in many applications such as the automotives, the aluminum welded parts are exposed to the cyclic loading or fatigue loading. The structures welded with the commercial fillers lead to lower fatigue strength and life due to lower obstacles in front of the dislocations and hence fast fatigue crack growth happens.

There are many attempts have been done to overcome this reduction in the strength and the fatigue properties via addition of ceramic nanoparticles such as the TiC and Al<sub>2</sub>O<sub>3</sub> to the fillers [18-20]. Additionally, other researchers tried to modify the chemical composition of

the used 4xxx fillers such as addition of Sr to modify the microstructure and the Mg (up to 0.4%) to produce a heat treatable FZs. However, the joint strength still low relative to the BM. In this case other issues such as using thick BMs and high cost should be added to achieve the required load bearing capacity of the welded structure.

Finally, the utilization of the aluminum alloys exceeds in marines' industry. The welding of the aluminum alloys affects on the corrosion resistance of the whole joint especially in the corrosive media such as the sea water and the industrial corrosive substances. This effect came from the non-homogeneous microstructure and chemical compositions of the different zones in the welded joints. Changes in the filler's composition can influence the corrosion resistance of the fusion zone (FZ). Therefore, any adjustment to the filler's chemical composition should be coupled with a comprehensive examination of the chemical properties of both the FZs and the entire welded joints.

## **1.7 Objectives**

The general objective of this work is to understand the effect of the addition of Mg and Mn on the microstructure of the welded joints in the as welded and PWHT. Moreover, the effect of the added alloying elements on the mechanical properties, including tensile, fatigue strengths, and impact toughness will be studied in the as welded and PWHTed samples using two BMs, AA6061 and AA6011. The specific objectives of three subprojects are listed below:

**1. Part 1: Developing High-Strength Al-Si-Mg Filler Alloys for Aluminum Fusion**

**Welding of AA6061-T6 Base Metals**

- a. Study the weld geometry and imperfection of the joints welded with the new fillers.
- b. Study the effect of the Mg on the microstructure in the as welded and PWHT conditions.
- c. Investigate the Mg distribution and the welded soundness in the welded joints.
- d. Investigate the impact of the added Mg on the tensile strength using the smooth and notched sampled in the as welded and PWHT conditions.

**2. Part 2: Welding AA6061 sheets by novel high strength 4xxx filler wires: effect of Mg content on mechanical and fatigue properties.**

- a. Study the microstructure and the mechanical properties of the welded samples in as welded and PWHT conditions.
- b. Study the effect of the added Mg on the fatigue strength in as welded condition.
- c. Study the effect of the heat treatment on the fatigue strength of the welded joints.
- d. Study the effect of the porosity on the fatigue properties of the welded samples.

**3. Part 3: Welding AA6011-T6 thick plates by novel high strength 4xxx filler alloys: influence of Mg and Mn on the mechanical and impact toughness properties.**

- a. Study the effect of the added Mg and Mn on the microstructure using thick plates of AA6011-T6 base metal.
- b. Evaluating the influence of Mg and Mn contents on tensile properties of thick and high strength AA6011-T6 base metal with low dilution joint geometry in as-welded and PWHT conditions

- c. Study the effect of using the newly developed fillers on the impact toughness in the as welded and PWHTed samples.

#### **4. Part 4: Comparison of Mechanical, Fatigue and Corrosion Properties of Fusion-Welded AA6011-T6 Plates Using Three Different Filler Wires**

- a. Comprehensive investigation of the tensile strength of the welded AA60611-T6 aluminum alloy with ER4043, ER5356, and FMg0.6 fillers.
- b. Studying the effect of using different fillers metals on the fatigue strength and life of the welded joints.
- c. Studying the corrosion resistance of the welded AA60611-T6 with the newly developed filler of FMg0.6 in comparison with using the commercial fillers of ER4043 and ER53256.

### **1.8 Originality Statement**

The current research work focuses on the mechanical properties of the welded AA6061 and AA60611 BMs with the newly modified ER4043 with addition of Mg and Mn to its composition. The following points address the subjects in this thesis that have lack of knowledge in the literature.

In the first part, different fillers with different Mg content were used to weld AA6061-T6 sheet with 2 mm in thickness. This is to understand the effect of the added Mg on the mechanical properties and the welded performance in comparison to the commercial filler metal, ER4043. This study also involves the microstructure investigation of the phases and

the nanoscale precipitates to explain the development occurred in the tensile strength of the welded joints in the as welded and PWHT conditions.

In the second part, the tensile and fatigue strengths of the welded AA6061-T6 BM with 2 mm thickness were studied. In this study, ER4043, as reference filler, and two newly developed fillers with 0.6 and 1.4% Mg and the same Mn content of 0.25 % were used. This work explains the reasons behind increasing the tensile and the fatigue properties via using the 4xxx fillers containing high Mg content relative to the reference filler. Furthermore, this study reveals the effect of the pores size on the fatigue strength in joints welded with the reference filler and those welded with the newly developed fillers.

In the third part, the advantages of using the high Mg fillers to weld thick BM, AA6011-T6 of 6 mm thickness. This investigation reveals the contribution of the newly developed fillers on the compensation of the Mg loss in the FZs in the second pass if welded with ER4043 reference filler. Moreover, the study shows the impact of the added Mg in the new fillers on the tensile strength of the welded joints in the as welded and PWH conditions. the impact toughness of the welded joints was also revealed in all condition for all the new and the reference fillers.

In the fourth part, the tensile strength of the welded AA60611-T6 welded with ER5356, ER4043, and FMg0.6 was studied to reveal the development in the tensile properties that can be achieved with FMg0.6 in comparison to the commercial fillers. Addition to the tensile strength, the fatigue strength of the welded joints was investigated in the as welded and PWHT conditions. Moreover, the corrosion resistance of the welded joints was conducted to uncover the effect of the added Mg in FMg0.6 on the corrosion rates of

the welded joints in comparison to the commercial reference fillers in the as welded and PWHT conditions.

## **1.9 Thesis outlines**

The thesis consists of six chapters. In Chapter 1, Introduction, a brief background is presented, which starts with the definition of the 4xxx fillers alloys and the relevant use in the welding of the 6xxx aluminum alloys. Then, the developments occurred in the literature regarding to modification of their composition via adding nanoparticles or alloying elements. In addition, the associated problems that were found with using such commercial fillers as reported in the literature. Finally, the corrosion properties of the aluminum alloys were discussed.

In Chapter 2, the published paper “Developing High-Strength Al-Si-Mg Filler Metals for Aluminum Fusion Welding ” in the *Journal of Material Engineering and Performance, 2023* is presented. The paper is drawn from the experimental results, discussing the microstructure and the mechanical properties of the AA6061-T6 BM welded with the modified commercial filler, ER4043, with Mg. The study included testing the microstructure and the mechanical properties in the as welded and PWHT conditions. Furthermore, a comparison was established between the joints welded with the newly developed fillers and the reference filler, ER4043.

In chapter 3, the published paper “ Welding of AA6061-T6 Sheets Using High-Strength 4xxx Fillers: Effect of Mg on Mechanical and Fatigue Properties ” in the *Journal of Material, 2023* is presented. In this paper, the tensile properties and the high cyclic fatigue properties

were systematically investigated. Moreover, the effect of the pores size on the fatigue strength was studied. The investigation was performed in comparison to the reference filler, ER4043.

In Chapter 4, the submitted paper “ Microstructure and mechanical properties of high-strength AA6011 aluminum alloy welding with novel 4xxx filler metals” *to the journal of Materials* is presented. In this paper, the effect of using the newly developed fillers on the mechanical properties of the thick and high strength AA60611 BM. Moreover, the effect of the high Mg fillers on the impact toughness of the welded joints was performed in the as welded and PWHT conditions.

In Chapter 5, the under-review paper “ Comparison of Mechanical, Fatigue and Corrosion Properties of Fusion-Welded AA6011-T6 Plates Using Three Different Filler Wires” is presented. In this article, a comprehensive investigation was performed between the welded AA6011 BM with three different fillers including, ER4043, ER5356, and FMg0.6. the study involved the tensile and the fatigue strengths as well as the corrosion resistances of the welded joints in the as welded and PWHTed samples.

Finally, in Chapter 6, the general conclusions and recommendations for future work are presented. Following this chapter, a list of publications and posters has been presented.

## 1.10 References

1. Weman, K., *Welding processes handbook*. Elsevier: 2011.
2. Lathabai, S., Joining of aluminium and its alloys. In *Fundamentals of Aluminium Metallurgy*, Elsevier: 2011; pp 607-654.
3. Miller, W.; Zhuang, L.; Bottema, J.; Wittebrood, A.; De Smet, P. Recent development in aluminium alloys for the automotive industry. *Mater. Sci. Eng., A*, **2000**, *280*, 37-49.
4. Lakshminarayanan, A.; Balasubramanian, V.; Elangovan, T. I. J. o. A. M. T. Effect of welding processes on tensile properties of AA6061 aluminium alloy joints. **2009**, *40*, 286-296.
5. Pérez, J. S.; Ambriz, R. R.; López, F. F. C. Recovery of mechanical properties of a 6061-T6 aluminum weld by heat treatment after welding. *Metall. Mater. Trans. A*, **2016**, *47*, 3412-3422.
6. Wael, A.; AlShaer; Li, L.; Mistry, A. Effect of filler wire properties on porosity formation in laser welding of AC-170PX aluminium alloy for lightweight automotive component manufacture. *Proceedings of the Institution of Mechanical Engineers, Part B: Journal of Engineering Manufacture*, , **2015**, *231*, 994-1006.
7. Guzmán, I.; Granda, E.; Acevedo, J.; Martínez, A.; Dávila, Y.; Velázquez, R. Comparative in Mechanical Behavior of 6061 Aluminum Alloy Welded by Pulsed GMAW with Different Filler Metals and Heat Treatments. *Materials*, **2019**, *24*, 4157.
8. Anderson, T. A New Development in Aluminum Welding Wire: Alloy 4943. *Weld. J.*, **2013**, *92*, 32-37.
9. Anderson, S. L., Anderson, Bruce E Aluminum welding filler metal, casting and wrought metal alloy (U.S. Patent No. 2015/0132181 A1) , 2015.
10. Anderson, S. L.; Anderson, B. E. Aluminum welding filler metal, casting and wrought metal alloy. 2015.
11. Anderson, T. A New Development in Aluminum Welding Wire: Alloy 4943. *Welding Journal*, **2013**, *33*, 32-36.
12. Anderson, B. E.; Berube, P. Aluminum Alloy Welding Wire. 2015.
13. Bethea, J. F. Gas Tungsten Arc Welding of Aluminum Alloys with Nanocomposite 4943 Filler Material. UCLA, 2019.

14. Aluminum Workshop: The best filler wire for welding 6061-T6 aluminum. Retrieved from <https://www.thefabricator.com/thewelder/article/aluminumwelding/which-filler-wire-is-best-for-welding-6061-t6-aluminum-5356-or-4043r>.
15. Rajan, R.; Kah, P.; Mvola, B.; Martikainen, J. TRENDS IN ALUMINIUM ALLOY DEVELOPMENT AND THEIR JOINING METHODS. *Reviews on Advanced Materials Science*, **2016**, *44*.
16. Haryadi, G. D.; Dewa, R. T.; Ekaputra, I. M. W.; Suprihanto, A. Investigation of post-weld heat treatment (T6) and welding orientation on the strength of TIG-welded AL6061. *Open Eng.*, **2020**, *10*, 753-761.
17. Dewan, M. W.; Wahab, M. A.; Okeil, A. M. Influence of weld defects and postweld heat treatment of gas tungsten arc-welded AA-6061-T651 aluminum alloy. *J. Manuf. Sci. Eng.*, **2015**, *137*, 051027.
18. Dabiri, A.; Mojallal, R. Y.; Ahmadi, E.; Fattahi, M.; Amir Khanlou, S.; Fattahi, Y. J. M. L. Effect of ZrO<sub>2</sub> nanoparticles on the impact properties of shielded metal arc welds. **2015**, *158*, 325-328.
19. Fattahi, M.; Aghaei, V. N.; Dabiri, A.; Amir Khanlou, S.; Akhavan, S.; Fattahi, Y. J. M. S.; A, E. Novel manufacturing process of nanoparticle/Al composite filler metals of tungsten inert gas welding by accumulative roll bonding. **2015**, *648*, 47-50.
20. Fattahi, M.; Mohammady, M.; Sajjadi, N.; Honarmand, M.; Fattahi, Y.; Akhavan, S. J. J. o. M. P. T. Effect of TiC nanoparticles on the microstructure and mechanical properties of gas tungsten arc welded aluminum joints. **2015**, *217*, 21-29.

## **2. CHAPTER 2: Developing High-Strength Al-Si-Mg Filler Metals for Aluminum Fusion Welding**

(Published in the Journal of Materials Engineering and Performance)

### **Abstract**

The 4xxx series of aluminum fillers are extensively used in aluminum welding owing to their excellent weldability, high cracking resistance, and low melting point. However, joints welded with commercial AA4043 fillers experience low mechanical strength. Therefore, we investigated the performance and mechanical strength of joints welded using newly developed Al-Si-Mg filler metals with different Mg contents (0.6–1.4 wt.%). AA6061-T6 plates were welded as the base metal using a gas metal arc welding process. The microstructures of the welded samples were characterized using optical microscopy, scanning electron microscopy, and transmission electron microscopy. The mechanical properties were characterized by microhardness and tensile testing. The results revealed that the new filler metals exhibited weldability similar to that of the ER4043 reference filler. The Mg concentration in the fusion zone of the new fillers was much higher than that of the reference filler. In the as-welded condition, all the fractures occurred outside the fusion zone. Therefore, all the welded samples exhibited similar mechanical strength, much lower than the base metal. After applying the post-weld heat treatment, the mechanical strength of all joints, regardless of the Mg content, reached the same level as the base metal and achieved 100% welding efficiency. Furthermore, the fusion zones were much stronger than the base metal and fusion zone of the reference filler using the new fillers with high Mg content, thus indicating their significant potential for welding high-strength aluminum structures.

**Keyword:** Aluminum fusion welding; Al-Si-Mg filler metals; Magnesium content; Fusion zones; Mechanical strength of joints.

## 2.1 Introduction

The demand for high-strength, weldable 6xxx series Al products is continuously increasing in various transportation industries [1]. The mechanical properties of 6xxx series Al alloys are primarily driven by the number density and volume fraction of metastable  $Mg_2Si$  precipitates. Therefore, the chemical composition (particularly the Mg and Si content) and applied heat treatment process are critical parameters for achieving the desired mechanical properties [2, 3]. Furthermore, since 6xxx series Al products are widely used in car bodies, they are mostly required to be joined by welding. Various welding techniques have been developed to join aluminum components, such as gas metal arc welding (GMAW), laser beam welding (LBW), and friction stir welding (FSW) [4, 5]. Heat-treatable Al-based alloys (i.e., 6xxx alloys) encounter several weldability problems during fusion welding. These include lower strength of the fusion zone (FZ), cracking during welding, reduction of the mechanical strength in the heat-affected zone (HAZ), and high porosity of the weld metal. These defects are related to the filler metal chemistry, propensity towards cracking, and the welding process parameters [6, 7].

Commercial Al-Si-based AA4043 weld wires have been widely used for the general-purpose welding of 6xxx Al products. This filler metal is characterized by high fluidity and high resistance towards weld/solidification cracking. However, as there is no strengthening element (mainly Mg to precipitate  $Mg_2Si$ ) in the AA4043 filler metal, the mechanical properties of the joints are strongly dependent on dilution with the base metal [7]. During the fusion welding process, the Mg content of the 6xxx base metal diffuses to the weld bead,

thus contributing to strengthening via  $Mg_2Si$  precipitation hardening. However, in many situations, the dilution ratio between the base metal and filler wire can fluctuate, influencing the strength of the joints [6].

To improve the properties of weldments, Babu *et al.* [8] added 0.2 and 0.75 wt.% Sc to the AA4043 filler, observing an apparent grain refinement in the weldment when the Sc content was above the hypereutectic composition. In another study by Babu *et al.* [9],  $TiB_2$  was added to the AA4043 fillers as a grain refiner, and the microhardness (HV) of the weldments improved by approximately 20%. The Mg-containing and heat-treatable AA4643 filler metal was also designed to resolve the strengthening variation related to the dilution phenomenon. However, the AA4643 filler still requires dilution from the base metal (approximately 20%) to obtain optimum mechanical properties. In addition, as the AA4643 filler has a lower Si content relative to the AA4043 filler, it has lower fluidity, lower fatigue life, and is more susceptible to hot cracking [6]. Later, AA4943 filler metal, with increased Mg content up to 0.5 wt.%, was developed to provide consistently higher tensile, yield, and shear strength relative to the AA4043 and AA4643 fillers while maintaining the same welding and corrosion characteristics as the AA4043 filler [6]. Although AA4943 filler metal exhibits acceptable strength relative to its conventional 4xxx series counterparts, the increasing demand to develop high-strength weldable Al products necessitates the development of new filler metals. In addition, the influence of Mg, a major alloying element in filler metals, on the mechanical properties of the joints in 6xxx alloys has never been systematically investigated.

Further improvement in the mechanical strength of the joints would also enable manufacturers to decrease the size of fillet welds without compromising strength [7].

Reducing the fillet size could potentially improve welding productivity by reducing the volume of weld wires used and welding process time. In addition, the reduced weld size/thickness could reduce weldment distortion. The objective of the present study is to develop a new generation of 4xxx series filler metals for aluminum fusion welding to obtain high-strength joints with consistent properties. High Mg additions (0.6–1.4 wt.%) were added to the filler metals, and their impact on the weldability, microstructure, and mechanical properties of AA6061 weldments was investigated.

## **2.2 Experimental procedure**

The experimental process is summarized in Figure 2.1. Direct chill (DC) cast billets (diameter of 101 mm) with varying Mg content were prepared to develop new weld wires. After homogenization at 530 °C for 10 h, the DC cast billets were transformed into weld wires (diameter of 1.5 mm) via extrusion and wire drawing processes. The three experimental filler metals containing 0.6, 1, and 1.4% Mg were denoted as Mg0.6, Mg1, and Mg1.4, respectively. A commercial ER4043 weld wire was used as the reference filler metal. The AA6061-T6 plates, as the base metal (BM), were cut into 300 mm × 100 mm × 2 mm sections and prepared in a butt joint configuration with a gap of 0+0.1 mm [10]. GMAW was used to join the plates using a Fronius Transpulse Synergic 5000-CMT welding machine mounted on a Motoman UP50N robot. The chemical compositions of the filler wires and the base metal are listed in Table 2.1. The welding process was conducted with the following parameters: voltage of  $21.6 \pm 0.3$  V, current of  $98 \pm 1$  A, positive direct current electrode, 0.8 m/min as the travel speed, 3m/min as the wire feeding rate, and 100% Ar shielding gas with a flow rate of 24 L/min.

The welded plates were first examined by X-ray radiography tests (XRT) to verify macro-processing defects such as large porosities and cracks in weldments. After the XRT analysis, the welded plates were divided to the high porosity zone, and the low porosity zones. Afterwards, at least four samples from the low porosity zones were grounded and polished then with using the optical microscopy, 20 images were taken from each sample at 50x and analyzed using the ImageJ software. Each image was analyzed, and the pores area fraction was calculated (area of pores / area of the image x 100); subsequently, the average value of the porosity was calculated. Welded samples were prepared using a standard metallographic procedure to examine the microstructural evolution. The microstructures were observed using optical microscopy (OM), scanning electron microscopy (SEM, Jeol JSM-6480LV), and transmission electron microscopy (TEM, Jeol JEM-2100). The welded plates were subjected to post-weld heat treatment (PWHT): 1) solution treatment at 530 °C for 1 h followed by water quenching at ambient temperature, and 2) artificial aging at 170 °C for 6 hr. The mechanical properties of the weldments in the as-welded (AW) and PWHT conditions were evaluated using HV and tensile tests. The Vickers microhardness of the joints was measured on polished samples using an NG-1000 CCD microhardness tester with a load of 50 g and a dwell time of 20 s. The tensile properties of the welded samples were measured using an Instron 8801 servo-hydraulic unit with a crosshead speed of 1 mm/min. An extensometer with a 25 mm gauge length was used to measure the strain. Two types of tensile samples were prepared: standard and double-edge notched samples, as shown in Figure 2.2. At least five samples were obtained for each condition, and the average value was reported.

The polished samples were etched in a solution of 0.5% HF for 5 s to reveal the boundaries between the FZ and HAZ. Identifying the FZ enabled the calculation of the dilution ratio of fillers with BM at the FZ using the equation [11]:  $\text{dilution ratio} = A/(A+B+C)\%$ , where A, B, and C correspond to the cross-sectional areas of the melted BM, weld cap, and weld root reinforcement, respectively (see Figure 2.3). The calculated dilution ratio was approximately 56% for all welded joints; based on this ratio, the chemical compositions of the FZs were calculated (Table 2.2).

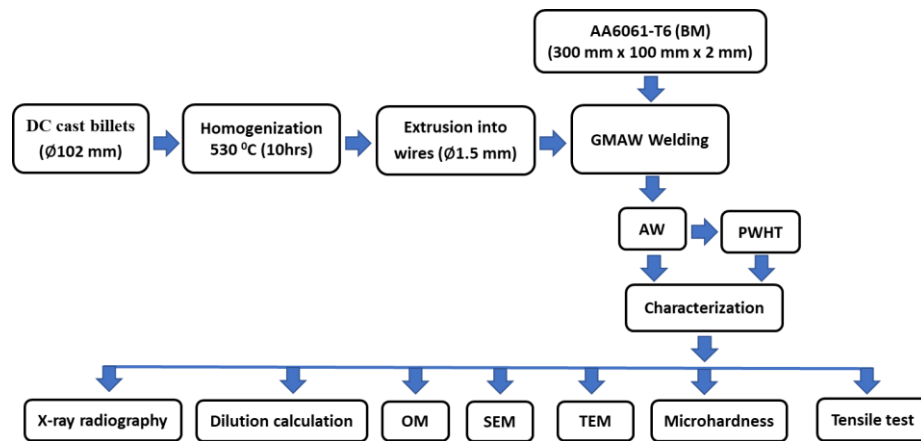


Figure 2.1. Flowchart of the experimental process.

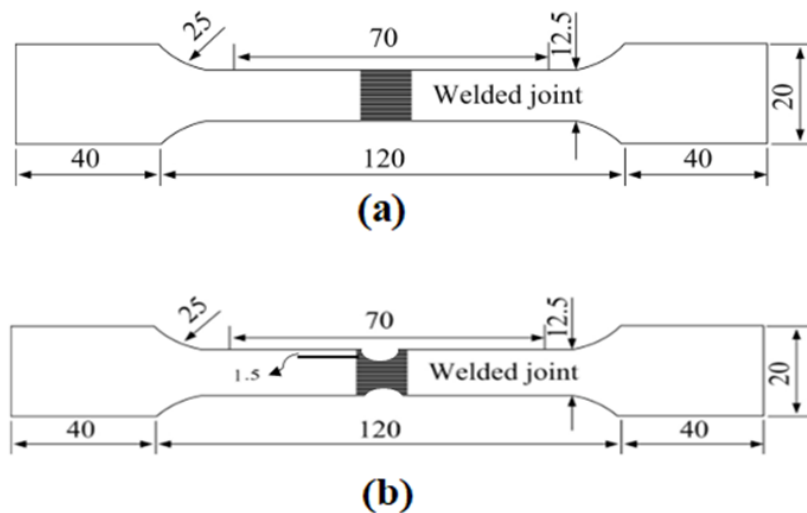


Figure 2.2. Dimension of the tensile samples for (a) standard and (b) double-edge notched samples (mm).

Table 2.1. Chemical compositions of the base metal and filler metals.

ID	Si	Fe	Mn	Mg	Cu
<b>BM (base)</b>	0.52	0.18	0.11	1.05	0.25
<b>ER4043</b>	5.5-6	<0.8	<0.05	<0.05	<0.3
<b>Mg0.6</b>	6.2	0.14	0.5	0.61	0.001
<b>Mg1</b>	6.2	0.15	0.52	1.04	0.001
<b>Mg1.4</b>	6.25	0.15	0.48	1.43	0.001

Table 2.2. The chemical compositions of the FZs calculated after dilution.

Filler	Si	Fe	Mn	Mg	Cu
<b>ER4043</b>	2.478	0.171	0.070	0.599	0.140
<b>Mg0.6</b>	3.009	0.159	0.279	0.835	0.135
<b>Mg1</b>	3.009	0.163	0.288	1.025	0.135
<b>Mg1.4</b>	3.031	0.163	0.271	1.196	0.135

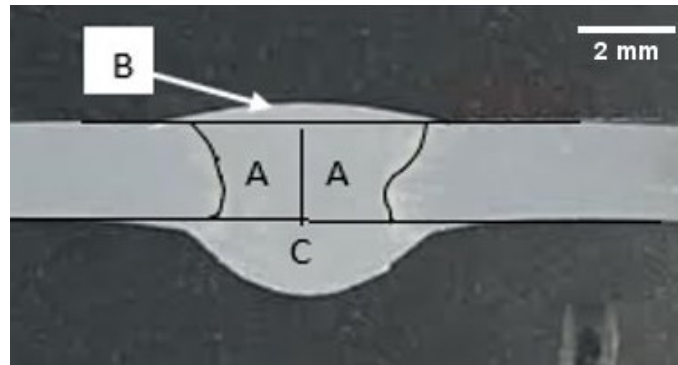


Figure 2.3. Macro view of a typical joint cross section for the dilution calculation.

## 2.3 Results and discussion

### 2.3.1 Weld geometry and imperfection

All weld plates were initially scanned by XRT to verify the integrity of the weld bead and the presence of macro imperfections, such as porosity and cracks. The XRT results showed no signs of slag inclusions, oxides, cracks, lack of fusion, or incomplete penetration for all welded plates, indicating similar weldability of the new filler metals and the reference

ER4043 filler. Two zones, with high and low porosity levels, were observed along the weld bead, as shown in Figure 2.4.

As fillers wires were not the commercial grades (developed at our laboratory), their surface was not perfectly smooth. Even though, at the first step, it was tried to optimize the welding process parameters, but the final weld quality in some region could be influenced by the filler wire quality and generate weld defects (like porosity) in certain zones which named as high porosity zones. The weld cross-sections were extracted from the steady-state region of the weld in the low porosity zones. Based on the macroscopic images, no undercuts on the top or root surfaces were detected. Excessive penetration at the root side was less than 2 mm, passing the stringent quality level B ( $\leq 3$  mm) based on the ISO 10042:2005(E) standard [12]. The porosity content of the low porosity zones, verified by XRT and metallographic analysis, was less than 1%, passing the stringent quality level B ( $\leq 1\%$ ) based on the ISO 10042:2005(E) standard. Consequently, all samples used for microstructure characterization and mechanical property evaluation were prepared from low-porosity zones.

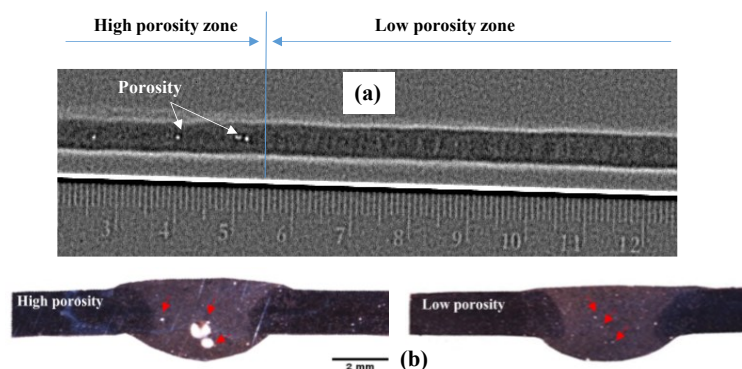


Figure 2.4. (a) XRT image of the weld and (b) macroscopic views of the low and high porosity zones (pores are indicated with red arrows).

## 2.3.2 Microstructures

### 2.3.2.1 As-welded microstructure

The grain morphologies in the BM, HAZ, and FZ were analyzed using OM, and the results are presented in Figure 2.5. The BM (i.e., the as-received 6061-T6 plates) comprise coarse grains (average grain size of 70  $\mu\text{m}$ ) partially elongated in the rolling direction (Figure 2.5(a)). Fine and equiaxed grains with an average size of 40  $\mu\text{m}$  were observed in the HAZ (Figure 2.5(b)); grains in the HAZ were subjected to static recrystallization owing to the heat input during the GMAW process. The fusion boundary between the HAZ and FZ revealed epitaxial growth of the columnar grains. The FZ was composed of dendritic equiaxed grains (average grain size of 130  $\mu\text{m}$ ), as shown in Figure 2.5(c). The second dendrite arm space (SDAS) of the FZ was also similar ( $\sim 16 \mu\text{m}$ ) in all joints. These results indicate that constant weld parameters and similar solidification rates were applied to all welds, which were not influenced by the variation in the Mg content of the fillers.

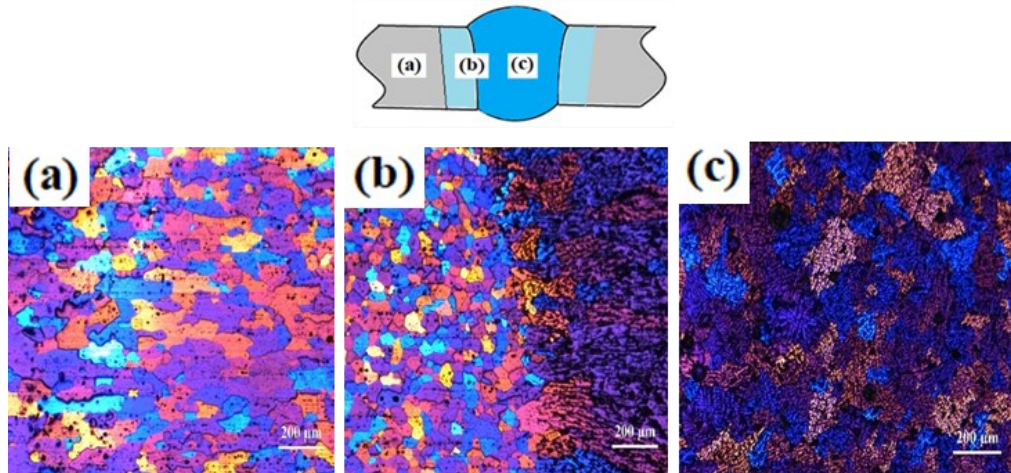


Figure 2.5. Grain morphology of the (a) BM, (b) HAZ, and (c) FZ in the joints welded with Mg1.4 filler.

The microstructure of the FZ was first calculated using the ThermoCalc software under Scheil conditions, using diluted FZ chemical compositions (Table 2.2). The predicted microconstituents and the corresponding mass fractions of the different phases in the ER4043 and Mg1.4 samples are shown in Figure 2.6. The microconstituents in the FZ of both samples were  $\alpha$ -Al, Si, Mg<sub>2</sub>Si,  $\alpha$ -Al(FeMn)Si, and  $\beta$ -AlFeSi. As shown in Figure 2.7, the main differences between these two samples were the content and formation temperatures of Mg<sub>2</sub>Si and the Fe-bearing intermetallics (i.e.,  $\beta$ -AlFeSi and  $\alpha$ -Al(FeMn)Si). Owing to the higher Mg content in the FZ of the Mg1.4 joints, the mass fraction of the Mg<sub>2</sub>Si phase was considerably higher than the ER4043 joints (1.1 vs. 0.4%). Furthermore, considering the higher Mn content in the new fillers, the Fe-bearing intermetallics formed were mostly  $\alpha$ -Al(FeMn)Si in the Mg1.4 joints rather than  $\beta$ -AlFeSi, as in the ER4043 joints.

The microstructures of the FZ of the ER4043 and Mg1.4 joints were further analyzed by SEM (Figure 2.7). The principal microconstituents observed in both samples were  $\alpha$ -Al, Si, Mg<sub>2</sub>Si,  $\alpha$ -Al (FeMn) Si, and  $\beta$ -AlFeSi, consistent with the predicted results (Figure 2.6). Although the Mg content of the ER4043 filler was negligible (>0.05 %), the FZ of the joints contained a small amount of Mg<sub>2</sub>Si particles (~0.2%) due to dilution with the BM. The area fraction of Mg<sub>2</sub>Si particles increased to 0.28, 0.5, and 0.6% in the Mg0.6, Mg1, and Mg1.4 joints, respectively.

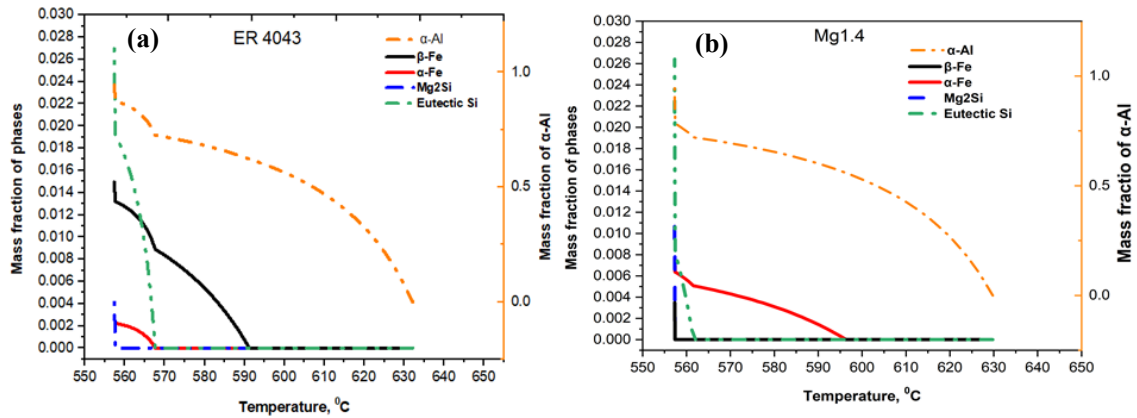


Figure 2.6. Predicted phase amounts of (a) ER4043 and (b) Mg1.4 joints under non-equilibrium Scheil condition.

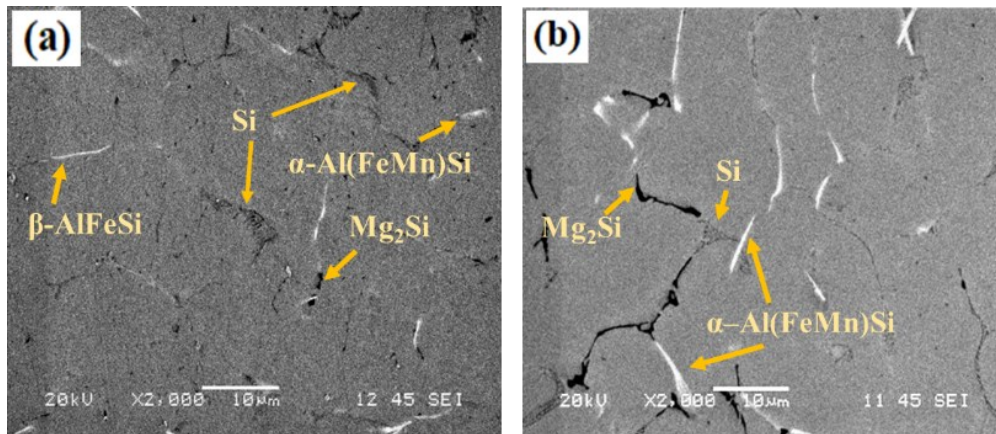


Figure 2.7. SEM images of the FZ of the (a) ER4043 and (b) Mg1.4 joints in the as-welded condition. All phases were identified by SEM-EDX.

### 2.3.2.2 Mg distribution and the weld soundness

The variation in Mg concentration from the weld toe to the weld surface has been previously reported [13,14]. Therefore, the Mg distribution in the FZs was investigated using SEM-EDS, and the results are presented in Figure 2.8. The Mg concentrations at all the weld

surfaces were lower, ranging between 0.2 to 0.29%. The Mg concentration at the weld toe of ER4043 was still relatively low (0.23%). However, at the weld toe of the joints of the new fillers, the Mg concentrations were remarkably higher, and reaching values of 0.72, 0.81, and 0.88% in the Mg0.6, Mg1, and Mg1.4 joints, respectively ( Figure 2.8(a)). Furthermore, the Mg distributions from the weld cap to the weld root were analyzed, and the corresponding results are presented in Figure 2.8 (b). The Mg concentration at the weld roots was significantly higher than that at the weld caps. Overall, the Mg concentration in the FZ of the new fillers was much higher than those of ER4043, where the higher the Mg content of the fillers, the higher the Mg concentration in the FZ. Similar observations on the distribution of Mg in weld beads have been previously reported [15 , 16]. The loss and nonuniform distribution of Mg in the FZs can be attributed to the evaporation and burning of Mg [13 , 14]. Mg can readily evaporate from the weld pool surface due to its low boiling point (1090 °C). In addition, owing to the buoyancy force and lower density of Mg relative to Al, Mg can float to the top surface of the weld pool. Hence, Mg can be vaporized in the hot region of the weld pool surface, underneath the welding arc, and subsequently condense at the weld toes/sides. In the macroscopic view of the weld beads illustrated in Figure 2.7(c)–(e), dark zones (i.e., black smut) were observed in the periphery of the weld beads. The darkness and area of the black smut correlated with the Mg content of the filler; the higher the Mg concentration of the fillers, the larger and darker were the black smuts. As previously reported, the black layer can be attributed to the oxidation of Mg [14 , 17].

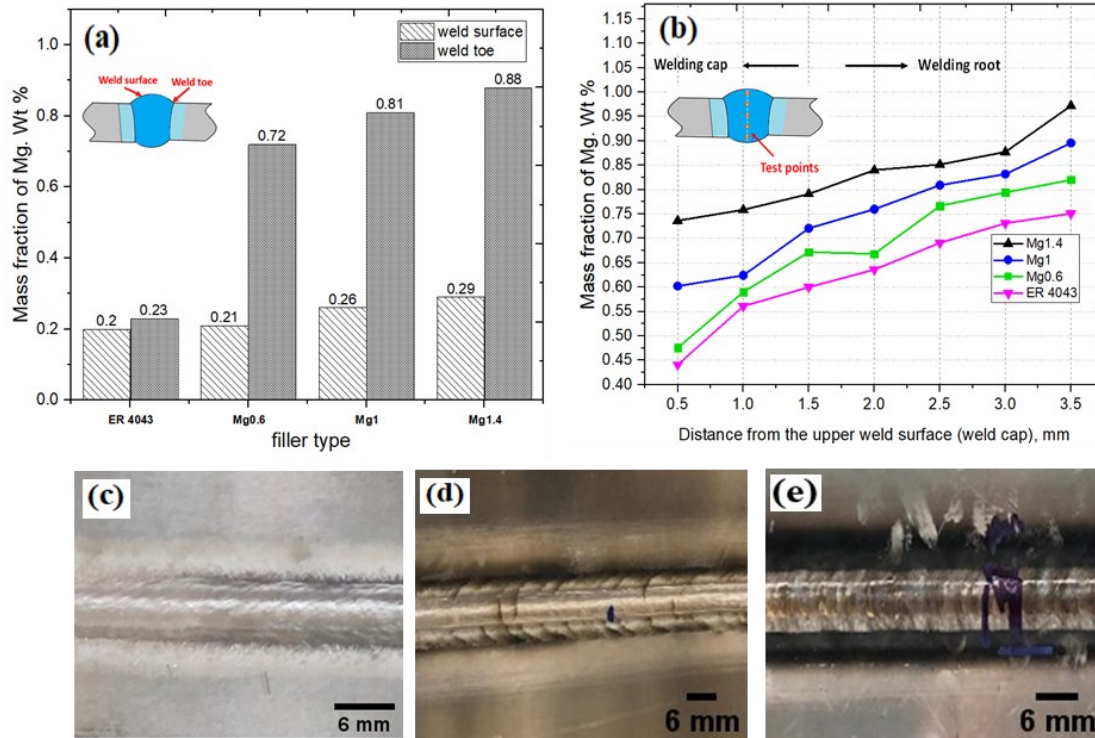


Figure 2.8. (a) Mg concentration at the weld surface and weld toe, (b) Mg distribution along the weld centerline and macro images of the black smut (Mg and Al oxides) around the weld bead in (c) ER4043, (d) Mg0.6, and (e) Mg1.4 joints.

### 2.3.2.3 PWHT microstructure

The microstructure of the FZ after PWHT is shown in Figure 2.9. With the applied heat treatment, the  $Mg_2Si$  and eutectic Si particles were partially dissolved. The remaining  $Mg_2Si$  and Si particles, with plate-like morphology, were modified to a fibrous round structure. The dissolved particles can contribute to strengthening the FZ via solid solution and precipitation hardening [18]. Furthermore, a slight fragmentation of the Fe-bearing intermetallics, marked with dotted circles in Figure 2.9, was observed in the microstructure after the heat treatment.

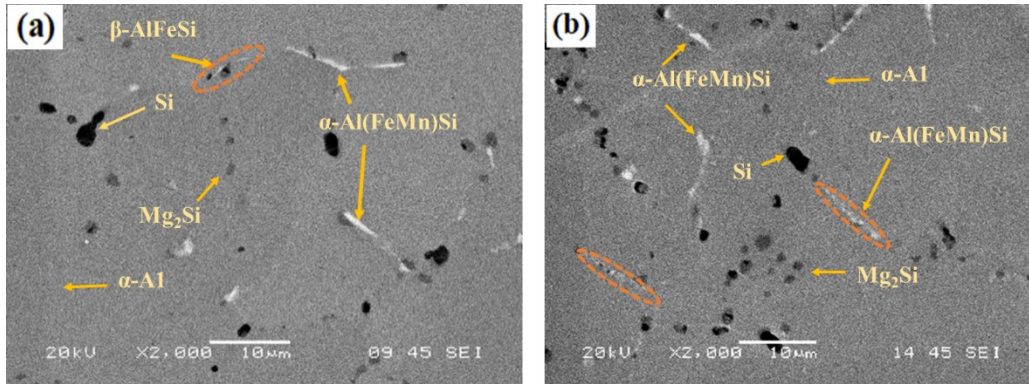


Figure 2.9. SEM images of the FZ in (a) ER4043 and (b) Mg1.4 joints after PWHT.

### 2.3.3 Mechanical properties

#### 2.3.3.1 Microhardness measurement

The microhardness results of the as-welded joints along the central line across the FZ are shown in Figure 2.10(a). The welded samples were divided into three distinct zones based on the HV results. The BM exhibited the highest hardness, with a constant profile (~120 HV), among all the welded samples. The HAZ appeared when the BM moved towards the FZ. Here, a remarkable reduction in HV was observed until reaching the minimum HV, and then the HV value increased again. In the HAZ, the HV values were similar for all welded samples. The large HV reduction in the HAZ can be attributed to recrystallization (Figure 2.5(b)) and the dissolution/coarsening of strengthening precipitates (e.g.,  $\beta''$ -Mg<sub>2</sub>Si) in the BM owing to the arc heat input [11]. With further movement from the HAZ (the softest zone) to the FZ, the HV sharply increased and reached a narrow plateau. The highest HV of the FZ was 115–120 HV for the Mg1.4 sample, similar to the HV of the BM. The HV values of the FZ were reduced to 107 and 104 for the Mg1 and Mg0.6 samples, respectively. The lowest HV of the FZ was 96 HV for the ER4043 sample, approximately 20% lower

compared to that of the Mg1.4 sample. The HV improvement in the FZ by Mg addition could be attributed to solid solution strengthening and possible natural aging prior to HV testing.

After the PWHT, the microhardness of the welded samples was again measured along the centerline of the FZ; the corresponding results are shown in Figure 2.10(b). The microhardness of the BM was ~130 HV, slightly higher than the initial HV of the BM in the as-welded condition (~120 HV). This could be associated with the optimized heat treatment to reach the peak aging in our study. The lost HV of the HAZ was entirely recovered after the PWHT, ensuring that the BM and HAZ exhibited similar HV values. The HV profiles across the FZs were also significantly enhanced compared to those of the as-welded condition. For instance, the HV of the FZ in the ER4043 joint exhibited a 40% improvement (96 vs. 137 HV). In addition, the HV value of the ER4043 joint was slightly higher than that of the BM (137 vs. 130 HV), even though the Mg content in the BM was higher than that in the ER4043 joint. This result can be associated with the excess Si content in the FZ of ER4043 filler, through which a greater volume fraction of  $\beta''$ -Mg<sub>2</sub>Si precipitates were formed [19 , 20], confirmed in Section 2.3.5. Furthermore, the HV values of the FZ welds with the three new fillers were remarkably higher than those of the BM and FZ welds of the ER4043 reference filler. The HV values of the FZs increased from 137 HV for the ER4043 joint to 143, 146, and 148 HV for the Mg0.6, Mg1, and Mg1.4 joints, respectively (Figure 2.10(b)).

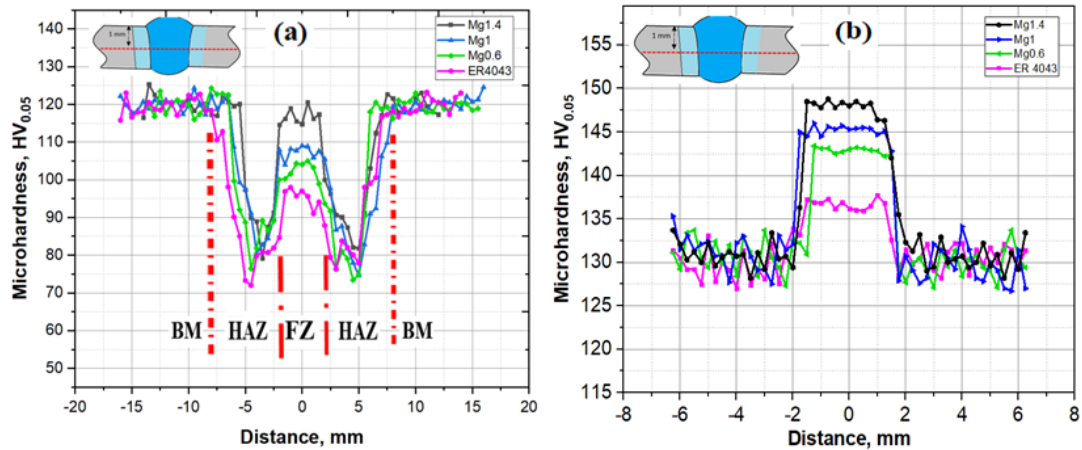


Figure 2.10. Microhardness profiles of the welded joints in (a) as-welded condition and (b) after PWHT.

### 2.3.4 Tensile properties

#### 2.3.4.1 Tensile strengths of standard samples

The tensile strengths of all the welded samples are presented in Figure 2.11. The yield strength (YS) and ultimate tensile strength (UTS) of the BM were 265 and 318 MPa, respectively. In the as-welded condition, all the welded samples with the four filler metals exhibited almost the same YS (~125 MPa) and UTS (~200 MPa), remarkably lower than those of the BM. A close look at the welded samples after tensile testing indicated that all the welded samples made with the four fillers were fractured in the HAZ ( Figure 2.11(b)), which was the softest zone according to the HV results (Figure 2.10(a)), thus explaining the similar tensile strengths exhibited by all the welded samples. It is event that the as-welded tensile properties of all joints reflected only the minimum mechanical strength in the HAZ.

As shown in Figure 2.11(a), the tensile strengths of weld samples with the four fillers were significantly enhanced after the PWHT and reached the same level of tensile strength

of the BM (i.e., YS and UTS of ~275 and ~325 MPa, respectively). The fractures of all the weld samples were again outside the FZ but in the BM ( Figure 2.11(b)). The HV profiles along the welding samples (Figure 2.10(b)) indicate that the strength of the HAZ was entirely recovered after PWHT, and the strength of the FZs made with the four fillers was remarkably higher than that of the BM. The fracture of welded samples occurs in the BM, thus explaining why all the welded samples, regardless of their Mg content, exhibited similar tensile properties as the BM and achieved 100% welding efficiency ( $UTS_{joint}/UTS_{BM} \times 100$ ).

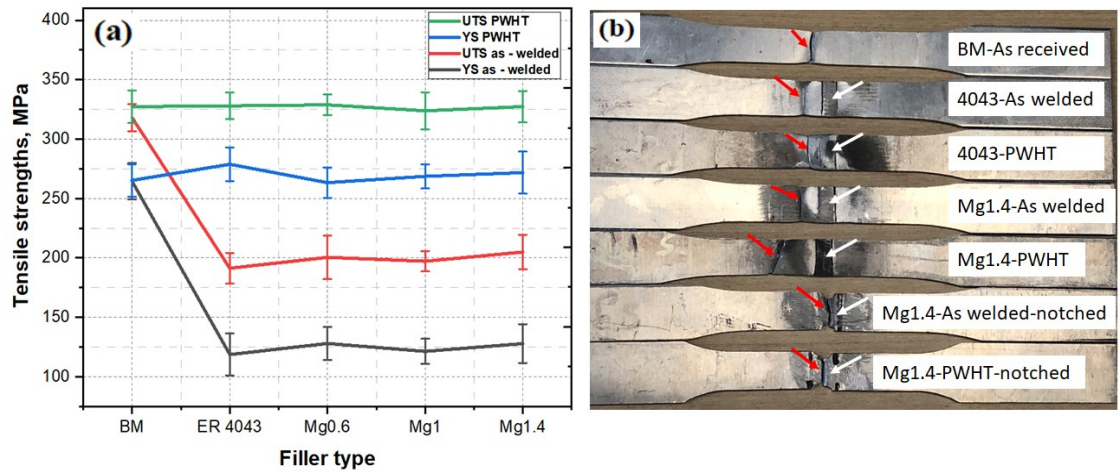


Figure 2.11. (a) Tensile strengths of the standard samples and (b) macro-images of fractured tensile samples under different conditions. The white and red arrows indicate the FZs and the fractures, respectively.

### 2.3.4.2 Tensile strengths of notched samples

As mentioned previously, the standard tensile samples fractured either in the HAZ in the as-welded condition or in the BM in the PWHT condition. Tensile tests in the FZ were conducted with double-edge notched samples to better understand the impact of the elemental contributions (i.e., the Mg content) on the weld bead strength (Figure 2.2(b)). A

correction factor [21 , 22] was applied to correlate the tensile properties of the notched samples to those of the standard tensile samples to obtain the tensile strengths of the FZ. The tensile strengths of the FZs in as-welded condition are shown in Figure 2.12(a). Due to the reduced area of the FZs in the notched tensile samples, all the fractures were located in the FZ (Figure 2.11(b)). The YS and UTS values of the FZ welded with the reference filler reached 148 and 238 MPa, respectively, already higher than that of the HAZ (black and red dashed lines in Figure 2.12(a)). With increasing Mg content, the YS of the FZ made with the new fillers increased up to 179 MPa for the Mg1.4 filler, 20% higher than that of the FZ welded by the reference filler. Moreover, the UTS of the FZs welded by the new fillers was also improved with increasing the Mg content; for instance, for the Mg1.4 filler, the UTS reached 260 MPa, 10% higher than that of the FZ of the reference filler. These improvements in tensile strength, consistent with the microhardness results (Figure 2.10(a)), are mainly attributed to the increased solid solution strengthening of the FZ caused by the higher Mg content in the new fillers [23].

Subsequently, the mechanical strength was evaluated after PWHT, and the results for the notched samples are shown in Figure 2.12(b). The YS and UTS of the FZ made with the reference filler was 288 MPa and 340 MPa, respectively, exceeding the YS and UTS of the BM (275 MPa and 325 MPa, respectively, as marked by the blue and green dashed lines in Figure 2.12(b)). Among the four filler metals, the reference filler exhibited the lowest tensile strength. The tensile strengths of the PWHT joints welded with the new fillers were remarkably higher than those of the joints made with the reference filler. For instance, the joint made with the Mg1.4 filler exhibited a YS of 336 MPa and UTS of 392 MPa. The

higher the Mg content in the filler metals, the higher the tensile strengths of the joints, consistent with the HV results presented in Figure 2.10(b).

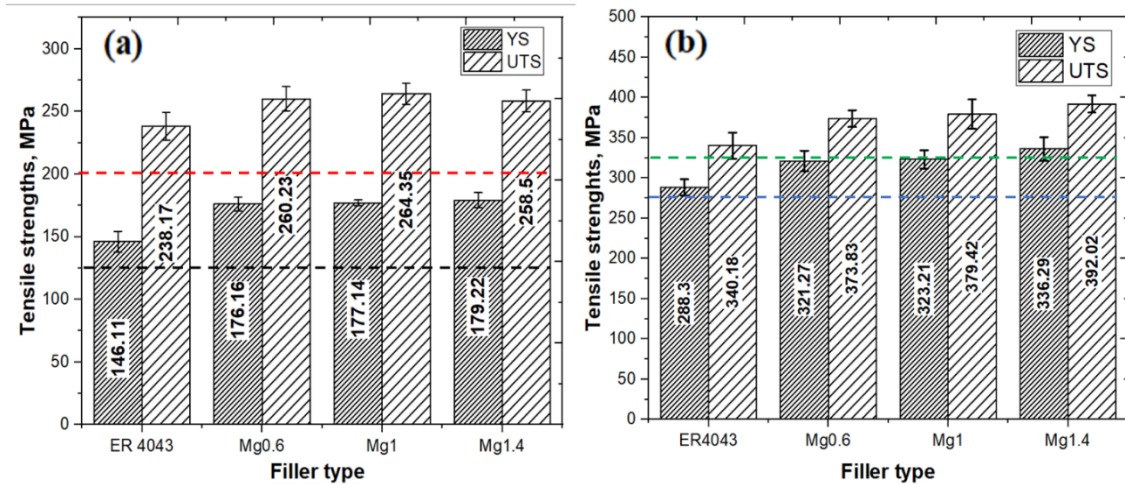


Figure 2.12. Tensile strengths of the notched samples in (a) as-welded and (b) PWHT conditions. The black and red dash lines in (a) represent the YS and UTS of the standard samples in the as-welded condition, while the blue and green dash lines in (b) show the YS and UTS of the standard samples in the PWHT condition.

### 2.3.5 TEM analysis

The HV and tensile results (Figure 2.10(a)) indicated that the HAZ was the softest zone in all the as-welded samples. Therefore, TEM analysis was conducted to characterize the precipitate microstructure in the HAZ and the BM. The bright-field TEM image in Figure 2.13(a) reveals the precipitate microstructure of the BM. It can be seen that very fine and needle-shaped  $\beta''$ -Mg<sub>2</sub>Si precipitates were uniformly distributed in the  $\alpha$ -Al matrix of the BM, which are the main strengthening phase in AA6061-T6 aluminum plates. Figure 2.13(b), taken at ~2 mm from the fusion line of the Mg1.4 joint, the approximate softest point in the HAZ (Figure 2.10(a)), indicated that most of the fine and coherent  $\beta''$ -Mg<sub>2</sub>Si was transformed to equilibrium and large  $\beta$ -Mg<sub>2</sub>Si particles in the matrix as a result of exposure

to high temperature [24 , 25]. Therefore, the strengthening effect on the aluminum matrix was almost completely lost. With increasing distance from the FZ, the effect of the arc heat input during welding was reduced. Figure 2.13(c), taken at ~7 mm from the fusion line of the Mg1.4 joint, showed that the fine and coherent  $\beta''$ -Mg<sub>2</sub>Si were transformed into coarse and semi-coherent  $\beta'$ -Mg<sub>2</sub>Si precipitates, resulting in a partial loss of the strengthening effect. In addition, the grains in the HAZ were mostly recrystallized due to the effect of the arc heat input (Figure 2.5(b)). The microstructure evolution in the HAZ, related to the heat flux during welding, accounts for the softening of the HAZ, resulting in the weakest zone in all the as-welded samples.

The precipitate microstructure in the FZ of the PWHT samples was investigated using TEM. Typical results for the FZ made with the ER4043, Mg0.6, and Mg1.4 fillers are presented in Figure 2.14(a) to (c). The quantitative results of the number densities and volume fractions of the  $\beta''$ -Mg<sub>2</sub>Si precipitates in the BM and all the welded samples are shown in Figure 2.14(d). The microstructures of the FZs in all the welded samples were dominated by nanosized and coherent  $\beta''$ -Mg<sub>2</sub>Si precipitates (Figure 2.14(a)). The FZ of the reference filler had a slightly higher number density and volume fraction of precipitates than the BM (Figure 2.14(a)), although the BM had a higher Mg content, attributed to the higher excess Si content in the ER4043 joint, promoting the formation of  $\beta''$ -Mg<sub>2</sub>Si precipitates [19]. With increasing Mg content in the new fillers, the  $\beta''$ -Mg<sub>2</sub>Si precipitates became finer (Figure 2.14(b) and (c)), and the number density and volume fraction of precipitates increased (Figure 2.14(d)). Therefore, compared to the BM and the reference filler joint, the higher HV (Figure 2.10(b)) and greater tensile strength ( Figure 2.12(b)) of the FZs of the new fillers were directly related to the finer and denser  $\beta''$ -Mg<sub>2</sub>Si precipitates. After the

PWHT, the HAZ of the welded samples recovered to the original strength of the BM. However, the FZs welded by the new fillers became much stronger; hence, the weld beads are no longer the limiting factor for the overall strength of the welded components, thus indicating the significant potential for the welding of high-strength aluminum structures.

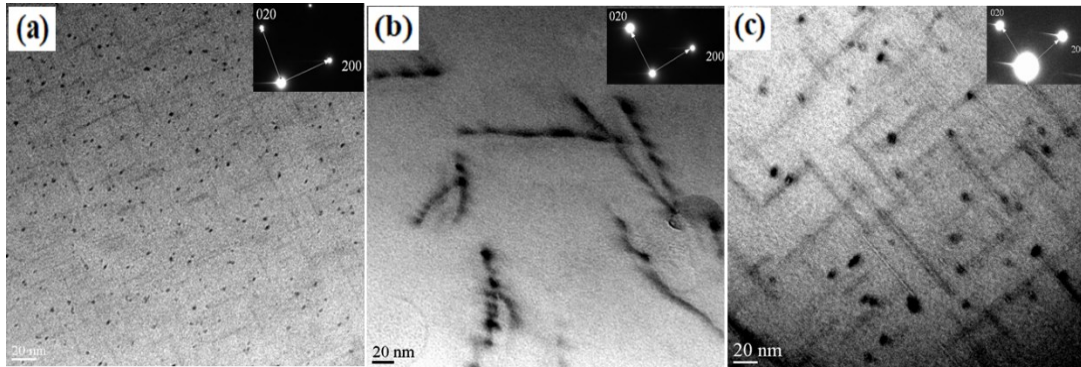


Figure 2.13. Bright-field TEM images of (a)  $\beta''$  precipitates in BM, (b)  $\beta$  precipitates at 2 mm from the fusion line, and (c)  $\beta'$  precipitates at 7 mm from the fusion line in the Mg1.4 joint.

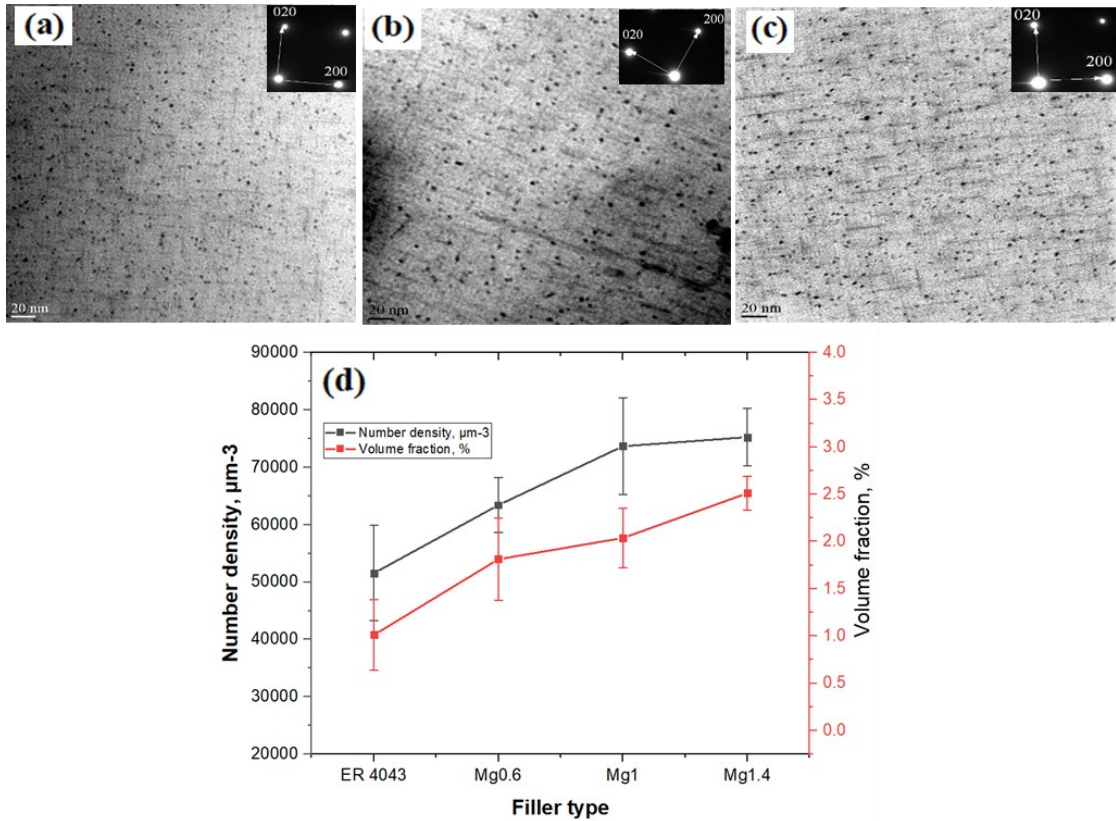


Figure 2.14. Bright-field TEM images of  $\beta''$  precipitates in the FZs of (a) ER4043, (b) Mg0.6, (c) Mg1.4 joints. (d) Quantitative results of the  $\beta''$  precipitates.

## 2.4 Conclusion

- 1) The new Al-Si-Mg 4xxx filler metals exhibited weldability similar to that of the ER4043 commercial filler. No slag inclusions, oxides, cracks, lack of fusion, or incomplete penetration were observed for any of the welded plates.
- 2) In the joints of all the filler metals, the Mg concentration varied significantly from the weld surface to the weld toe and from the weld root to the weld cap. The average Mg concentration in the FZ of the new fillers was much higher than that of the reference filler, increasing with increasing Mg content in the new fillers.
- 3) In the as-welded condition, all the welded samples exhibited similar mechanical strength, but much lower than the BM. The strength of the FZ was greater than the minimum strength

of the HAZ for any given filler. Therefore, all the welded samples were fractured at the HAZ, the weakest zone in the joints owing to recrystallization and the dissolution/coarsening of the strengthening precipitates.

- 4) After applying the PWHT, the mechanical strength of all joints, regardless of the Mg content, reached the same level as the BM, achieving 100% welding efficiency.
- 5) The results of the microhardness and notched tensile samples indicated that although the HAZ of the welded samples was recovered during PWHT, the FZs welded by new fillers became much stronger than the BM and the joint made by the reference filler, thus indicating the significant potential for the welding of high-strength aluminum structures. The improved strength of the FZs was attributed mostly to the finer and denser  $\beta''$ -Mg<sub>2</sub>Si owing to the higher Mg content in the FZs made by new fillers compared to that made by the reference filler.

## 2.5 References

1. W. Miller, L. Zhuang, J. Bottema, A.J. Wittebrood, P. De Smet, A. Haszler, and A. Vieregge, Recent Development in Aluminium Alloys for the Automotive Industry, *Mater. Sci. Eng., A*, 2000, **280**(1), p 37-49
2. J.S. Pérez, R.R. Ambriz, F.F.C. López, and D.J. Viguera, Recovery of Mechanical Properties of a 6061-T6 Aluminum Weld by Heat Treatment after Welding, *Metall. Mater. Trans. A*, 2016, **47**(7), p 3412-3422
3. A. Lakshminarayanan, V. Balasubramanian, and K. Elangovan, Effect of Welding Processes on Tensile Properties of Aa6061 Aluminium Alloy Joints, *Int. J. Adv. Manuf. Technol.*, 2009, **40**(3), p 286-296
4. A.W. AlShaer, L. Li, and A. Mistry, Effect of Filler Wire Properties on Porosity Formation in Laser Welding of Ac-170px Aluminium Alloy for Lightweight Automotive Component Manufacture, *Proc Inst Mech Eng B J Eng Manuf*, 2017, **231**(6), p 994-1006
5. I. Guzmán, E. Granda, J. Acevedo, A. Martínez, Y. Dávila, and R. Velázquez, Comparative in Mechanical Behavior of 6061 Aluminum Alloy Welded by Pulsed Gmaw with Different Filler Metals and Heat Treatments, *Materials*, 2019, **12**(24), 4157
6. B. Anderson, T. Anderson, G. White, and P. Berube, A New Development in Aluminum Welding Wire: Alloy 4943, *Weld. J.*, 2013, **92**(7), p 32-37
7. Anderson, Stephen L, Anderson, Bruce E, Aluminum Welding Filler Metal, Casting and Wrought Metal Alloy (U.S. Patent No. 2015/0132181 A1) , 2015.
8. N.K. Babu, M.K. Talari, D. Pan, Z. Sun, J. Wei, K.J.M.C. Sivaprasad, and Physics, Microstructural Characterization and Grain Refinement of AA6082 Gas Tungsten Arc Welds by Scandium Modified Fillers, 2012, **137**(2), p 543-551
9. N.K. Babu, M.K. Talari, P. Dayou, S. Zheng, W. Jun, and K. SivaPrasad, Influence of Titanium–Boron Additions on Grain Refinement of AA6082 Gas Tungsten Arc Welds, *Mater. Des.*, 2012, **40**, p 467-475
10. Aluminum Filler Alloy Selection Chart, (AlcoTec Wire Corporation) [http://alcotec.com/us/en/support/upload/Aluminum\\_Filler\\_Alloy\\_Selection\\_Chart.pdf](http://alcotec.com/us/en/support/upload/Aluminum_Filler_Alloy_Selection_Chart.pdf), 2015.
11. Y. Liang, J. Shen, S. Hu, H. Wang, and J. Pang, Effect of Tig Current on Microstructural and Mechanical Properties of 6061-T6 Aluminium Alloy Joints by Tig–CMT Hybrid Welding, *J. Mater. Process. Technol.*, 2018, **255**, p 161-174

12. Technical committee ISO/TC 44, Welding - Arc-Welded Joints in Aluminium and Its Alloys - Quality Levels for Imperfections, ISO 10042:2005(E), ISO, 2005, p 1-27
13. T.E. Borchers, D.P. McAllister, and B. Zhang, Macroscopic Segregation and Stress Corrosion Cracking in 7xxx Series Aluminum Alloy Arc Welds, *Metall. Mater. Trans. A*, 2015, **46**(5), p 1827-1833
14. H.-k. Lee, T.-j. Yoon, and C.-y. Kang, Analysis of Spatter Formation Phenomena on Mig and Plasma-Mig Hybrid Weld of Cryogenic Al-Mg Alloy, *J. Korean Inst. Met. Mater*, 2016, **54**(2), p 79-88
15. X. Zhan, J. Chen, J. Liu, Y. Wei, and J.M. Zhou, Microstructure and Magnesium Burning Loss Behavior of Aa6061 Electron Beam Welding Joints, *Mater. Des.*, 2016, **99**, p 449-458
16. L. Zhou, M. Zhang, X. Jin, H. Zhang, and Mao, Study on the Burning Loss of Magnesium in Fiber Laser Welding of an Al-Mg Alloy by Optical Emission Spectroscopy, *Int. J. Adv. Manuf. Technol.*, 2017, **88**(5-8), p 1373-1381
17. H.-K. Lee, K.-S. Chun, S.-H. Park, and C.-Y. Kang, Control of Surface Defects on Plasma-Mig Hybrid Welds in Cryogenic Aluminum Alloys, *Int. J. Nav. Archit. Ocean Eng*, 2015, **7**(4), p 770-783
18. J.-h. Peng, X.-l. Tang, J.-t. He, and D.-Y. Xu, Effect of Heat Treatment on Microstructure and Tensile Properties of A356 Alloys, *Trans. Nonferrous Met. Soc. China*, 2011, **21**(9), p 1950-1956
19. A. Gupta, D. Lloyd, and S.J.M.S. Court, Precipitation Hardening in Al–Mg–Si Alloys with and without Excess Si, *Mater. Sci. Eng., A*, 2001, **316**(1-2), p 11-17
20. J. Rakhmonov, K. Liu, P. Rometsch, N. Parson, and X. Chen, Improving the Mechanical Response of Al–Mg–Si 6082 Structural Alloys During High-Temperature Exposure through Dispersoid Strengthening, *Materials*, 2020, **13**(22), p 5295
21. J. Choung, and S. Cho, Study on True Stress Correction from Tensile Tests, *J. Mech. Sci. Technol*, 2008, **22**(6), p 1039-1051
22. V. Olden, Z. Zhang, E. Østby, B. Nyhus, and C. Thaulow, Notch Tensile Testing of High Strength Steel Weldments, 2nd international symposium on high strength steel, 2002

23. O. Myhr, Ø. Grong, H. Fjær, and C. Marioara, Modelling of the Microstructure and Strength Evolution in Al–Mg–Si Alloys During Multistage Thermal Processing, *Acta Mater.*, 2004, **52**(17), p 4997-5008
24. L. Zhang, X. Li, Z. Nie, H. Huang, and J. Sun, Softening Behavior of a New Al-Zn-Mg-Cu Alloy Due to Tig Welding, *J. Mater. Eng. Perform.*, 2016, **25**(5), p 1870-1879
25. M. Peel, A. Steuwer, and P. Withers, Dissimilar Friction Stir Welds in AA5083-AA6082. Part II: Process Parameter Effects on Microstructure, *Metall. Mater. Trans. A*, 2006, **37**(7), p 2195-2206.

### **3. Chapter 3: Welding of AA6061-T6 Sheets Using High-Strength 4xxx Fillers: Effect of Mg on Mechanical and Fatigue Properties**

(Published in the Journal of Materials)

#### **Abstract**

Al-Si-Mg 4xxx filler metals are widely used in aluminum welding due to excellent weldability and capability of strength enhancement by heat treatment. However, the weld joints with commercial ER4043 filler often suffer low strength and low fatigue properties. In the present work, two novel fillers were designed and prepared by increase Mg level in 4xxx filler metals, and the effect of Mg on mechanical and fatigue properties was studied in as welded and post-weld heat treatment (PWHT) conditions. AA6061-T6 sheets was welded as the base metal using a gas metal arc welding technique. The results show that increasing Mg content in the fillers metals provided higher microhardness and tensile strength of weld joints compared to the reference 4043 filler. The joints made by novel fillers with high Mg content (0.6-1.4 wt.%) displayed higher fatigue strengths and loner fatigue lives compared to the joint made by the reference filler in both as welded and PWHT conditions. The joint with the filler containing 1.4 wt.% Mg exhibited the highest fatigue strength and best fatigue life among all three joints studied. The improved mechanical strength and fatigue properties in aluminum joints were attributed to the enhanced solid solution strengthening of Mg in as welded condition and the increased precipitation strengthening of  $\beta''$  in PWHT condition.

**Keyword:** Aluminum welding; Al-Si-Mg 4xxx filler metals; Mg addition; Mechanical strength, Fatigue properties.

### 3.1 Introduction

Nowadays aluminum alloys find widespread use in various applications such as bridges, automobiles, airplanes, and building construction. The diverse nature of these applications requires various approaches to join the aluminum components to form a complete assembly. Fusion welding is the primary method used for joining the assembly, and a proper filler metal is essential to achieve the desirable strength and to mitigate welding defects such as porosity and hot cracking [1, 2]. New welding techniques have emerged for metal welding, including friction stir welding, laser welding, and electron beam welding. Despite those developments, conventional welding techniques such as tungsten inert gas (TIG) and gas metal arc welding (GMAW) are still prevalent in the industry due to their ability for quick welding, deep penetration, and ease of use on-site [3]. For welding Al-Mg-Si 6xxx materials, commercial Al-Si-based ER4043 filler metal is widely used. During fusion welding, this filler metal exhibits good fluidity and high weld crack resistance. However, the mechanical properties of such joints are generally low and vary largely, depending on the dilution of alloying elements from the base 6xxx materials as the ER4043 filler metal contains only high Si but without Mg.

Many attempts were made to achieve a consistent high-strength joint for 6xxx materials. Anderson [4] attempted to modify the composition of ER4043 filler by adding 0.4% Mg to make it heat-treatable. The modified alloy, named ER4943, exhibited higher tensile strength in weld joints compared to ER4043 joints in both as welded and post-weld heat treatment conditions (PWHT). However, the joint strength of ER4943 was still lower than that of the base AA6061-T6 materials. Perez et al. [2] studied the effect of Mg addition on the welding performance and mechanical properties of AA6061-T6 joints. The results indicated that the

added Mg could enhance the fusion zone strength. However, little work has been done to explore the effect of Mg levels on other mechanical performance of 6xxx joint, such as the fatigue properties [5].

Fatigue properties of aluminum alloy joints play an important role on the safe and reliable structural applications [6], and studies show that 90% of engineering constructions fail due to fatigue [7]. Researchers have found that excess solute Mg in 6xxx alloys can improve fatigue strength and fatigue life [8-12]. Takahashi [9] reported that the fatigue strength and fatigue life could be improved in an excess Mg in 6xxx alloys where Mg persisted as soluble atoms in the matrix. The author added 0.5% and 0.8% excess Mg to a stoichiometric  $Mg_2Si$  composition AA6061-T6 alloy and found that excess Mg in AA6061-T6 alloys increased work hardening and produced cyclic slip resistance for the crack growth. In addition, the excess solute Mg caused a dynamic strain aging, which made easier for fatigue cracks to stop propagating by slowing down the motion of mobile dislocations [8, 9].

Al-Mg-Si 6xxx alloys are heat treatable, and the precipitation of  $\beta''/\beta'$   $Mg_xSi_y$  after T6 heat treatment can hinder dislocation movements and hence improve the mechanical properties of aluminum alloys. The effect of  $\beta''$  precipitates on the fatigue properties was investigated [2]. It was reported that the PWHT of AA6061-T6 joints welded with ER4043 filler resulted in a significant improvement in fatigue strength compared to the as welded condition, due to the formation of  $\beta''$  precipitates resulting from Mg via the base metal dilution. Many works studies the interaction between dislocations and precipitates [11, 13-15]. Their results revealed that the moving dislocations could share the coherent or semi-coherent precipitates, and therefore, their number density increased via sharing leading to

enhance the resistance against the dislocation movements and hence increase the fatigue strength.

The formation of porosity in the fusion welding is difficult to completely eliminate, and the selection of the proper fillers and optimizing the welding parameters can reduce its content [16]. Morton [17] demonstrated a linear relationship between the porosity area and the decrease in weld fracture strength in TIG-welded AA2xxx aluminum alloy. According to Wang et al. [18], A356 castings that contained high porosity exhibit a fatigue life at least one order of magnitude lower than those free of porosity. Gao et al. [19] and Caton et al. [20] studied the effect of porosity on the fatigue life of 356 cast alloys. They reported that the pore size and nearest pores to the surface critically influenced the crack initiation and fatigue lifetime. Linder et al. [21] studied the effect of porosity on the fatigue strength of high-pressure die-cast AlSi12Cu3 aluminum alloy. The results revealed that the increase of pore fraction from 0.7% to 1.6% reduced the fatigue strength by approximately 15% for notched specimens.

Recently, the demand to develop high-strength weldable aluminum products is intensively increased, and consequently it necessitates the development of new filler metals. In the present work, the effect of the addition of Mg in 4xxx filler metals on the tensile properties and fatigue strength of A6061-T6 joints was investigated by adding 0.6 and 1.4 % Mg. The ER4043 filler (free Mg) was used as a reference compared with the newly developed high Mg filler metals. The microstructure and mechanical performance of welded samples were analyzed under both as welded and PWHT conditions. Moreover, the effect of the porosity size on the fatigue strength was studied. The fracture analysis of the fatigue

fractured samples was performed to explain the effect of the Mg addition on the fatigue properties.

### **3.2 Experimental procedure**

AA6061-T6 sheets, as the base metal (BM) with a dimension of  $500 \times 100 \times 2$  mm, were welded by the novel filler wires using the gas metal arc welding (GMAW) technique. The filler wire manufacture and the welding process are illustrated in Figure 3.1. Two novel filler wires with different Mg contents (0.6 and 1.0 %), designated as FMg0.6 and FMg1.4, were fabricated and used. In addition, a commercial ER4043 filler wire was also included in the experiment as the control base. The chemical compositions of the BM along and three filler wires is listed in Table 3.1. A Fronius Transpulse Synergic 5000-CMT welding equipment mounted on a Motoman UP50N robot was utilized for welding the sheets in the butt joint configuration with a gap size of  $0 \pm 0.1$  mm. The welding parameters and the X-ray radiography examination for welded sheets were reported in our previous work [22]. The welded sheets were subjected to a post-weld heat treatment (PWHT) including a solution treatment at 530 °C for 1 h, followed by water quenching at room temperature and aging at 170 °C for 6 h.

To characterize the microstructure, the welded samples were subjected to a standard grinding and polishing procedure. Optical microscopy (OM), scanning electron microscopy (SEM, Jeol JSM-6480LV), and transmission electron microscopy (TEM, Jeol JEM-2100) were employed to study the microstructure evolution. The transverse microhardness profiles were performed using an NG-1000 CCD microhardness tester by applying a load of 50 g and a dwell time of 20 s on polished samples.

The tensile and the high cyclic fatigue (HCF) tests were performed using Instron 8801 servo-hydraulic machine in as-welded (AW) and PWHT conditions. Based on the X-ray radiographic results, the samples were selected from the low porosity zone to reduce the effect of the porosity on these properties. As shown in Figure 3.2, the standard and notched tensile samples were used. Given that the standard samples were cracked outside the fusion zone (FZ), the notched samples were designed to characterize the strength of the FZ. For the fatigue tests, the standard samples were mirror polished to remove surface inhomogeneity. The tests were conducted at ambient temperature with applying a sinusoidal waveform at a frequency of 20 Hz and a cyclic stress ratio of 0.1. To plot the fatigue S-N curve, the statistic approach of the ISO 12107:2003 standard was used. As aluminum alloys usually do not present a fatigue limit, the fatigue tests were stopped at the cycle number of  $10^7$ .

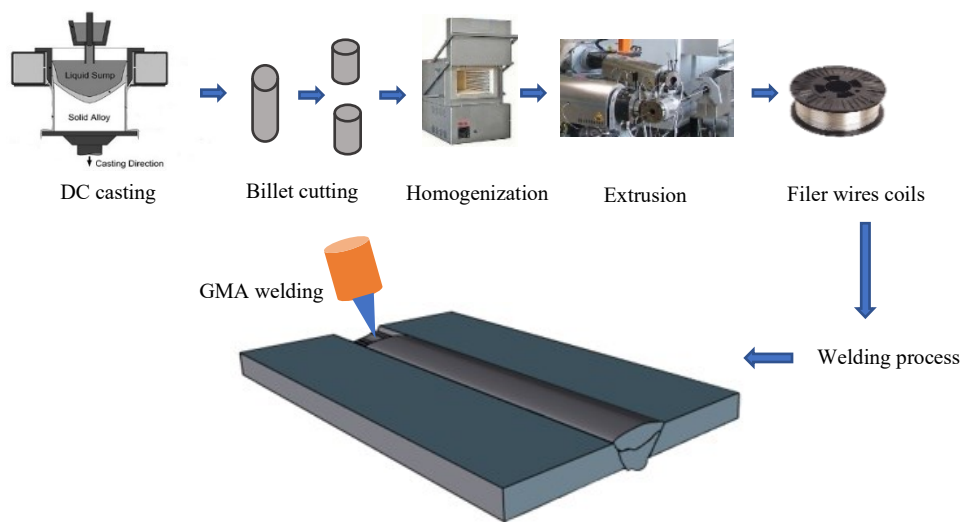


Figure 3.1. Schematic of the filler wire manufacture and welding process.

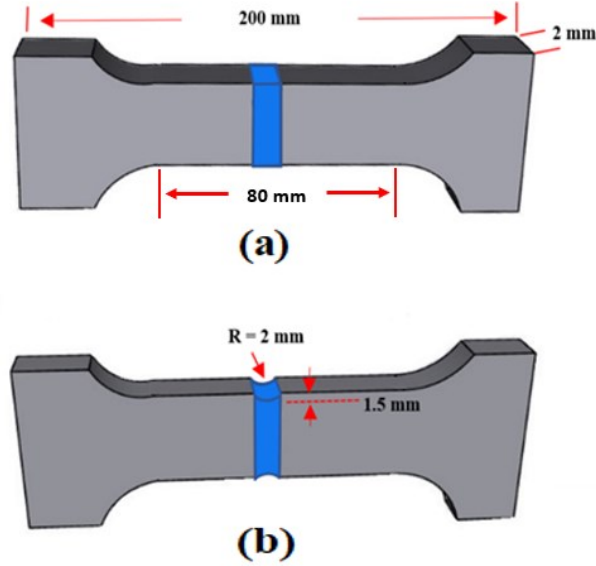


Figure 3.2. Dimension of the samples (a) standard samples for tensile and fatigue tests and (b) double-edge notched samples for tensile test [11, 23, 24].

Table 3.1. Chemical compositions of the base metal and filler wires.

ID	Si	Fe	Mn	Mg	Cu
BM (base)	0.52	0.18	0.11	1.05	0.25
ER4043	5.5-6	<0.8	<0.05	<0.05	<0.3
FMg0.6	6.23	0.14	0.23	0.6	0.001
FMg1.4	6.4	0.18	0.28	1.4	0.001

### 3.3 Results and discussion

#### 3.3.1 Welding defect analysis

The results of the X-ray radiography test (XRT) and the optical macrographs from the cross section of the FZs are shown in Figure 3.3. A uniform weld deposit with no sign of hot cracking, slag inclusions, oxides, or incomplete penetration were observed in all the welded samples. Two porosity zones with low and high porosity levels were observed in the fusion zones (FZ) as shown in Figure 3.3 (a). The high porosity zone was partially caused by using homemade filler wires with non-perfect smooth surface. Since X-ray radiography test cannot

detect the undercuts defects, the metallographic macroimages were taken as shown in Figure 3.3(b). No sign of undercuts on top or root surfaces as well as macroporosity were observed. Figure 3.3(c) displays optical microscopy image of the low porosity zone as example of FMg1.4 joints. The porosity in this zone was a combination of the gas and shrinkage pores. The gas pores were mostly round shape (red arrows) and of larger size relative to the irregular shrinkage pores (yellow arrows) [25].

The statistical analysis of the porosity was performed using two methods, the XRT and the metallographic one, and the results is illustrated in Figure 3.3(d). The XRT utilized the whole radiographic images of the welded samples to estimate the overall porosity and the average percentage of the porosity was calculated for all the weld seams. The porosity levels of two newly developed filler joints were higher than the commercial ER4043 filler joint, and were  $0.3\% \pm 0.03$  (area of pores in the weld area of the whole weld seam), which is still in an acceptable rang (quality level B < 1%) according to ISO 10042:2005(E) standard [26]. Although the XRT is appreciated in revealing the macro defects, it had difficulty to examine the micro defect under the size of  $100 \mu\text{m}$  due to the spatial resolution and signal-to-noise sensitivity [27]. Therefore, the metallographic analysis was performed in the low porosity zones of all of filler joints. The average percentages of porosity in three filler joints were found to be  $0.1\% \pm 0.05$  (Figure 3.3(d)). Based on these results, the samples for the mechanical property characterizations were chosen from the low porosity zone aiming to reduce the effect of the weld defects and to better reveal the impact of the added Mg.

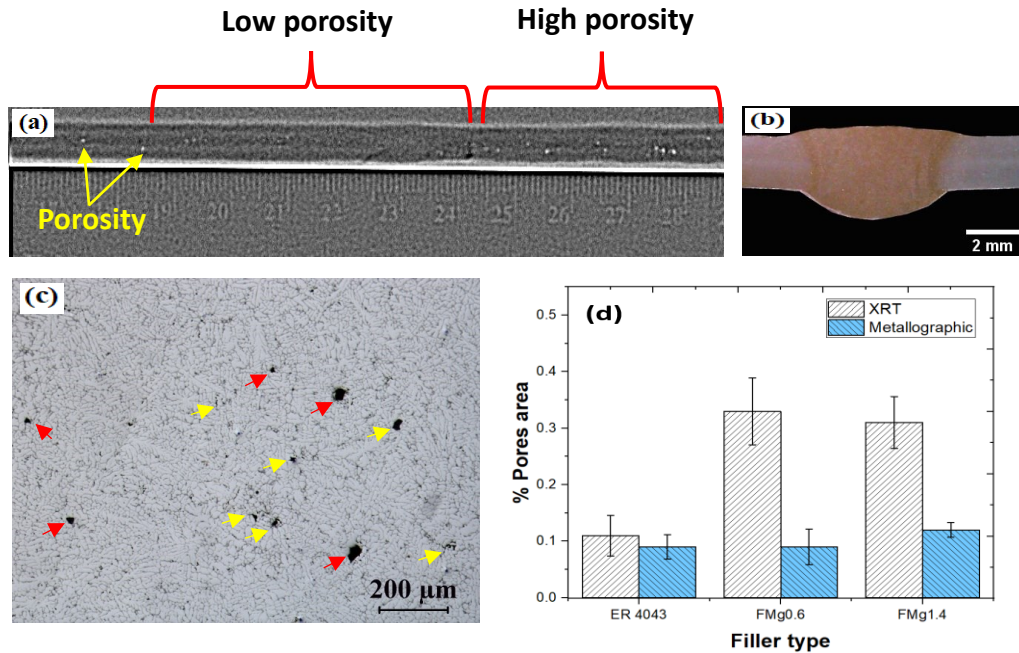


Figure 3.3. a) X-ray radiography results, b) macroimage of the cross-section of FMg1.4 joints, c) the optical microimage of porosity in the low porosity zone (The red arrows for gas pores and yellow arrows for shrinkage porosity), and d) the overall area fraction of the pores with XRT and the area fraction of the pores in the low porosity zone with metallographic analysis.

### 3.3.2 Mechanical properties

#### 3.3.2.1 Microhardness

The microhardness profiles across the mid-thickness of the as-weld and PWHT specimens are displayed in Figure 3.4 (a). The hardness values varied significantly across the mid-thickness, through which the three principal zones of the welded samples (i.e., BM, HAZ and FZ) can be distinguished. The average HV values of three filler joints, corresponding to each zone in as-weld and PWHT conditions are shown in Figure 3.4(b). For the as welded condition, the highest hardness of 122 HV was measured in BM, while the lowest value (i.e.,  $80 \pm 4$  HV) was measured in the HAZ zone in ER4043 joint. The HV in

HAZ was slightly improved with increasing Mg content in novel filler wires. The sharp drop of the HV values in the HAZ was related to dissolution/coarsening of the precipitates [22]. The HV values were enhanced by moving toward the FZs owing to the solid solution strengthening. The HV in FZ increased from 95 HV in ER4043 to 102 HV in FMg0.6 and further to 110 HV in FMg1.4. After applying the PWHT, the HV values in HAZ were retrieved and became equal to the BM. Furthermore, the HV values in FZ of all the filler joints were higher than that of BM. The HV increased with increasing Mg content of filler wires, and it enhanced from 137 HV in ER4043 to 140 HV in FMg0.6 and further to 145 HV in FMg1.4 in the PWHT condition, respectively.

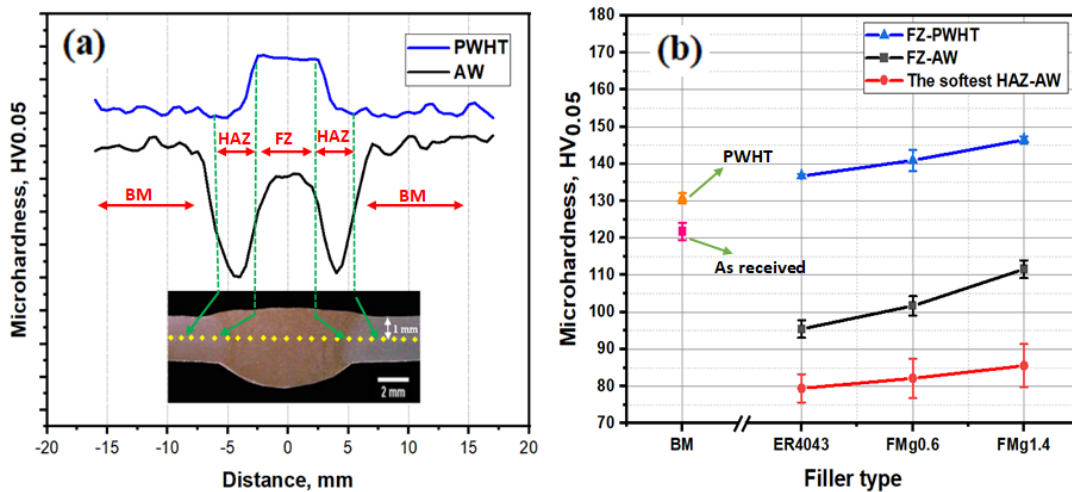


Figure 3.4. (a) Schematic of microhardness profiles and location in as welded and PWHT condition, (b) The average of the microhardness in the FZs and HAZs of three filler joints in as welded and PWHT conditions.

### **3.3.2.2 Tensile Strength**

#### **3.3.2.2.1 The tensile strength of the standard samples**

It is common in aluminum welding that the FZ has the lowest strength relative to the BM and even to the HAZ [2, 28-30]. This is often observed in aluminum 6xxx alloy welding using the commercial fillers of the 4xxx series, such as ER4043. The addition of Mg to the Al-Si filler metals can improve the mechanical strength by a combination of solid solution strengthening and precipitation hardening [31].

The tensile strength results of the BM and the joints with standard samples are shown in Figure 3.5(a). In as weld condition, all the joints exhibited similar tensile strength results because the as welded samples were all fractured in the HAZ. The UTS and YS of the samples were approximately 200 MPa and 150 MPa, respectively, whereas the UTS and yield of the as received BM were 325 and 275 MPa, respectively. The tensile results and the HV results are consistent (Figure 3.4(b)), as both indicate that HAZ was the softest zone. With the modification of Mg, the strength of the weld joints became not the lowest part of the joint, instead, the HAZ showed the lowest microhardness and strength in as welded condition, as seen in Figure 3.4(b) and Figure 3.5(a).

After the PWHT, the tensile strength of the standard samples increased to the same level as BM, as seen in Figure 3.5(a). The heat-treated joints show interesting strength since the fracture using the standard samples occurs away from the FZs but in BM of all joints. The applied PWHT recovered all the microhardness and the strength in the HAZ zone, resulting in a microhardness profile coinciding with the BM level, and hence, its strength of all joints was similar to the BM [2]. It is apparent that using the standard samples, the difference of joint strengths for three different fillers cannot be distinguishable.

### 3.3.2.2.2 The tensile strength of the notched samples

Figure 3.5 (b) displays the tensile properties of the notched samples in the as welded and PWHT conditions. Applying the double edge notch, the fracture transferred from HAZ to the FZ in as welded condition. The UTS of the joints increased to 220 MPa in ER4043, 238 MPa in FMg0.6 and further to 250 MPa in FMg1.4 joints, respectively. By applying the PWHT, the fracture from BM transferred to the FZ. The UTS were further raised, which were 340, 366, and 384 MPa in ER4043, FMg0.6 and FMg1.4 joints, respectively. The black and blue dotted lined in Figure 3.5(b) show the level of the UTS and the YS of the BM for the comparison for the strength of the welded joints. The joint of FMg1.4 exhibited the highest strength among all the joints, while the ER4043 joint had the lowest strength but was slightly higher than that of the BM. It can be seen that, in both as-weld and PWHT conditions, the higher was the Mg content of the filler wires, the greater was the strength of the joints.

The strength of the as welded joints was found to be higher than that of the HAZ as shown in Figure 3.4(a). This is because some Mg from the BM was diffused to the FZ of the joints, enhancing the solid solution strength and making it harder as compared to the HAZ. By using the notched samples (Figure 3.2(b)), the effect the Mg on the strength of the FZ can be better characterized. The joint strength was dramatically improved with increasing the Mg content in the fillers. In the PWHT condition, all FZs displayed higher strengths compared to the strength of the BM, as shown in Figure 3.5(b). The improved strength in the FZs is directly related to the precipitation of  $\beta''$  in the aluminum matrix [2, 32]. The bright-field TEM images of Figure 3.6 show the typical precipitate microstructures of the BM and the ER4043, FMg0.6 and FMg1.4 welded samples, which were dominated by

nanoscale coherent  $\beta''$  MgSi precipitates. The FZ of the reference filler (Figure 3.6(a)) showed a higher number density and volume fraction of  $\beta''$  than the BM (Figure 3.6(b)), attributing to a higher Si in the reference filler to promote the precipitation of  $\beta''$  [33], although the BM possessed a higher Mg content. With increasing Mg in the novel filler wires, the  $\beta''$  became denser and finer relative to the reference filler (Figure 3.6(c-d)) and their number density and volume fraction of  $\beta''$  increased (Figure 3.6(e)).

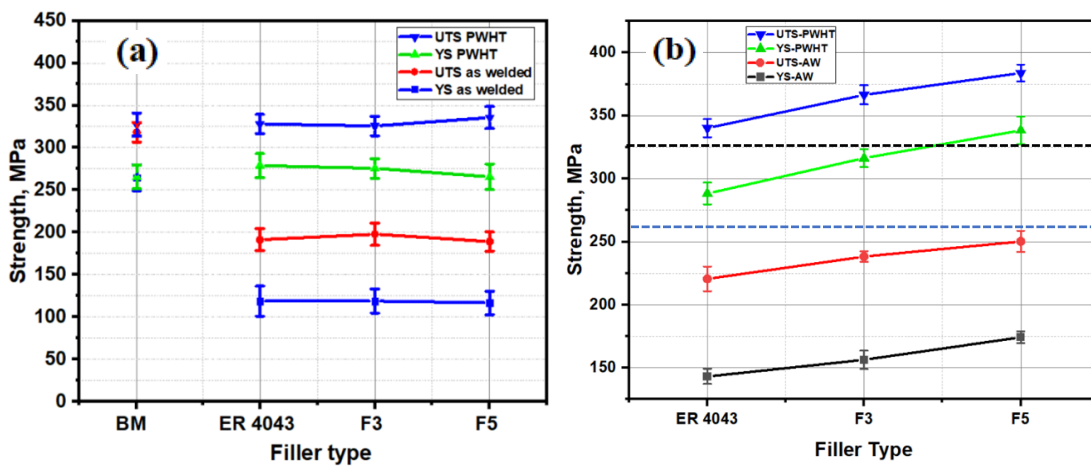


Figure 3.5. (a) tensile strengths of the standard samples and (b) tensile strengths of the notched samples in as welded (AW) and PWHT conditions. The blue and black dotted lines in (b) representing the YS and UTS of BM, respectively.

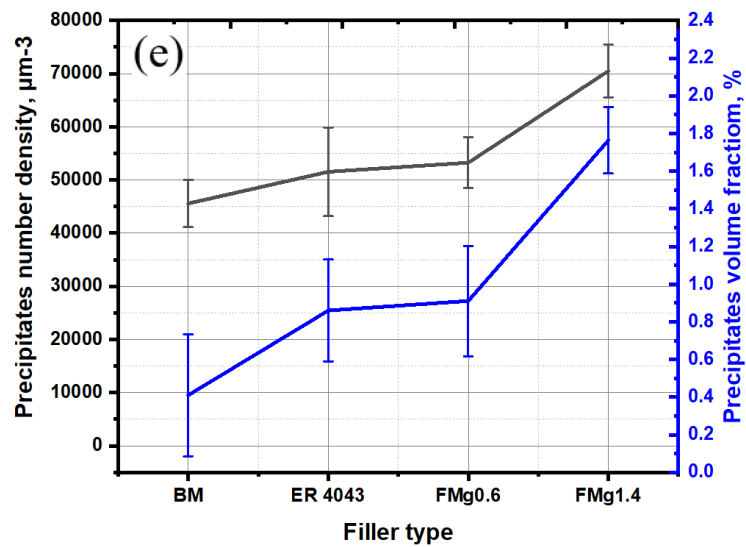
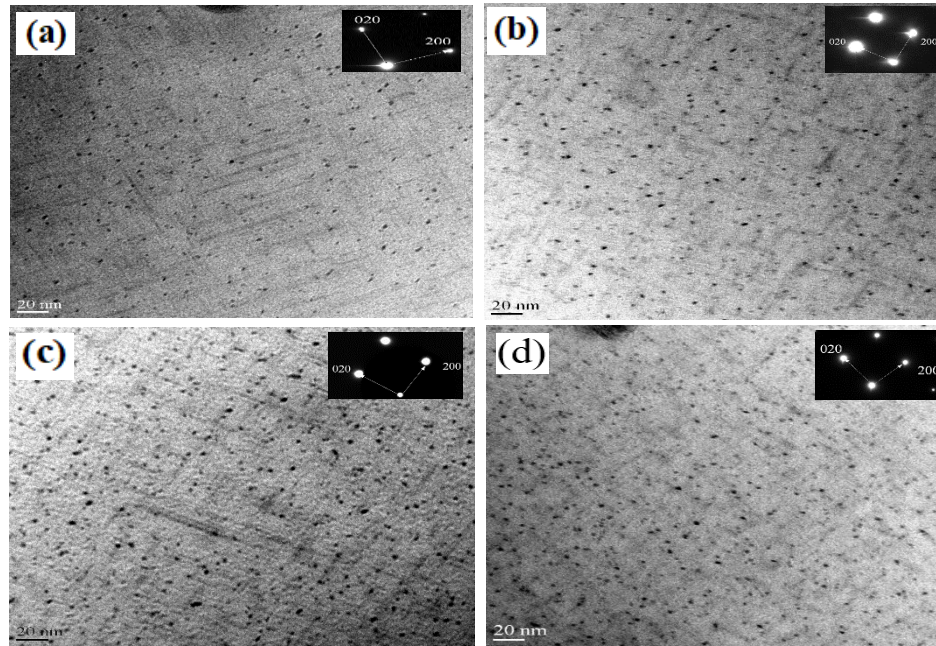


Figure 3.6. Bright-field TEM images of  $\beta''$  precipitates in the FZs of (a) BM, (b) ER4043, (c) FMg0.6 and (d) FMg1.4 joints, (e) Quantitative results of  $\beta''$  precipitates.

### 3.3.3 Fatigue properties

#### 3.3.3.1 S–N curves of welded samples

The S–N curve of the joints in as weld and PWHT conditions are displayed in Figure 3.7.

It is convenient to use the stress associated with specific fatigue life, such as  $10^6$  and  $10^7$

cycles on the S-N curve to express fatigue strength [33]. In this study, the fatigue strength for the different joints was taken at the fatigue life of  $10^6$  cycle because there was no plateau in the S-N curves of aluminum alloys. The fatigue life of the joints increases with decreasing applied stress. The S-N curves can generally be expressed by Basquin's equation [34]:

$$\sigma_{max} = AN_f^b$$

where  $\sigma_{max}$  is the maximum applied stress,  $A$  is the fatigue strength coefficient,  $b$  is the fatigue strength exponent, and  $N_f$  is the number of cycles to failure.

The S-N curve of the BM was also included for comparison purpose. As can be seen in Figure 3.7, the BM at all the applied stresses displayed the highest fatigue strength and life compared to the welded samples, since AA6061 rolled sheets had almost no defects relative to the welded joints. The fatigue strength and life increased with increasing Mg content in the filler wires (Figure 3.7(a)). The joints welded ER4043 displayed the lowest fatigue strength and life due to a low Mg content in ER4043. For instance, the fatigue strength in as weld samples increased from 115 MPa in ER4043 to 136 MPa in FMg0.6 and further to 158 MPa in FMg1.4 joints. The fatigue strength and life of the joints were further enhanced by applying the PWHT (Figure 3.7(b)). The fatigue lives of all the joints were closer to the fatigue life of BM compared to those in as welded condition. Meanwhile, the fatigue strength was improved from 150 MPa in ER4043 to 172 MPa in FMg0.6 and further to 194 MPa in FMg1.4 joints. The high Mg level in the filler wire improved the fatigue strength of the FMg1.4 joint by 37 % and 30 % in the as welded and PWHT conditions, respectively, relative to the ER4043 joint.

The trends of the relation of the maximum stress with fatigue life are also reflected in the fitting parameters of the S-N curves. The BM exhibited its high fatigue strength, as it has the highest fatigue strength coefficient ( $A$  value= 769.56). In the as welded condition, the ER4043 has the lowest  $A$  value (535.73). The welded joints of FMg0.6 and FMg1.4 have almost similar  $A$  values (between 604 – 608), which are considerably higher than that of ER4043 (Figure 3.7(a)). Similar to the as welded condition, the novel filler wires exhibited higher  $A$  values in the PWHT condition relative to the reference filler (Figure 3.7(b)). As shown by those regressed curves in Figure 3.7, at any given applied stress, the fatigue lives of the joints of novel filler wires are significantly higher than the joint of the reference filler; among all the joints, the joint of FMg1.4 filler exhibited the best fatigue life. These results depict that increasing the Mg content in the filler wires results in a significant improvement in the fatigue strength and life of the weld joints in both as welded and PWHT conditions .

The fatigue strengths at  $10^6$  cycles vs the UTS of the notched samples for all three joints are plotted in Figure 3.7(c). The fatigue strength of the joints is directly related to the UTS; the higher the UTS value, the greater the fatigue strength. This can be attributed to the increased solution strengthening in as welded samples and the enhanced precipitation strengthening in the PWHT samples, as the Mg content increased in the filler wires [35].

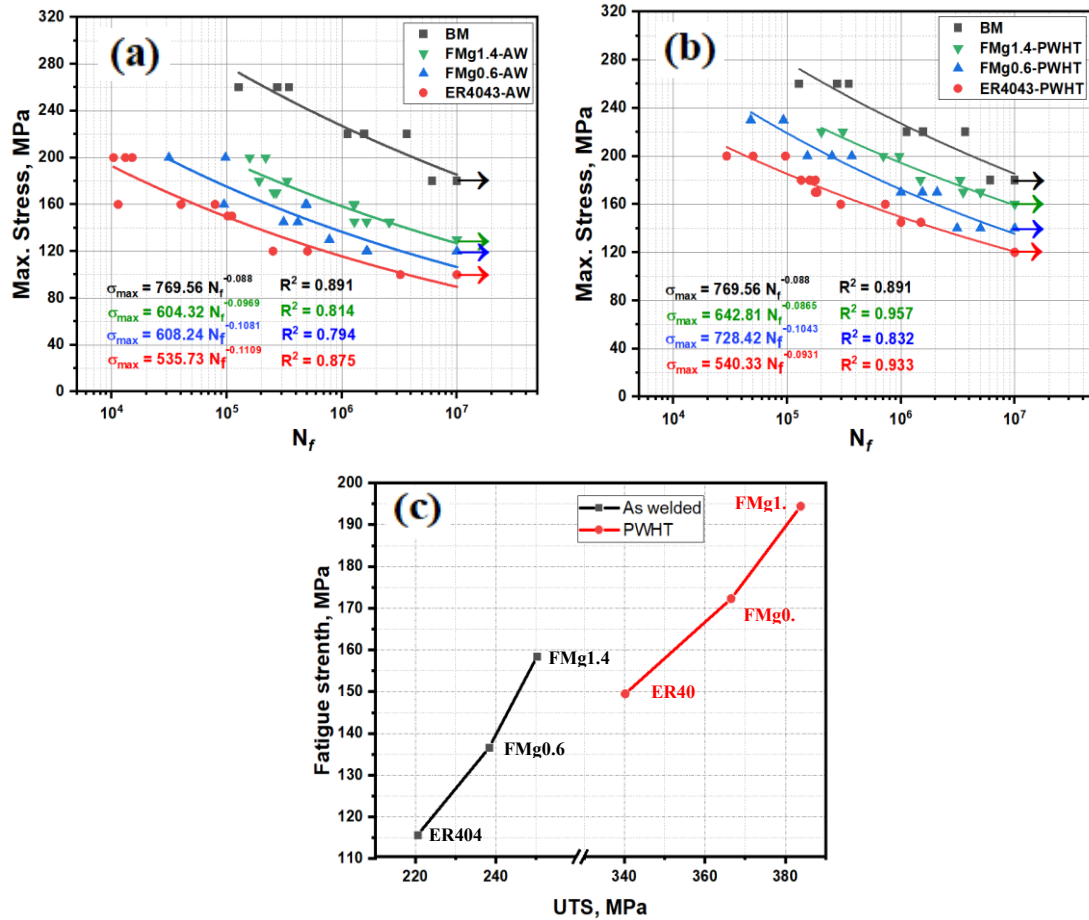


Figure 3.7. (a) S-N curves in as welded and (b) in PWHT conditions, (c) the fatigue strength as a function of the UTS in both as welded and PWHT conditions.

### 3.3.3.2 Effect of porosity on fatigue life

Several studies reported [36, 37] that the fatigue cracks in weld joints were mostly originated from porosity. In the present study, the fracture in fatigued samples mostly occurred in the FZs since the porosity formation is a common phenomenon during fusion welding, and the porosity is the largest defects in the welded joints in term of the size. To better understand the impact of porosity on the fatigue life, the samples were selected randomly from the welded plates covering the whole porosity range. Measuring the pores size was performed

according to the method used by Wang et al. [18], in which the squar root of the total projection area ( $\sqrt{A}$ ) of the pores in the fatigue fractured sample was measured, as shown in Figure 3.8. The pore size was plotted against the number of cycle at the maximum applied stress of 170 MPa in as weld condition (Figure 3.9). The general tendency is that the larger the pore size in the FZ, the lower the fatigue life in all the joints, indicating the severe deleterious effect of porosity. Moreover, for the small pore sizes ( $\sqrt{A} < 375 \mu\text{m}$ ), the joints with higher Mg content presented longer fatigue life compared with the joint of the reference filler, especially for FMg1.4 filler. However, for the large pore size ( $\sqrt{A} > 375 \mu\text{m}$ ), the fatigue lives of all joints were already in the low level and their values were in similar range, indicating that the porosity became a major influencing factor instead of the mechanical properties of the joints. This implies that the crack can directly start from the large pores without the initiation period [19].

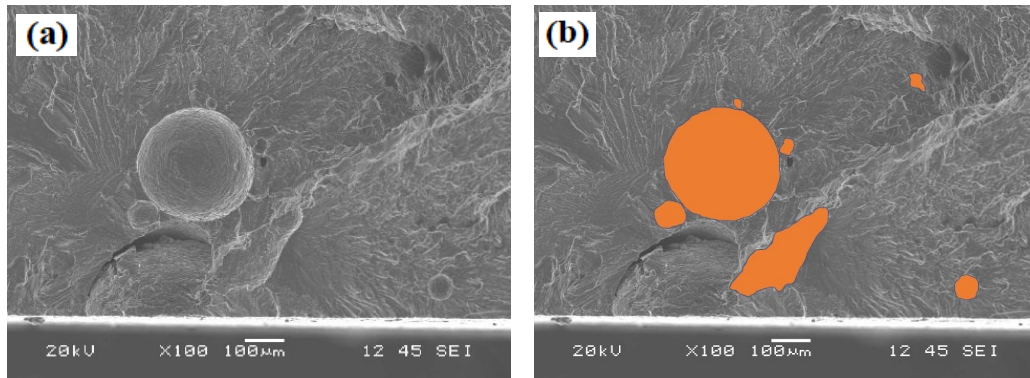


Figure 3.8. (a) SEM image of the fatigue fracture surface showing an example of pores and (b) the projection area of the pores.

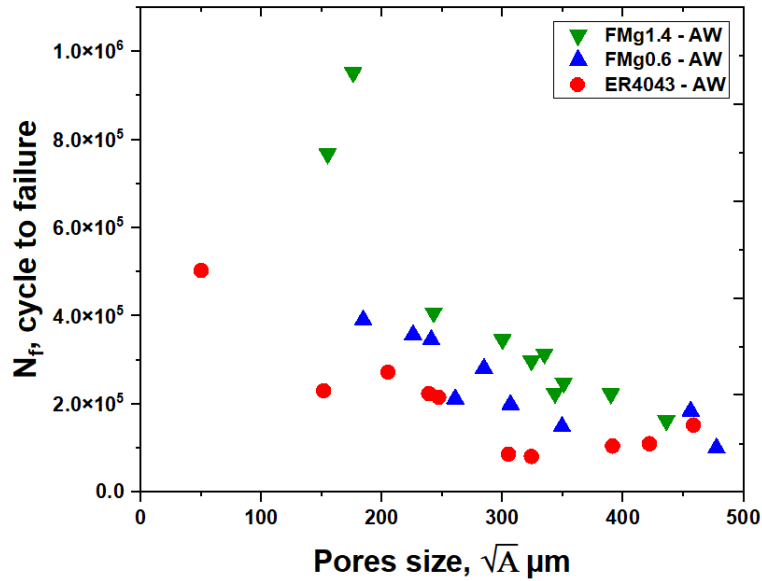


Figure 3.9. Fatigue life as a function of pores size at maximum applied stress of 170 MPa in the as welded condition.

### 3.3.3.3 Fracture analysis of weld joints

The fatigue fracture surfaces of the ER4043 and FMg1.4 joints in the as-weld condition are shown in Figure 3.10. The fracture surfaces show the three different zones, including the crack initiation, crack propagation, and the final failure zones [38]. It appears that the cracks are predominantly initiated from the pores close to the sample surface. According to Liu et al.[39], the crack initiated at the boundary between the pore and the surrounding material due to the stress concentration at the boundaries. As the crack adjacent to the pore grew, it would move both forward and backward inside the pore. Eventually, two cracks would converge, resulting in a crack that spans the entire pore (as illustrated in Figure 3.10(b)). Then the microcrack continued to extend to the final failure. As shown in Figure 3.10 (c and f), the fracture surfaces in the final failure zone were very shallow with presence of only several dimples and without slip bands, which implies that no plastic deformation occurred during cyclic loading in as welded condition. The joint of ER4043 in the crack propagation zone

displayed more cleavage facets compared to the joints of FMg1.4 (Figure 3.10(b) vs. Figure 3.10(e)). This result indicated that low-energy fracture occurred in the ER4043 joint, and hence a shorter lifetime was spent in the propagation zone compared to that the FMg1.4 joint.

Figure 3.11 displays the fatigue fracture surfaces of ER4043 and FMg1.4 joints in the PWHT condition. Similar to the as weld joints, the cracks were principally initiated from the pores close to the sample surface. As shown in Figure 3.11(b and f), slip bands can be observed in the PWHT samples. Compared to the as-weld samples, the crack propagation through the localized plastic deformation governed by the slip bands required higher numbers of cyclic loading, and hence extended the fatigue life [14-16]. Therefore, unlike the as-weld condition, the fatigue life in the PWHT samples is derived by a combined influence of the porosity, crystallographic mechanism and plasticity of the material [40]. As shown in Figure 3.11(c), the final zone experienced a ductile fracture in all the joints. The fracture dimples were larger and deeper in Figure 3.11(c) than those in Figure 3.10(c), showing improved plasticity in the PWHT samples. The area fraction of the propagation zone in FMg1.4 joint was larger relative to the joint of ER4043 ( $7.4 \text{ mm}^2$  vs  $5.6 \text{ mm}^2$ ), due to its superior tensile strength and the positive effect of the coherent  $\beta''$  precipitates. According to Wang et al. [18], the fatigue of Al-Si alloys failed mostly due to defects like porosity and oxide films, and the total fatigue life was primarily made up of crack propagation life, and the number of cycles required to start the fatigue crack from a defect can be ignored. Therefore, the fatigue life of weld joints was mostly controlled by the crack propagation rate for the three fillers studied. This is determined by the yield strength since a higher yield strength decreases the propagation rate. Higher yield strengths can also result in fewer and

smaller local plastic deformation zones in the material. The slip bands in FMg1.4 joint started near to the pore initiator, which means longer time was taken to form the bands to start the propagation zone. By contrast, the slip bands in ER4043 joint started at boundary of the pore and the matrix and have no time to form wide bands and hence the crack initiated faster than that in FMg1.4 joint.

The crack propagation rate can be estimated by the width of the striation in the fracture surface (i.e., the displacement of the crack tip with each cycle). The larger the striation width, the greater the crack propagation rate, and the lower the fatigue strength [2, 41, 42]. The method used to calculate the width of the striation is depicted in Figure 3.12(a). Figure 3.12(b–e) reveal the striation evolution during crack propagation for two different filler wires, and Figure 3.12(f) displays the striation width as a function of the distance from the initiation zone. By moving away from the crack initiation zone, the striation width increased. However, at a given distance from the initiation zone, the striation width decreased with increasing the Mg content of the joints. For instance, at 1.5 mm from the initiation zone, the striation width in FMg1.4 is smaller compared to that in ER4043 (0.76  $\mu\text{m}$  vs 1.11  $\mu\text{m}$ ). This implies that the crack propagation rate in FMg1.4 joint is slower than that in the 4043 joint, which is consistent with the results of the fatigue life in Figure 3.7.

#### **3.3.3.4 Effect of Mg on fatigue properties**

In the as welded condition, the central role of Mg in the aluminum matrix is the solid solution strengthening, improving both tensile strength and fatigue strength. Takahashi et al. [9] studied the excess Mg in a stoichiometric  $\text{Mg}_2\text{Si}$  composition AA6061-T6 alloy, and found that the Mg in the solid solution increased the alloy work hardening, which produced cyclic slip resistance at the initial crack tip and retarded the crack growth. Moreover, the

solute Mg could shift the crack motion to a non-localized mode due to generation a large number of active slip systems leading to a longer crack path and longer fatigue life before the final failure [8, 13]. Due to higher Mg content in the novel filler wires, the FZ of FMg0.6 and FMg1.4 joints contained much more Mg solutes relative to the reference filler wire [21]. The results in Figure 3.7(a) also confirmed that FMg0.6 and FMg1.4 joints had higher fatigue strength and longer fatigue life compared to ER4043 joint.

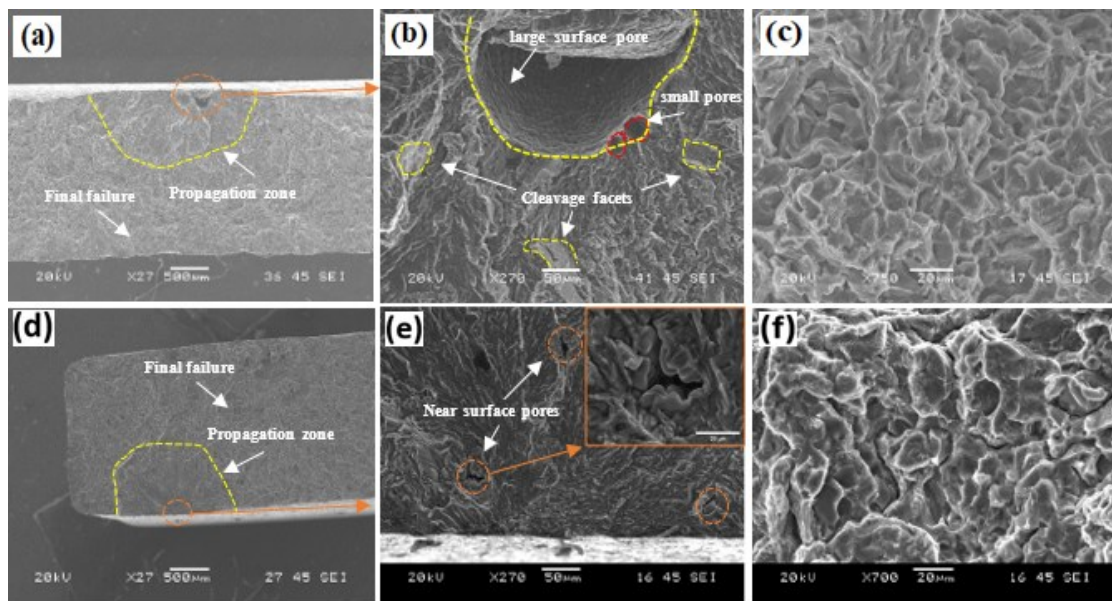


Figure 3.10. SEM images of the fatigue fracture surface in as welded condition at  $\sigma_{max}$  of 200 MPa, (a) macroscopic view, (b) the initiation and propagation zones and (c) the final zone for ER4043 joint; (d) macroscopic view, (e) the initiation and propagation zones and (f) the final zone for FMg1.4 joint.

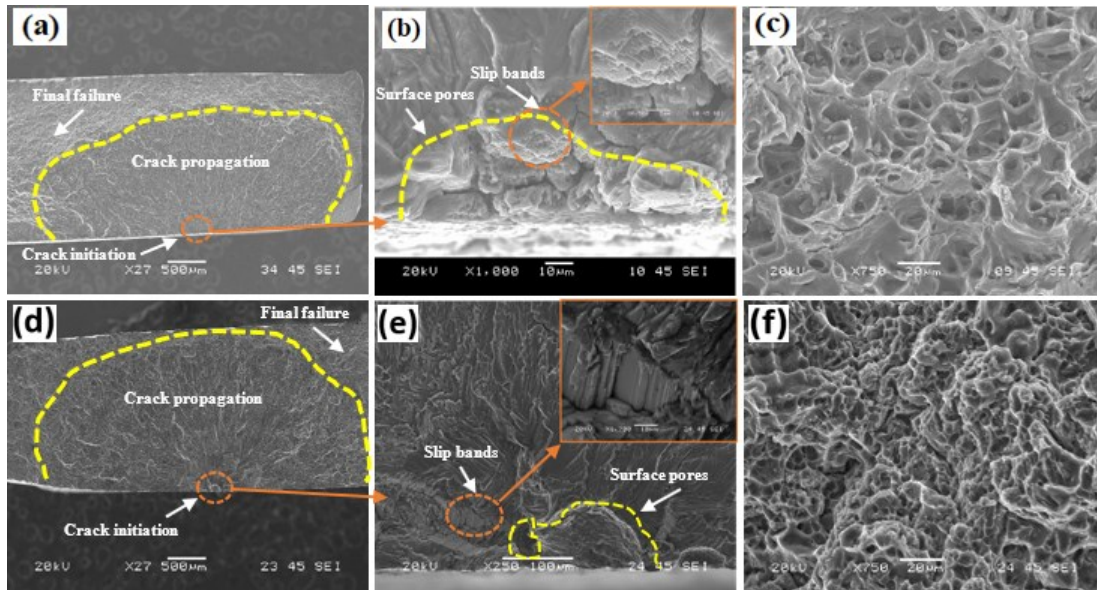


Figure 3.11. SEM images of the fatigue fracture surface in PWHT condition at  $\sigma_{max}$  of 200 MPa, (a) macroscopic view, (b) the initiation and slip bands and (c) the final zone for ER4043 joint; (d) macroscopic view, (e) the initiation and slip bands and (f) the final zone for FMg1.4 joint.

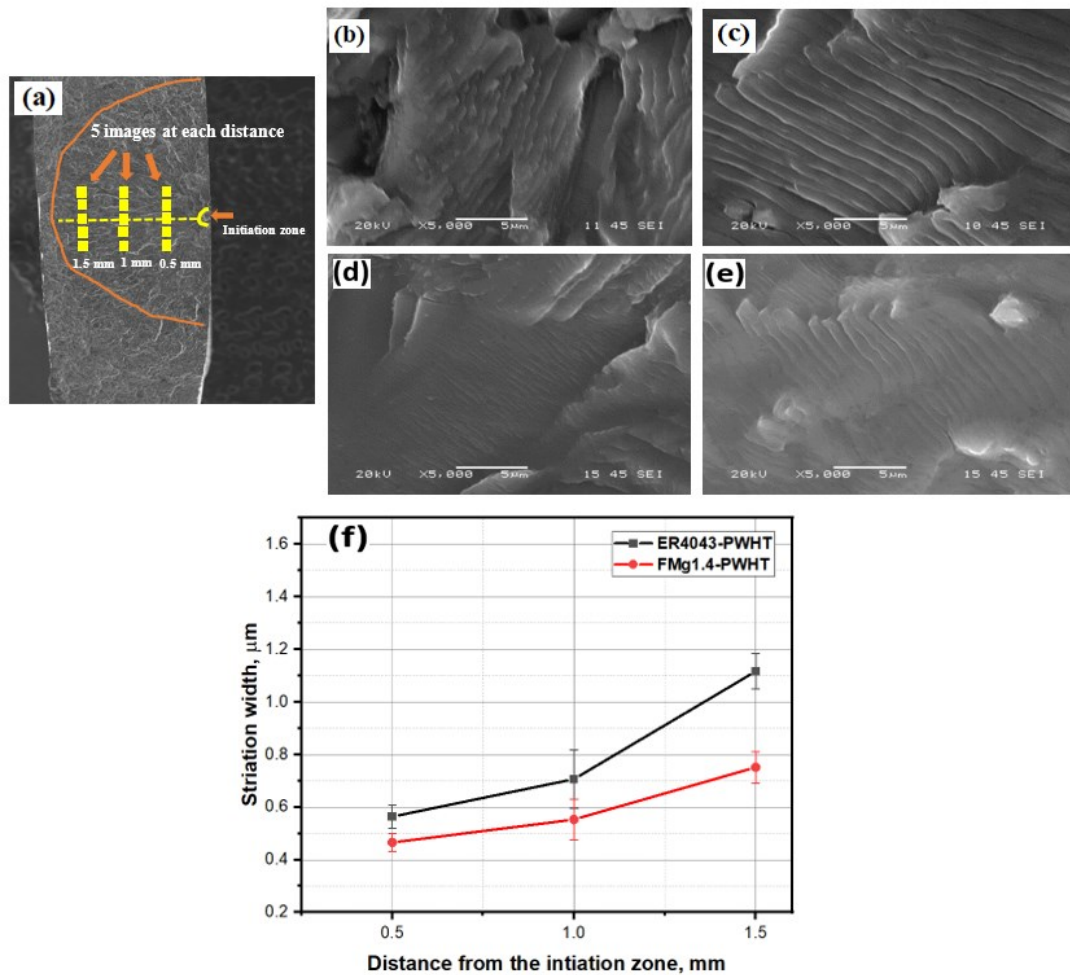


Figure 3.12. Fatigue striations during crack propagation in PWHT condition at  $\sigma_{max}$  of 200 MPa, (a) evaluation of fatigue striation, and (b) and (c) SEM images showing the striations at 0.5 mm and 1.5 mm from the crack initiation zone for ER4043 joint; (d) and (e) SEM images showing the striations at 0.5 mm and 1.5 mm from the crack initiation zone for FMg1.4 joint; (f) striation width at different distances from the initiation zone.

With applying the PWHT, the  $\beta''$  precipitated in the aluminum matrix of FZ zones as the main strengthening phase (Figure 3.6) and significantly increased the tensile strength, as shown in Figure 3.7(b). It is reported [11, 39] that during cyclic loading the dislocations could share the coherent precipitates and lead to cyclic softening, which reduced the dislocation piling up at the grain boundaries and hence lowered the stress concentration to

avoid the formation of microcracks [2]. The higher number density of coherent  $\beta''$  precipitates, the lower microcracks growth. The high number density of  $\beta''$  precipitates in the FZ via increasing the Mg content in the novel filler wires resulted in improving the fatigue strength and life in FMg0.6 and FMg1.4 joints, as depicted in Figure 3.7(b). The fatigue strength and life were in the order of FMg1.4 > FMg0.6 > ER4043. Another secondary factor for improvement in the fatigue properties after heat treatment could be related to the transition of coarse plate-like Si in as weld condition to the fine spherical Si after PWHT, which is capable of impeding crack initiation and propagation. Khisheh et al. [43] report that the heat treatment extended the high-cycle bending fatigue lifetime of A380 alloy by 26% and 85% at the highest and lowest stress levels, respectively. This was attributed to change the morphology of the eutectic silicon phase that strengthened the material.

### 3.4 Conclusions

1. Increasing Mg level in Al-Si-Mg 4xxx filler metals provided higher microhardness and tensile strength of weld joints compared to the reference ER4043 filler in both as welded and PWHT conditions. The higher Mg content in the filler wire, the higher mechanical strength of the weld bead.
2. The joints made by novel fillers with high Mg content (0.6-1.4 wt.%) displayed higher fatigue strengths and longer fatigue lives compared to the joint made by the reference filler in both as welded and PWHT conditions. The joint with the filler containing 1.4 wt.% Mg exhibited the highest fatigue strength and best fatigue life among all three joints studied.
3. The porosity in the fusion zone had a detrimental effect on fatigue life. For the small pore sizes, the joints of novel fillers with higher mechanical strength showed longer fatigue lives compared the joint of the reference filler. For large pore sizes, the porosity became a major influencing factor instead of the mechanical properties of the joints.

4. The porosity close to the sample surface were the major crack initiation sites during cycle loading. After applying the PWHT, the slip bands and fatigue striation in the welding zone can be clearly observed. The striation width in joint with the novel filler containing 1.4 wt.% Mg was significantly smaller than that in the reference filler joint, indicating the low crack propagation rate for a longer fatigue life.
5. With increasing Mg content in 4xxx fillers, the improved mechanical strength and fatigue strength in weld joints were attributed to the enhanced solid solution strengthening of Mg in as welded condition and the increased precipitation strengthening of  $\beta''$  in PWHT condition.

### 3.5 References

1. Xiao, R.; Zhang, X. Problems and issues in laser beam welding of aluminum–lithium alloys. *J. Manuf. Processes*, **2014**, *16*, 166-175.
2. Pérez, J. S.; Ambriz, R. R.; López, F. F. C. Recovery of mechanical properties of a 6061-T6 aluminum weld by heat treatment after welding. *Metall. Mater. Trans. A*, **2016**, *47*, 3412-3422.
3. Chiarelli, M. L., Agostino Sacchi, Sacchi, M Fatigue resistance of MAG welded steel elements. *Int. J. Fatigue*, **1999**, *21*, 1099-1110.
4. Anderson, T. A New Development in Aluminum Welding Wire: Alloy 4943. *Weld. J.*, **2013**, *92*, 32-37.
5. Bethea, J. F. Gas Tungsten Arc Welding of Aluminum Alloys with Nanocomposite 4943 Filler Material. master of engineering, University of California, Los Angeles, 2019.
6. Niu, P. L., Wenya Yang, Chenggang Chen, Yuhua Chen, Daolun Yang, Chenggang Chen, Yuhua Chen, Daolun Chen, Yuhua Chen, Daolun Low cycle fatigue properties of friction stir welded dissimilar 2024-to-7075 aluminum alloy joints. *Mater. Sci. Eng., A*, **2022**, *832*, 142423.
7. Fajri, A. P., Aditya Rio Muhayat, Nurul Smaradhana, Dharu Feby Bahatmaka, Aldias. Fatigue analysis of engineering structures: State of development and achievement. *Procedia Struct. Integr.*, **2021**, *33*, 19-26.
8. Takahashi, Y.; Kuriki, R.; Kurihara, J.; Kozawa, T.; Shikama, T.; Noguchi, H. Distinct fatigue limit of a 6XXX series aluminum alloy in relation to crack tip strain-aging. *Mater. Sci. Eng., A*, **2020**, *785*, 139378.
9. Takahashi, Y.; Shikama, T.; Nakamichi, R.; Kawata, Y.; Kasagi, N.; Nishioka, H.; Kita, S.; Takuma, M.; Noguchi, H. Effect of additional magnesium on mechanical and high-cycle fatigue properties of 6061-T6 alloy. *Mater. Sci. Eng., A*, **2015**, *641*, 263-273.
10. Takahashi, Y.; Yoshitake, H.; Nakamichi, R.; Wada, T.; Takuma, M.; Shikama, T.; Noguchi, H. Fatigue limit investigation of 6061-T6 aluminum alloy in giga-cycle regime. *Mater. Sci. Eng., A*, **2014**, *614*, 243-249.
11. Shan, Z.; Liu, S.; Ye, L.; Li, Y.; He, C.; Chen, J.; Tang, J.; Deng, Y.; Zhang, X. Mechanism of Precipitate Microstructure Affecting Fatigue Behavior of 7020 Aluminum Alloy. *Materials*, **2020**, *13*, 3248.

12. Jin, Y.; Jiahao, S.; Chenkai, G.; Yixuan, Z.; Hongbing, L.; Oliveira, J. P.; Caiwang, T.; Zhishui, Y. Effect of heat input on interfacial microstructure, tensile and bending properties of dissimilar Al/steel lap joints by laser Welding-brazing. *Opt. Laser Technol.*, **2021**, *142*, 107218.
13. Anis, S. F.; Koyama, M.; Hamada, S.; Noguchi, H. Mode I fatigue crack growth induced by strain-aging in precipitation-hardened aluminum alloys. *Theor. Appl. Fract. Mech.*, **2019**, *104*, 102340.
14. Jiang, X.-S.; He, G.-Q.; Liu, B.; Fan, S.-J.; Zhu, M.-H. Microstructure-based analysis of fatigue behaviour of Al-Si-Mg alloy. *Trans. Nonferrous Met. Soc. China*, **2011**, *21*, 443-448.
15. Li, P.; Li, H.; Liang, X.; Huang, L.; Zhang, K.; Chen, Z. Enhanced low-cycle fatigue and crack propagation resistance of an Al-Cu-Mg-Si forging alloy by non-isothermal aging. *Mater. Sci. Eng., A*, **2018**, *732*, 341-349.
16. Wang, B.; Xue, S.; Ma, C.; Wang, J.; Lin, Z. Effects of porosity, heat input and post-weld heat treatment on the microstructure and mechanical properties of TIG welded joints of AA6082-T6. *Metals*, **2017**, *7*, 463.
17. Morton, T. M. Defects in 2021 aluminum alloy welds. *Weld. J.*, **1971**, *7*, 304-312.
18. Wang, Q.; Apelian, D.; Lados, D. Fatigue behavior of A356-T6 aluminum cast alloys. Part I. Effect of casting defects. *J. Light Met.*, **2001**, *1*, 73-84.
19. Gao, Y. X. Y., J. Z. Lee, PD. Lee, P. D. Lindley, T. C. The effect of porosity on the fatigue life of cast aluminium-silicon alloys. *Fatigue Fract. Eng. Mater. Struct.*, **2004**, *27*, 559-570.
20. Caton, M. J. Predicting fatigue properties of cast aluminum by characterizing small-crack propagation behavior. University of Michigan, 2001.
21. Linder, J.; Arvidsson, A.; Kron, J. The influence of porosity on the fatigue strength of high-pressure die cast aluminium. *Fatigue Fract. Eng. Mater. Struct.*, **2006**, *29*, 357-363.
22. Ahmed, M.; Javidani, M.; Mirakhorli, F.; Maltais, A.; Chen, X. G. Developing High-Strength Al-Si-Mg Filler Metals for Aluminum Fusion Welding. *J. Mater. Eng. Perform.*, **2023**, *32*, 2218-2227.
23. Fan, C.; Yang, S.; Zhu, M.; Bai, Y. Microstructure and Fatigue Properties of 6061 Aluminum Alloy Laser-MIG Hybrid Welding Joint. *Adv. Mater. Sci. Eng.*, **2021**, *2021*.
24. Salvati, E. E., Joris Kageyama, Koji Korsunsky, Alexander M Kageyama, Koji Korsunsky, Alexander M Transverse fatigue behaviour and residual stress analyses

- of double sided FSW aluminium alloy joints. *Fatigue Fract. Eng. Mater. Struct.*, **2019**, *42*, 1980-1990.
25. Tagirov, D. L., Elena Kaibyshev, Rustam Kaibyshev, Rustam Effect of Liquid Hot Isostatic Pressing on Structure and Mechanical Properties of a Sand-Cast A356. 02 Alloy. *Metall. Mater. Trans. A*, **2013**, *44*, 2369-2381.
  26. Kim, D.-Y.; Hwang, I.; Jeong, G.; Kang, M.; Kim, D.; Seo, J.; Kim, Y.-M. Effect of Porosity on the Fatigue Behavior of Gas Metal Arc Welding Lap Fillet Joint in GA 590 MPa Steel Sheets. *Metals*, **2018**, *8*, 241.
  27. Lashkari, O. Y., Lu Cockcroft, Steve Maijer, Daan X-ray microtomographic characterization of porosity in aluminum alloy A356. *Metall. Mater. Trans. A*, **2009**, *40*, 991-999.
  28. Wang, L.; Liu, Y.; Yang, C.; Gaos, M. Study of porosity suppression in oscillating laser-MIG hybrid welding of AA6082 aluminum alloy. *J. Mater. Process. Technol.*, **2021**, *292*, 117053.
  29. Vimalraj, C. K., Paul Experimental Review on Friction Stir Welding of Aluminium Alloys with Nanoparticles. *Metals*, **2021**, *11*, 390.
  30. Murali, N. S., Maximilian Yao, Gongcheng Pan, Shuaihang De Rosa, Igor Li, Xiaochun Gas-Tungsten Arc welding of dissimilar aluminum alloys with Nano-Treated filler. *J. Manuf. Sci. Eng.*, **2021**, *143*, 081001.
  31. Pedersen, L.; Arnberg, L. The effect of solution heat treatment and quenching rates on mechanical properties and microstructures in AlSiMg foundry alloys. *Metall. Mater. Trans. A*, **2001**, *32*, 525-532.
  32. Yıldırım, M.; Özyürek, D. The effects of Mg amount on the microstructure and mechanical properties of Al–Si–Mg alloys. *Mater. Des.*, **2013**, *51*, 767-774.
  33. Malarvizhi, S. R., K Viswanathan Viswanathan. Fatigue behaviour of post weld heat treated electron beam welded AA2219 aluminium alloy joints. *Mater. Des.*, **2008**, *29*, 1562-1567.
  34. Ambriz, R. R.; Mesmacque, G.; Ruiz, A.; Amrouche, A. Effect of the welding profile generated by the modified indirect electric arc technique on the fatigue behavior of 6061-T6 aluminum alloy. *Mater. Sci. Eng., A*, **2010**, *527*, 2057-2064.
  35. Yarema, S. Y. Formation of the science of fatigue of metals. Part 2. 1870-1940. *Mater. Sci.*, **2006**, *42*, 814.
  36. He, C. H., Chongxiang Liu, Yongjie Wang, Qingyuan Liu, Yongjie Wang, Qingyuan Fatigue damage evaluation of low-alloy steel welded joints in fusion zone and heat

- affected zone based on frequency response changes in gigacycle fatigue. *Int. J. Fatigue*, **2014**, *61*, 297-303.
37. Zhao, X. D., Wang Deng, Caiyan Liu, Yu Zongxian, Song The fatigue behaviors of butt welds ground flush in the super-long life regime. *Int. J. Fatigue*, **2012**, *36*, 1-8.
  38. Yan, S. N., Yuan Zhu, Zongtao Zhu, Zongtao Chen, Hui Gou, Guoqing Yu, Jinpeng Wang, Guiguo Chen, Hui Gou, Guoqing Yu, Jinpeng Wang, Guiguo Characteristics of microstructure and fatigue resistance of hybrid fiber laser-MIG welded Al–Mg alloy joints. *Appl. Surf. Sci.*, **2014**, *298*, 12-18.
  39. Liu, H.; Yang, S.; Xie, C.; Zhang, Q.; Cao, Y. Microstructure characterization and mechanism of fatigue crack initiation near pores for 6005A CMT welded joint. *Mater. Sci. Eng., A*, **2017**, *707*, 22-29.
  40. Gerbe, S. K., Ulrich Michels, Wilhelm. Influence of secondary dendrite arm spacing (SDAS) on the fatigue properties of different conventional automotive aluminum cast alloys. *Frat. ed Integrita Strutt.*, **2019**, *13*, 105-115.
  41. Davidson, D.; Lankford, J. Fatigue crack growth in metals and alloys: mechanisms and micromechanics. *Int. Mater. Rev.*, **1992**, *37*, 45-76.
  42. Lancaster, R.; Jeffs, S.; Illsley, H.; Argyrakis, C.; Hurst, R.; Baxter, G. Development of a novel methodology to study fatigue properties using the small punch test. *Mater. Sci. Eng., A*, **2019**, *748*, 21-29.
  43. Khisheh, S.; Khalili, K.; Azadi, M.; Hendouabadi, V. Z. Influences of roughness and heat treatment on high-cycle bending fatigue properties of A380 aluminum alloy under stress-controlled cyclic loading. *Mater. Chem. Phys.*, **2021**, *264*, 124475.

## 4. Chapter 4: Microstructure and mechanical properties of high-strength AA6011 aluminum alloy welding with novel 4xxx filler metals

(Published in the Journal of Materials)

### Abstract

Welding high strength 6xxx aluminum alloys using a commercial ER4043 filler often results in inferior joint strength. This study investigated the effects of newly developed Al-Si-Mg filler metals with varying Mg (0.6–1.4 wt.%) and Mn (0.25–0.5 wt.%) contents on microstructure evolution and mechanical performance of high-strength AA6011-T6 plates using gas metal arc welding. Two commercial fillers, ER4043 and ER4943, were used as references for comparison. The results revealed that increasing the Mg and Mn contents in the novel fillers resulted in sufficiently high alloying elements in the fusion zone (FZ), leading to higher microhardness. Under as-welded conditions, the weakest region of the joint was the heat-affected zone (HAZ). The joint strength was almost independent of the filler type and was controlled by the HAZ strength. The higher Mg contents in the novel fillers promoted the precipitation of a large volume fraction of fine  $\beta''$ -MgSi in the FZ during post-weld heat treatment (PWHT), resulting in superior strength and higher welding efficiency relative to the reference fillers. The optimal Mg content of the novel fillers was 0.6 wt.%. Increasing the Mn content of the filler metal had an insignificant effect. The FMg0.6 filler with 0.6% Mg achieved the best combination of strength and elongation, as well as the highest welding efficiency after PWHT, among all fillers studied. However, the newly developed fillers adversely affected the impact toughness of the joints.

**Keywords:** High-strength aluminum alloy welding; AA6011 alloy; 4xxx filler metals; Mechanical properties; Impact toughness.

## 4.1 Introduction

Al-Mg-Si 6xxx alloys are widely used in the aerospace and automotive industries owing to their high strength-to-weight ratio, good corrosion resistance, and weldability. However, the welding of 6xxx alloy parts using commercial Al-Si 4xxx filler metals often results in low welding strength, which is not acceptable for high-strength 6xxx alloy welding in many applications. The use of Al-Si 4xxx filler metals can be traced back to the 1940s. They have been widely used for the general-purpose welding of 6xxx alloys owing to their low cost, high fluidity in the weld zone, and good resistance to weld cracks [1]. However, low welding strength is a persistent problem for high strength 6xxx alloy joints. Recent research has explored the development of new filler metals with improved mechanical properties, such as the use of nanoscale reinforcement particles and advanced welding techniques such as friction stir welding. However, the welding strength generally remains lower than the strength of the base metal (BM) [1, 2].

The fusion welding process involves melting a part of the BM and filler metal together to form a weld bead or fusion zone (FZ). The composition of the FZ depends mainly on the composition of the BM and filler metal as well as the added ratio of these constituents, which is called the dilution ratio [3, 4]. Furthermore, in the case of thick and multipass weldments, the dilution ratio calculation is complex because some parts of the previous pass are shared in the formation of the next pass [5]. The dilution is highest for single-pass welds on thin sheets with square joints, while it is lowest for fillet welds with regular edge preparation and in the backup passes with thick BMs. Changes in welding parameters and joint geometry can affect fusion zone dilution and, hence, change the chemical composition of the weld zone [6]. Mousavi et al. [7] calculated the dilution ratio for different joint geometries and reported

that a beveled joint (single V groove) produced minimal BM dilution (40–60%), whereas butt joints resulted in high dilution (60–80%). Commercial ER4043 (Al-5Si) and ER4943 (Al-5Si-0.4Mg) wires are common filler metals used in Al welding. Owing to the high Si content of these two fillers, the chemical composition of the FZ shifts towards an alloy regime that is less prone to hot cracking. However, because of the absence or insufficiency of Mg for  $Mg_2Si$  precipitation strengthening in weldments, the mechanical properties of high strength 6xxx joints are often unsatisfactory. Therefore, the chemical composition of the FZ is the main factor affecting the metallurgical and mechanical properties of the weld and its susceptibility to cracking [8-10].

In addition to the mechanical properties, the Charpy impact test offers significant benefits, such as determining the ductile-to-brittle transition and the relative toughness between different materials [11]. However, limited data are available in the literature on the impact toughness of Al alloys. Investigations of the impact properties have mainly focused on eutectic Al-Si cast alloys in the automotive industry [12, 13]. Murali et al. [14] studied the effects of Mg and Fe impurities on the impact properties of hypoeutectic Al-Si-Mg cast alloys in the aircraft industry. They found that an increase in the Mg content from 0.32% to 0.65% caused a notable reduction of approximately 50% in the total absorption energy until fracture, which highlighted the possible embrittlement effect of Mg. The Fe intermetallics were investigated by Samuel et al. [15], who reported that a higher volume fraction of Fe intermetallics led to a reduction in impact toughness. Heat treatment was found to significantly enhance the impact energy of the as-cast 356 alloys, particularly when the iron content in the alloy was low [16]. Mosneaga et al. [17] found that the addition of Mn could enhance the impact toughness of the welded metal by 20–30%.

In our previous work [18], an AA6061-T6 thin sheet with a thickness of 2 mm was welded to the newly developed 4xxx fillers. The results showed that a high dilution ratio of approximately 56% produced an increase in the Mg content of the FZ, even if the Mg-free ER4043 filler was used. Consequently, the FZ became heat-treatable and exhibited a reasonably high tensile strength. However, when thick plates of high-strength AA6011 BM ( $YS > 400$  MPa) were welded using multiple passes, the dilution ratio from the BM was low, and only a small amount of Mg from the BM could be transferred to the FZ. Consequently, the joint strength decreased depending on the amount of Mg transferred. In this study, four novel filler metals were designed with Mg content of 0.6–1.4 wt.% and Mn content of 0.25–0.5 wt.%. High-strength AA6011-T6 plates with a thickness of 6 mm were welded to systematically investigate the effect of filler metals on the mechanical performance and microstructural evolution of the joints under as-weld and post-weld heat treatment (PWHT) conditions. ER4043 and ER4943, two reference fillers, were used for comparison with the newly developed fillers.

## **4.2 Experimental Procedure**

The BM of the AA6011 alloy was direct-chill-cast and extruded into plates with a cross-section of 75 mm  $\times$  6 mm, which were then cut into a plate with a length of 500 mm and heat-treated in the T6 temper. The plates were welded using the gas metal arc welding (GMAW) technique. The filler wires used in this study were composed of four newly developed filler metals and two reference filler metals (commercial ER4043 and ER4943). The chemical compositions of the BM and filler metals are listed in Table 4.1. The process for producing new filler wires was reported in our previous study [18]. A Fronius Transpulse Synergic 5000-CMT mounted on a Motoman UP50N robot was used for the welding. Before

welding, the plates were clamped in a butt-joint configuration with a single V-groove geometry, as shown in Figure 4.1. The welding parameters used in the two passes are listed in Table 4.2. A higher current for the first pass (163 A) was selected with the aim of achieving greater melt penetration owing to the groove geometry. The current of the second pass (110 A) necessitated reduced melt penetration and heat input [19]. Following the welding process, a part of the weld plates underwent PWHT, including a solution treatment at 550 °C for 1 h and water quenching, and natural aging for 24 h, followed by artificial aging at 180 °C for 8 h. The heat treatment was optimized to determine the mechanical properties of the BM during welding.

The dilution ratios of the weld zone were calculated using the following equation [5]:

$$D_n = [BM_n + \sum_j^{n-1} R_{nj} \cdot D_j] / A_n$$

where  $D_n$  is the dilution with BM in pass  $n$ ;  $n$  is the pass number;  $BM_n$  is the melted BM area by pass number  $n$ ;  $j$  is the number of previously deposited passes,  $R_{nj}$  is the melted area from the previous pass  $j$  in pass  $n$ ;  $D_j$  is the dilution with BM in the weld zone for bead  $j$ ;  $A_n$  is the total area of the BM in pass  $n$  under the as-deposited condition. All the areas are illustrated in Figure 4.2. The calculated dilution ratios in the first and second passes are  $43 \pm 0.02\%$  and  $21 \pm 0.06\%$ , respectively. The chemical composition in each pass in the weld zone was calculated, and the results are listed in Table 4.3.

Microstructural analyses were performed using optical microscopy (OM), scanning electron microscopy (SEM), and transmission electron microscopy (TEM). The microhardness (HV) profiles were measured using an NG-1000 CCD microhardness tester with a 50-gram load and 20-second dwell time. The HV measurements for each joint were

obtained at two specific locations: the first location was positioned 1 mm from the bottom (representing the first pass), and the second location was located 1 mm from the upper surface (representing the second pass). Tensile tests were performed using an Instron 8801 servo-hydraulic machine under as-welded (AW) and PWHT conditions, using a crosshead speed of 1 mm/min at room temperature with standard subsize samples, according to ASTM B557-15. Impact tests were conducted on the AW and PWHT samples to evaluate the impact toughness of the filler joints. Perpendicular to the weld bead, half-sized Charpy V-notch specimens with dimensions of 10 mm × 5 mm × 55 mm, notch root radius of 0.25 mm, notch depth of 2 mm, and notch flank angle of 45° were machined according to ASTM E23. The notch in the HAZ was machined 8 mm from the center of the FZ. Figure 4.3 shows the geometries of the impact samples. An instrumented Charpy impact testing machine with a capacity of 150 J, an impact speed of 5.2 m/s, and a pendulum drop angle of 150° was used.

Table 4.1. Chemical compositions of the base metal and filler metals (wt.%)

	Si	Mg	Mn	Fe	Cu	Ti
<b>BM (6011-T6)</b>	0.92	0.75	0.45	0.17	0.64	0.028
<b>ER 4043</b>	4.97	0.024	0.02	0.16	-	0.108
<b>ER 4943</b>	5.51	0.395	0.02	0.17	-	0.108
<b>FMg0.6</b>	6.23	0.6	0.23	0.14	0.011	0.103
<b>FMg1.4</b>	6.4	1.4	0.28	0.18	0.012	0.103
<b>Mg0.6Mn</b>	6.2	0.61	0.5	0.14	0.01	0.103
<b>Mg1.4Mn</b>	6.25	1.43	0.48	0.15	0.012	0.106

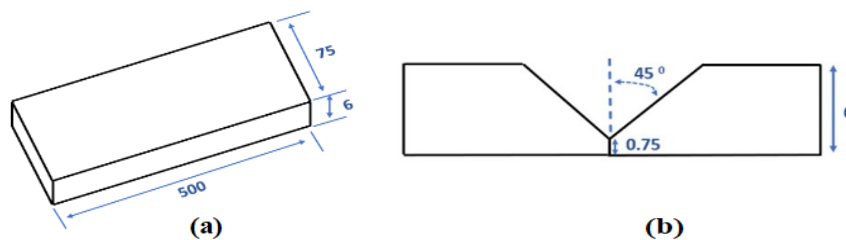


Figure 4.1. (a) Dimensions of the extruded BM and (b) Single V-groove joint (mm).

Table 4.2. The welding parameters used.

	Current (Amp.)	Voltage (V)	Travel speed (m/min)	Wire feed speed (m/min)
1 <sup>st</sup> Pass	163 ± 4	21.5 ± 0.5	0.5	4.5 ± 0.3
2 <sup>nd</sup> Pass	110 ± 5	22 ± 0.7	0.27	3.2

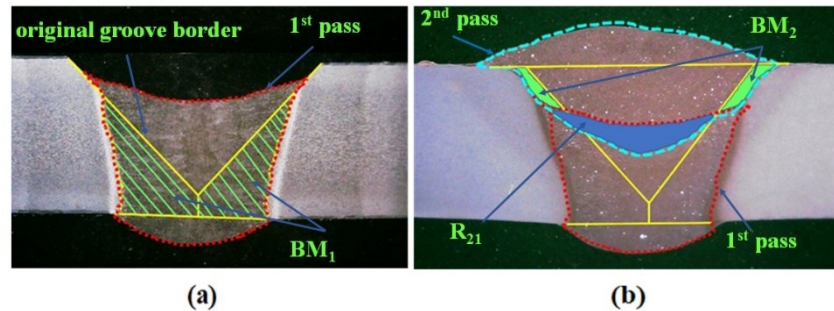


Figure 4.2. Macroview of a typical cross section joint for the dilution calculation. The areas for the (a) first pass and (b) second pass.

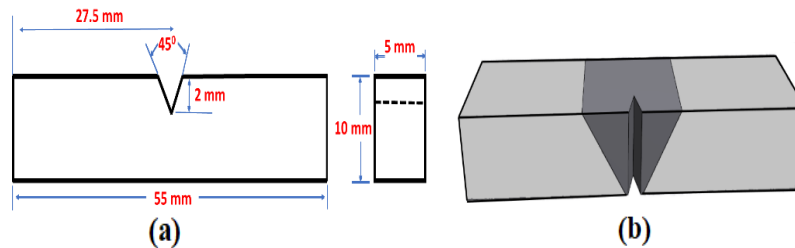


Figure 4.3. (a) Dimensions of the impact samples and their notches. (b) The notch position in the weld zone [17].

Table 4.3. The calculated chemical compositions in the first and second passes (wt.%)

		Si	Mg	Mn	Fe	Cu
<b>First pass</b>	ER4043	3.25	0.34	0.21	0.17	0.29
	ER4943	3.63	0.55	0.23	0.17	0.28
	FMg0.6	3.51	0.67	0.32	0.16	0.27
	FMg1.4	3.39	1.12	0.35	0.18	0.30
	Mg0.6Mn	3.83	0.68	0.47	0.16	0.31
	Mg1.4Mn	3.59	0.82	0.28	0.09	0.28
<b>Second pass</b>	ER4043	4.22	0.16	0.10	0.16	0.12
	ER4943	5.21	0.46	0.24	0.16	0.16
	FMg0.6	5.26	0.63	0.27	0.15	0.11
	FMg1.4	4.52	1.07	0.37	0.18	0.15
	Mg0.6Mn	4.44	0.66	0.48	0.15	0.13
	Mg1.4Mn	4.40	1.08	0.39	0.13	0.09

## 4.3 Results and Discussion

### 4.3.1 Microstructure

Figure 4.4 shows the optical microstructure of the FMg1.4 joint, which is a typical example of a newly developed filler metal. Figure 4.4(a) displays the OM image of the first pass, which consists of  $\alpha$ -Al dendrite cells/grains as the matrix and the surrounding eutectic Al-Si. In the second pass, the amount of eutectic Al-Si increased, and the  $\alpha$ -Al cells/grains coarsened (Figure 4.4(b)) due to lower BM dilution and a lower cooling rate relative to the first pass. Figure 4.4(c) shows the effect of the heat input to the second pass on the microstructure of the first pass. The heat introduced in the second pass resulted in the fragmentation of the eutectic Al-Si network and partial spheroidizing of eutectic Si particles in the transition zone of the first pass.

Figure 4.5(a–c) and Figure 4.6 show the SEM micrographs and the EDs analysis, respectively, of the as-welded FZs of the three filler metals. The attention was focused on the microstructures of the second pass, as they revealed large differences between the joints using low-Mg reference fillers and the new high-Mg fillers. Generally, the microstructure comprises  $\alpha$ -Al, eutectic Si, primary  $Mg_2Si$ ,  $\alpha$ -Al(FeMn)Si, and  $\beta$ -AlFeSi intermetallics. As Mn content increased in the new fillers, including the FMg0.6 and Mg1.4Mn joints (Table 4.2), the plate-like  $\beta$ -AlFeSi began to transfer into  $\alpha$ -Al(FeMn)Si [20]. In the Mg1.4Mn joint, the predominant Fe-rich intermetallic became  $\alpha$ -Al(FeMn)Si (Figure 4.5(c)). Even in the absence of Mg in the ER4043 reference filler (Figure 4.5(a)), some  $Mg_2Si$  particles were still observed in the FZ, owing to dilution from the BM. The volume fractions of the  $Mg_2Si$  in the reference fillers ER4043 and ER4943 were  $0.15\pm 0.08$  and  $0.43\pm 0.12\%$ , respectively, whereas in the new fillers, the fractions of  $Mg_2Si$  were significantly higher, being

0.75±0.21% and 1.43±0.25% in the fillers containing 0.6 and 1.4% of Mg, respectively. The volume fraction of Fe-rich intermetallics was dependent on the Mn content. The reference fillers have a volume fraction of  $0.88 \pm 0.24$ , whereas the fillers containing 0.25 and 0.5% Mn have volume fractions of  $1.68 \pm 0.32\%$  and  $2.31 \pm 0.27\%$ , respectively.

Figure 4.5(d–f) show the microstructures of the three filler metals under the PWHT conditions. The heat treatment had a significant effect on the microstructure. The eutectic Si was spheroidized, and the  $\beta$ -AlFeSi intermetallic particles were partially fragmented [21]. This fragmentation is associated with the partial dissolution of Fe-rich intermetallics and their connected eutectic constituents, such as  $Mg_2Si$  [22-24]. Meanwhile, the  $\alpha$ -Al(FeMn)Si particles were not affected by the PWHT because they are more stable than the  $\beta$ -AlFeSi particles, as shown in Figure 4.5(f) [23]. In the ER4043 and FMg0.6 samples, almost all  $Mg_2Si$  particles were completely dissolved (Figure 4.5(d, e)), whereas undissolved primary  $Mg_2Si$  particles remained in the Mg1.4Mn sample (Figure 4.5(f)), because the Mg content in this filler is higher than the maximum solubility of Mg at the solution treatment temperature of 550 °C, which is approximately 0.7 wt.% at this temperature [25].

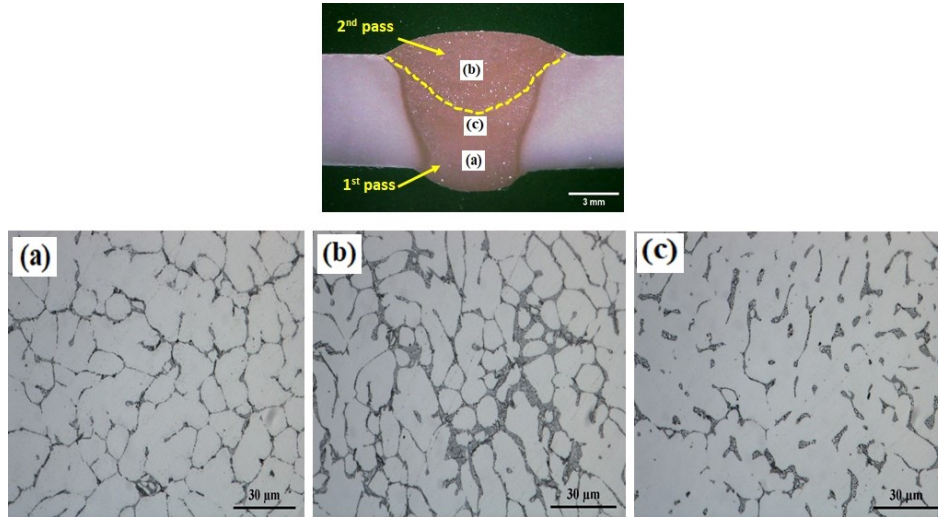


Figure 4.4. Optical microscopy of the different zones of the as-welded FMg1.4 joint. (a) and (b) show the microstructure in the first and second passes, respectively. (c) The heat affected zone in the first pass by the heat input of the second pass.

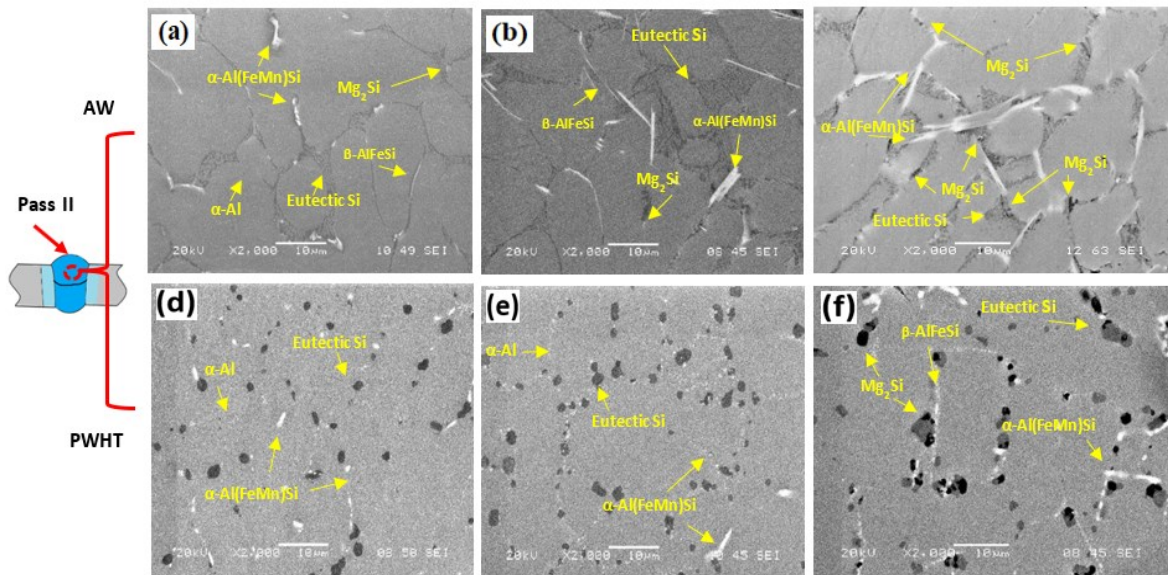


Figure 4.5. SEM images showing the microstructures of the second pass: (a) ER4043, (b) FMg0.6, and (c) Mg1.4Mn joints under the as-welded condition; and (d) ER4043, (e) FMg0.6, and (f) Mg1.4Mn joints under the PWHT condition, respectively.

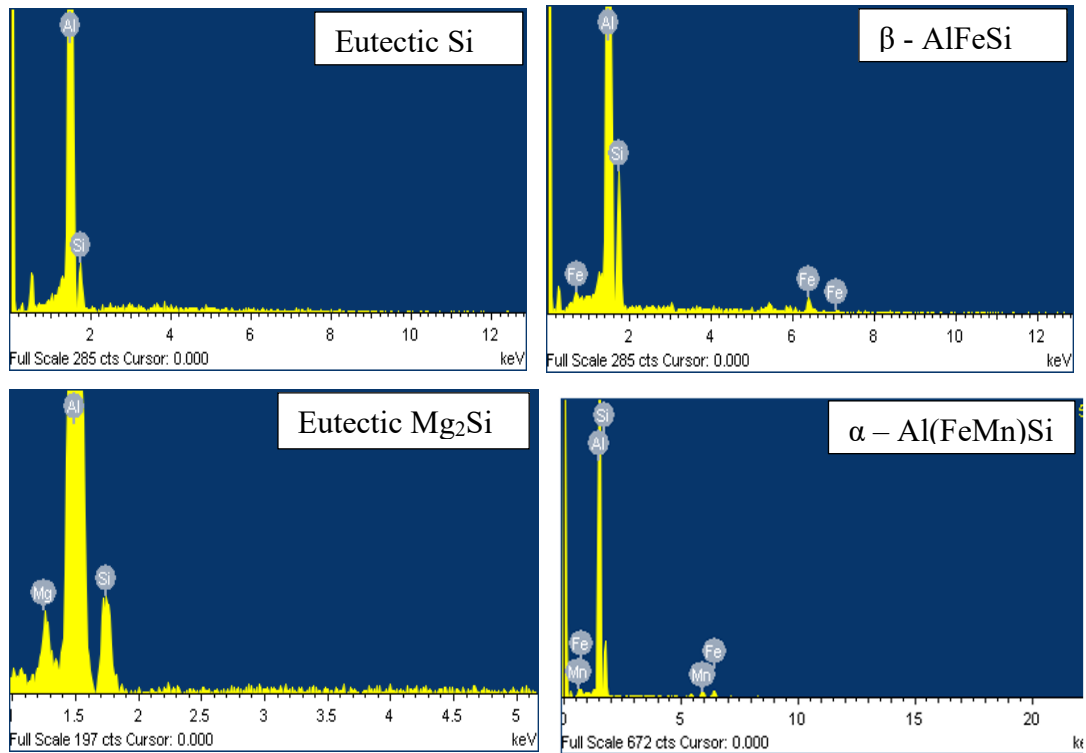


Figure 4.6. SEM-EDS analysis of the different phases identified in Figure 4.5.

TEM analysis was used to study the effect of PWHT on the precipitation of the joints, and the results are presented in Figure 4.7. The precipitates in all the FZs were MgSi-type phases, as expected in AA6011 heat-treatable alloys. Based on the morphology and size, the precipitates in the BM and all the joints except ER4043 joint were identified as  $\beta''$ -MgSi. In the ER4043 joint, they were  $\beta'$ -MgSi [26]. The BM exhibited a lower number density of the  $\beta''$  ( Figure 4.6 (a)) compared to the FZs of FMg0.6 and FMg1.4 joints, as shown in Figure 4.6 (c, d). This result is most likely attributed to the higher amount of Si in the FZs of FMg0.6 and FMg1.4 joints, which promotes the formation of the coherent  $\beta''$  precipitates [27]. The reason behind the formation of  $\beta'$  in the FZ of ER4043 (Figure 4.7 (b)) is the

insufficient Mg content in the joint because the ER4043 filler itself contains almost no Mg. In alloys with low Mg content,  $\beta'$  has been reported to precipitate at a lower temperature than  $\beta''$  [28, 29]. As the aging time is the same for all joints, the formation of  $\beta'$  was promoted in the ER4043 sample. A quantitative analysis of the precipitates is shown in Figure 4.7 (e). The BM had a low number density and volume fraction of the  $\beta''$ . The number density and volume fraction of the  $\beta''$  precipitates were comparable in the FMg0.6 and FMg1.4 joints, but their values were higher than the corresponding values in the BM. This implies that the Mg solutes dissolved in the low-Mg (FMg0.6) and high-Mg (FMg1.4) joints are mostly similar. As mentioned above, not all the primary  $Mg_2Si$  in the FMg1.4 joint can be dissolved during PWHT. Therefore, the strengthening effect of  $\beta''$  precipitates in both joints is expected to be similar. This result is consistent with the HV and tensile strength results discussed in the following sections.

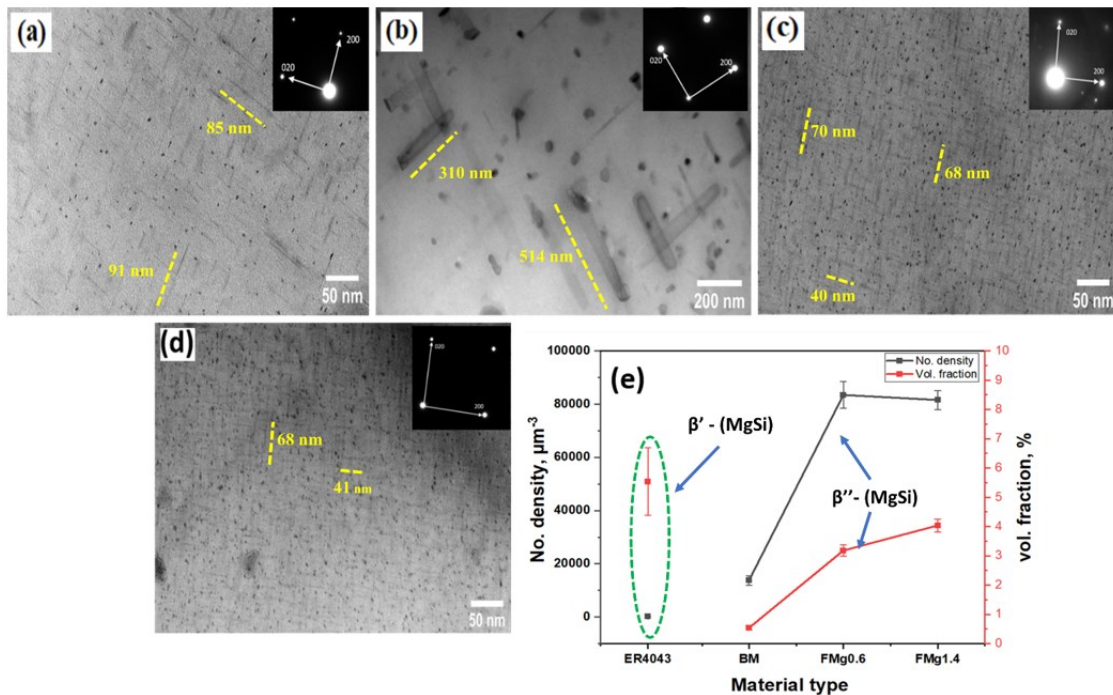


Figure 4.7. Bright-field TEM images of (a)  $\beta''$  precipitates in the BM; (b)  $\beta'$  precipitates in ER4043;  $\beta''$  precipitates in (c) FMg0.6 and (d) FMg1.4 joints. (e) Quantitative analysis of the precipitates.

## 4.3.2 Mechanical properties

### 4.3.2.1 Microhardness

The as-welded HV profiles of the reference and newly developed fillers are illustrated in Figure 4.8 (a, b). The FZs of the new fillers have higher HV values than those of the reference fillers. Moreover, the second pass yielded higher HV values (90–115 HV, Figure 4.8 (b)) than the first pass (86–107 HV, Figure 4.7 (a)) for all new fillers. The ER4043 joint exhibited the lowest HV values among all the filler metals used. However, it displayed a higher HV in the first pass than in the second pass (76 HV vs. 63 HV). This occurred because of the transfer of more Mg solutes from the BM in the first pass but less Mg in the second pass. The FZ of the ER4943 filler transferred similar HV values in both passes because the Mg content in both passes was within a similar range during dilution (Table 4.3). The Mg content in all the fillers played a more predominant role in the microhardness profiles than the Mn content. At the same Mg content, a higher Mn content in the FZ resulted in a slightly higher HV [30]; however, the effect was relatively weak. The order of the average HV in the FZ in both passes was FMg1.4 > Mg1.4Mn > Mg0.6Mn > FMg0.6, which was determined based on the calculated Mg and Mn contents, as shown in Table 4.3. The softest region in the AW condition was the HAZ, which was positioned approximately 8 mm from the center of the FZ, with a total length of approximately 18 mm, as shown in Figure 4.8 (a, b).

Figure 4.8 (c, d) show the HV profiles of the PWHT samples. The PWHT resulted in a significant increase in the HV values in both passes as well as in all fillers by promoting the precipitation strengthening arising from  $\beta''/\beta'$  (Figure 4.7). The new fillers showed higher HV values than the two reference fillers. In the new fillers, the average HV values were  $145 \pm 5$  HV in the first pass (Figure 4.8 (c)) and  $140 \pm 5$  HV in the second pass (Figure 4.8(d)).

The ER4043 joint exhibits the lowest HV value for both passes, followed by the ER4943 joint. In particular, the HV of the ER4043 joint in the second pass decreased to 96 HV, which is much lower than that in the first pass. This reduction in HV is attributed to the low Mg content in the FZ in the second pass and hence causes lower precipitation strengthening of coarse  $\beta'$  (Figure 4.7(b)). In the new fillers, the differences in HV between the fillers and passes were quite small owing to the limited Mg solubility and the similarity in the number densities of the precipitates, as shown in Figure 4.6 (e). Overall, PWHT was found to be effective in improving the HV of all the fillers, and the new fillers showed a large improvement in HV because of the high Mg content in the FZ compared to the low BM dilution in the reference ER4043 filler. The HAZ disappeared after the PWHT due to the recovery of strength in this zone and the re-precipitation of the  $\beta''$  strengthening phase in the matrix [18, 31].

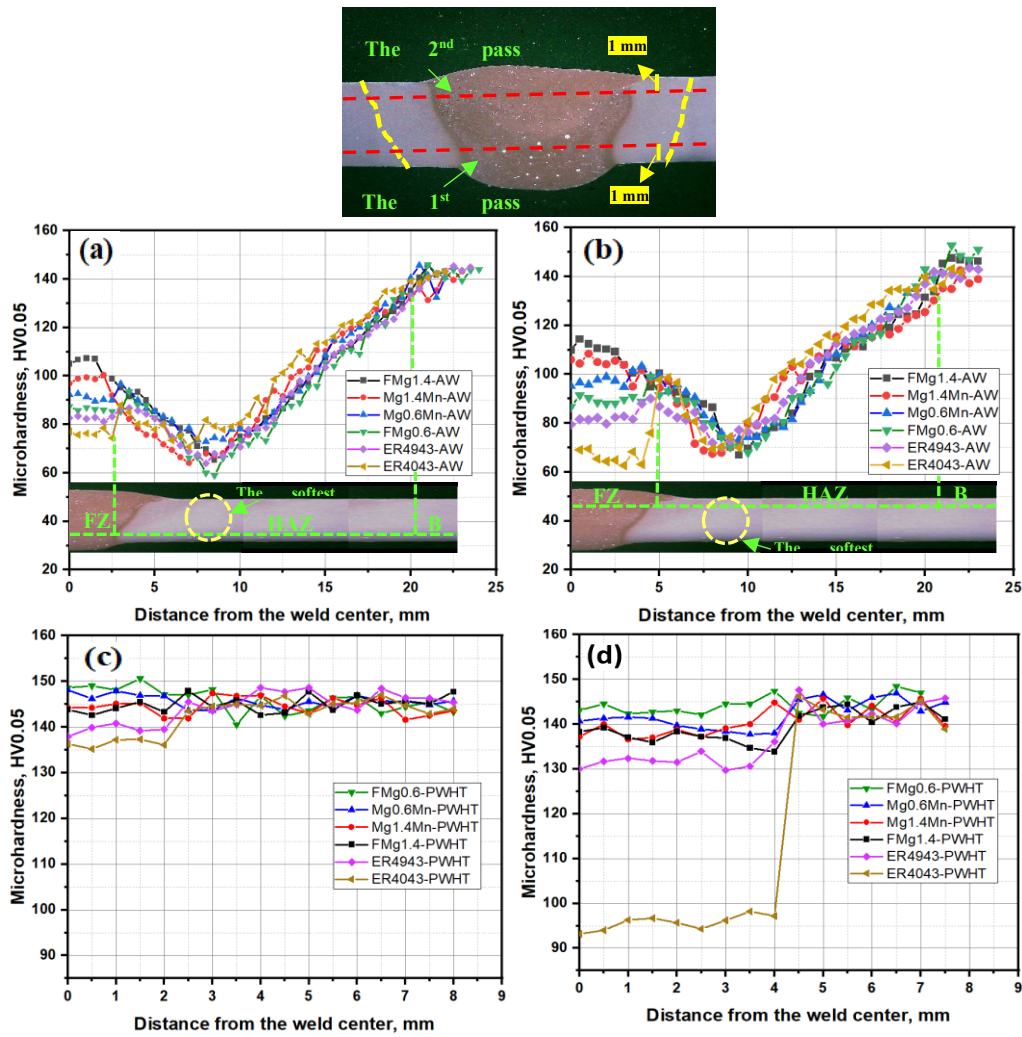


Figure 4.8. Hardness measurements in the joints for (a) first and (b) second passes in the as-welded condition and (c) first and (d) second passes in the PWHT condition.

#### 4.3.2.2 Tensile properties

The tensile properties of the as-welded joints are shown in Figure 4.9(a). All the tensile samples except for the ER4043 joint were fractured in the HAZ. The ER4043 joint was fractured in the FZ. The ER4043 joint presented the lowest YS and UTS of  $134 \pm 6$  and  $230 \pm 8$  MPa, respectively. This result is consistent with the HV results, as the lowest HV was

observed for the ER4043 filler (Figure 4.8(a, b)). The ER4943 filler and new filler joints displayed similar YS and UTS values of  $142 \pm 4$  and  $241 \pm 3$  MPa, respectively. This is attributed to the fact that the HAZ in all the joints was the softest zone and had the minimum HV, which was also observed in our previous study on AA6061 welding [18, 32]. The elongation of the as-weld joints exhibited a similar trend as for the tensile strength, with an average elongation of  $12 \pm 2\%$ , except in the case of the ER4043 joint, which produced the lowest elongation of  $9.5 \pm 0.8\%$ . The ER4043 filler had the lowest welding efficiency (52.5%) among all the fillers used. The average welding efficiency of all as-welded joints was approximately 54.4%, which indicates that almost 45% of the AA6011-T6 strength was lost during the welding process (see Figure 4.9(c)). The joint strength in the as-welded condition represented the strength of the HAZs because all the samples were fractured in this zone (except for the ER4043 joint). This implies that the actual strength of the FZs was higher than the obtained current strength. Figure 4.9(b) shows the tensile properties of the PWHT joints. The tensile strengths of all the joints were consistent with the HV results, showing a significant improvement relative to the as-welded condition owing to precipitation strengthening after PWHT. Fractures occurred in the FZs of all the welded joints. The ER4043 joint exhibited the lowest tensile strength (UTS of  $335 \pm 10$  MPa), and the ER4943 joint showed greater tensile strength with a UTS of  $373 \pm 5$  MPa due to the high Mg content in the filler. However, the tensile strengths of the two reference fillers were still lower than those of the new fillers, owing to the lower Mg content in the fillers relative to the new fillers. The average YS and UTS of the new fillers reached  $370 \pm 10$  and  $395 \pm 12$  MPa, respectively, which were still lower than those of the BM, although the number density and volume fraction of the  $\beta''$  strengthening phase in the FZs of the new fillers were higher than those of the BM as shown in Figure 4.7 (e). This is mostly due to the existence of welding

defects such as porosity, which will be discussed in the fracture analysis section [33]. In addition, the tensile strengths of the four new fillers were similar, as these strengths depended on the number density and volume fraction of  $\beta''$ . According to the TEM results (Figure 4.7), the number density and volume fraction of the  $\beta''$  precipitates in the low- and high-Mg fillers, such as FMg0.6 and FMg1.4, are similar. Due to its low tensile strength, the ER4043 joint produced the highest elongation of  $8.5 \pm 2\%$ . The elongation of the other fillers decreased considerably with the increasing Mg content [34]. The elongation of the ER4943 and FMg0.6 joints attained a similar value of  $6.5 \pm 1\%$ . These results demonstrate that an excellent combination of strength and ductility was achieved using the FMg0.6 filler. With a further increase in Mg in the fillers, such as in FMg1.4, or an increase in Mn in the fillers, such as in Mg0.6Mn and Mg1.4Mn, the elongation decreased remarkably. The reasons behind this reduced ductility are attributed to 1) the undissolved brittle primary  $Mg_2Si$  particles in the high-Mg filler and 2) the increase in the size and amount of  $\alpha-Al(FeMn)Si$  intermetallic particles in the high-Mn fillers (Figure 4.5(c, f)). The welding efficiency increased from 76.7% for the ER4043 joint to 85.5% for the ER4943 joint. On the other hand, the average welding efficiency of the four newly developed fillers was 90.1%, whereas the FMg0.6 joint achieved the highest efficiency of 93.8% (Figure 4.9(c)).

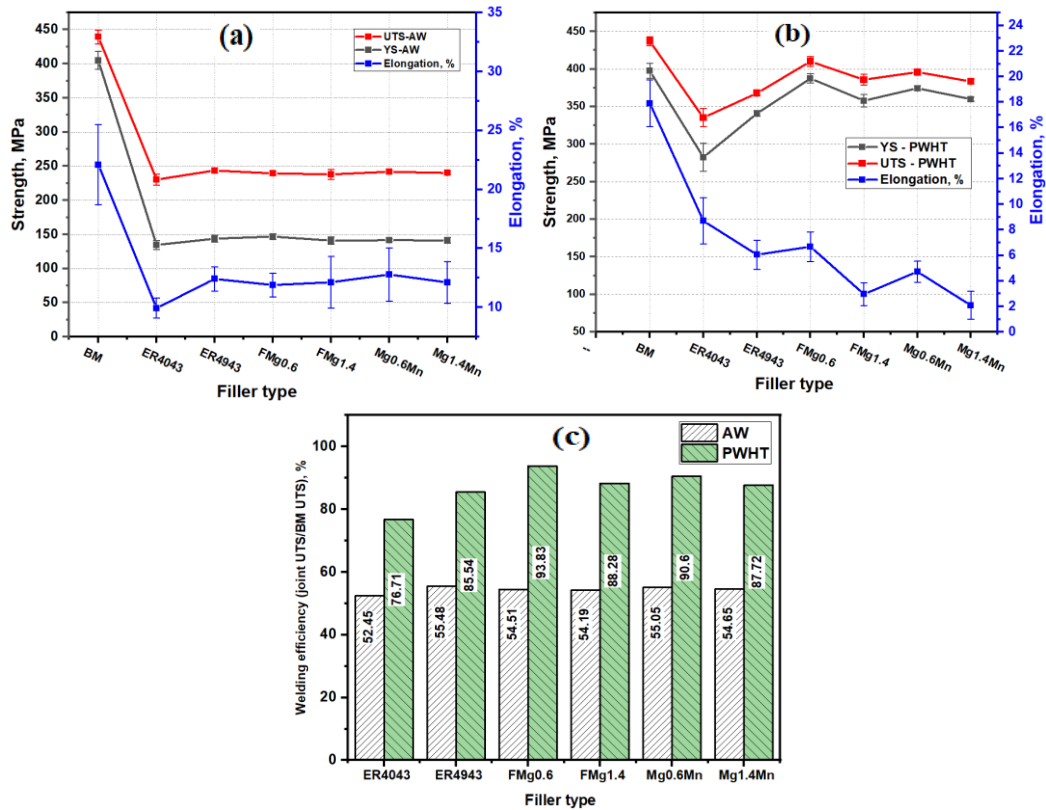


Figure 4.9. The tensile properties in the (a) as-welded and (b) PWHT conditions; (c) the welding efficiency in the as-welded and PWHT conditions.

### 4.3.2.3 Fracture analysis of tensile samples

Figure 4.10 shows the fracture surfaces of the PWHT tensile samples. Figure 4.10(a, b) show the pores formed during both passes in the ER4043 and Mg1.4Mn joints, respectively. A large number of pores were found in the second pass, whereas few but relatively large pores were observed in the first pass. This occurred because the heat input from the second pass resulted in gas release and caused the growth of pre-existing pores in the first pass [35, 36]. The fracture surfaces of the three joints (ER4043, FMg0.6, and Mg1.4Mn) in the first pass are illustrated in Figure 4.10(c–e). The fracture surface of the ER4043 joint showed large and deep dimples, indicating a ductile fracture. The fracture

surfaces of the FMg0.6 and Mg1.4Mn joints exhibited honeycomb-like shallow dimples, suggesting a more brittle fracture than that of the ER4043 joint. The dimples of the Mg1.4Mn joint were smaller and shallower than those of the FMg0.6 joint, indicating its more brittle nature. Broken particles, primarily Si and  $\alpha$ -Fe intermetallic particles, were observed at the bottom of the dimples in the ER4043 joint and the joints with low Mg content fillers (e.g., FMg0.6 and Mg0.6Mn). In joints with high Mg content fillers (e.g., FMg1.4 and Mg1.4Mn), the broken  $\alpha$ -Fe intermetallic particles with the undissolved primary Mg<sub>2</sub>Si particles were observed in the bottom of the dimples. Both  $\alpha$ -Fe intermetallic and primary Mg<sub>2</sub>Si particles were mainly distributed along interdendritic boundaries. Moreover, microcracks can easily initiate and propagate along these brittle particles [37, 38].

The fracture surfaces of the second pass under the PWHT condition are shown in Figure 4.10(f–h). Similar to the first pass, the ER4043 joint had a fracture surface, indicating a more ductile fracture in the second pass, whereas the dimples on the new filler joints were smaller and shallower than those of the ER4043 joint. The FMg0.6 joint showed relatively larger dimples, illustrating better ductility than the Mg1.4Mn joints, which is consistent with the measured elongations (see Figure 4.9). Owing to the high Si content in the second pass, a larger number of fractured Si particles were observed than in the first pass.

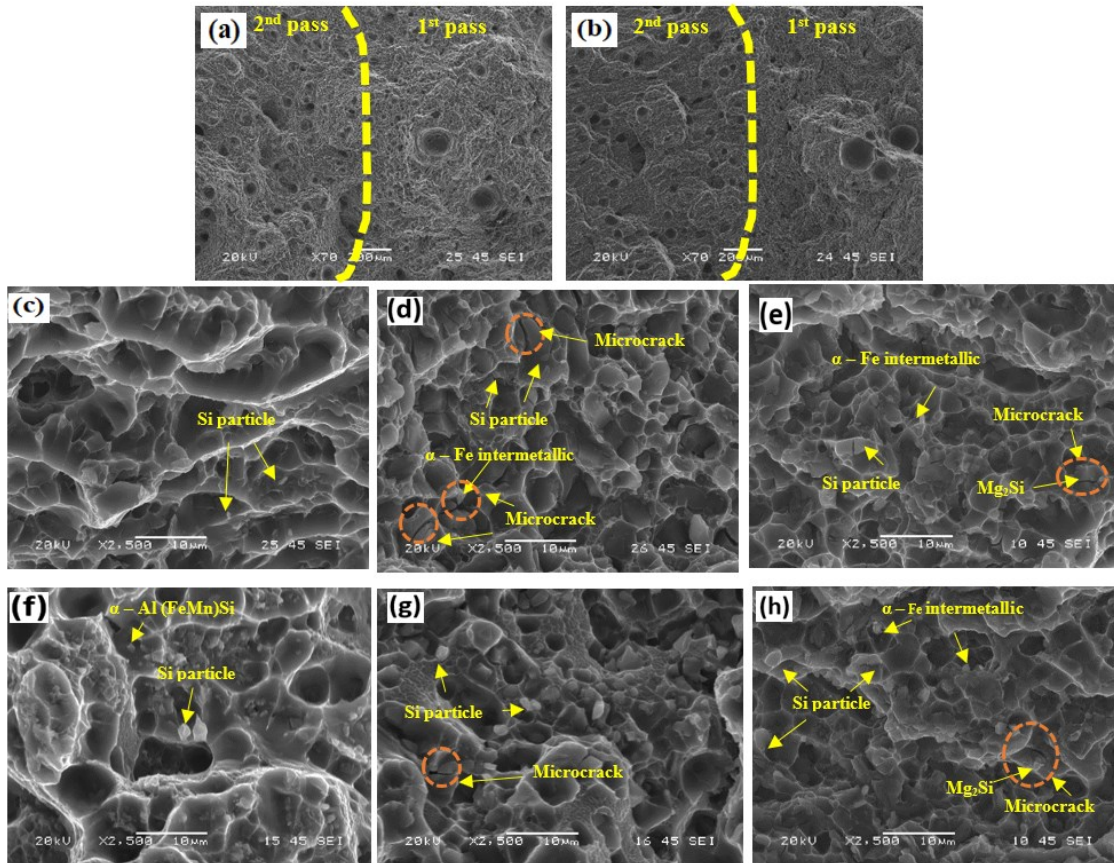


Figure 4.10. Fracture surfaces of the PWHT tensile samples. Porosity in the (a) ER4043 and (b) Mg1.4Mn joints. (c–e) First pass of ER4043, FMg0.6, and Mg1.4Mn joints. (f–h) Second pass of ER4043, FMg0.6, and Mg1.4Mn joints.

#### 4.3.2.4 Charpy impact toughness

Figure 4.11 shows the impact toughness of the BM, HAZ, and FZ of the joints under as welded and PWHT conditions. The HAZ exhibited the highest impact toughness (21.83 J), representing the highest absorbed energy relative to the FZ of all the joints. The impact toughness in the HAZ can be attributed to the effect of the welding heat input, which resulted in the dissolution and coarsening of the  $\beta''$  precipitates and the HAZ becoming the softest region in the joints ( Figure 4.8 (a, b)), which could absorb the impact energy. The BM

presented the second highest value of impact toughness of 10.35 J, owing to the absence of macro-defects, such as porosity in the extruded plate, and the best ductility compared to the welded joints (Figure 4.9(a)). Under the as-weld condition, the ER4043 and ER4943 joints showed higher values of impact toughness (5.03 and 4.07 J) compared to those of the new filler joints. The joints with the fillers containing 0.6% Mg (FMg0.6 and Mg0.6Mn) had an impact toughness of  $2.38 \pm 0.07$  J, whereas the joints with the high Mg fillers containing 1.4% Mg (FMg1.4 and Mg1.4Mn) could absorb the impact energy up to  $1.3 \pm 0.01$  J. The decrease in the impact toughness with increasing Mg contents in the new fillers is mainly attributed to 1) the increased amount of primary Mg<sub>2</sub>Si particles (Figure 4.5(b–c)), which can act as a stress riser and promote the formation of microcracks [39], and 2) the increasing Mg solutes in the matrix, thereby retarding the dislocation movement. In the case of the impact test, the dislocations had no time to override the Mg effect owing to the high strain rate; hence, less impact energy was absorbed.

The joints subjected to PWHT exhibited a moderate improvement in impact toughness compared with those subjected to the as-welded condition. This improvement can be attributed to a few factors, including the spheroidization of eutectic Si particles and the dissolution of primary Mg<sub>2</sub>Si particles during solution treatment (Figure 4.5(d–f)) [16]. Under the PWHT condition, the ER4043 and ER4943 joints achieved impact toughness values of  $6 \pm 0.7$  and  $4.93 \pm 0.35$  J. Despite the improved impact toughness of the PWHT samples, the joints with the new fillers still exhibited lower toughness than the joints with the two reference fillers. This difference in impact toughness is mostly due to the precipitation of the high number density of the β'' strengthening phase in the joints with the

new fillers, resulting in high tensile strength but relatively low elongation (the trade-off between strength and ductility) [40, 41].

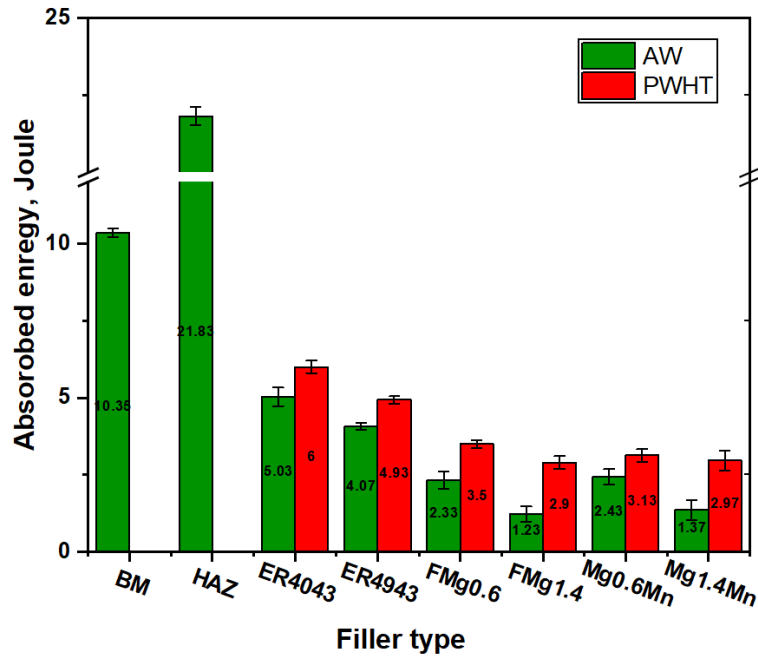


Figure 4.11. Impact toughness of the BM, HAV, and FZ of all joints under as welded and PWHT conditions.

#### 4.3.2.5 Fracture analysis of impact samples

Figure 4.12 shows the fracture surfaces of the as-welded impact samples. A higher level of plastic deformation was observed in the HAZ than in the ER4043 or any other joint. A typical example of the macroviews of the HAZ and ER4043 fractures is shown in Figure 4.12(a, b). The HAZ exhibited large and deep dimples, showing significant deformation, and high impact energy was absorbed (Figure 4.12(c)) [42]. The fracture surfaces of the ER4043 joint still exhibited ductile fractures in the first and second passes, as shown in Figure 4.12(d, e). Figure 4.12(f, g) depict the fracture surfaces of the high Mg filler (FMg1.4) in the first and second passes, respectively. In both passes, the cleavage facets became the dominant

feature of the fracture, with only a few small dimples. This brittle fracture in the FMg1.4 joint is caused by the high amount of primary  $Mg_2Si$  and Fe-rich intermetallic particles, which results in low ductility and premature failure. Furthermore, secondary cracks were observed in the fracture surfaces of the FMg1.4 joint in both passes (see the yellow arrows), which mainly started from the primary  $Mg_2Si$  and Fe-rich intermetallic particles.

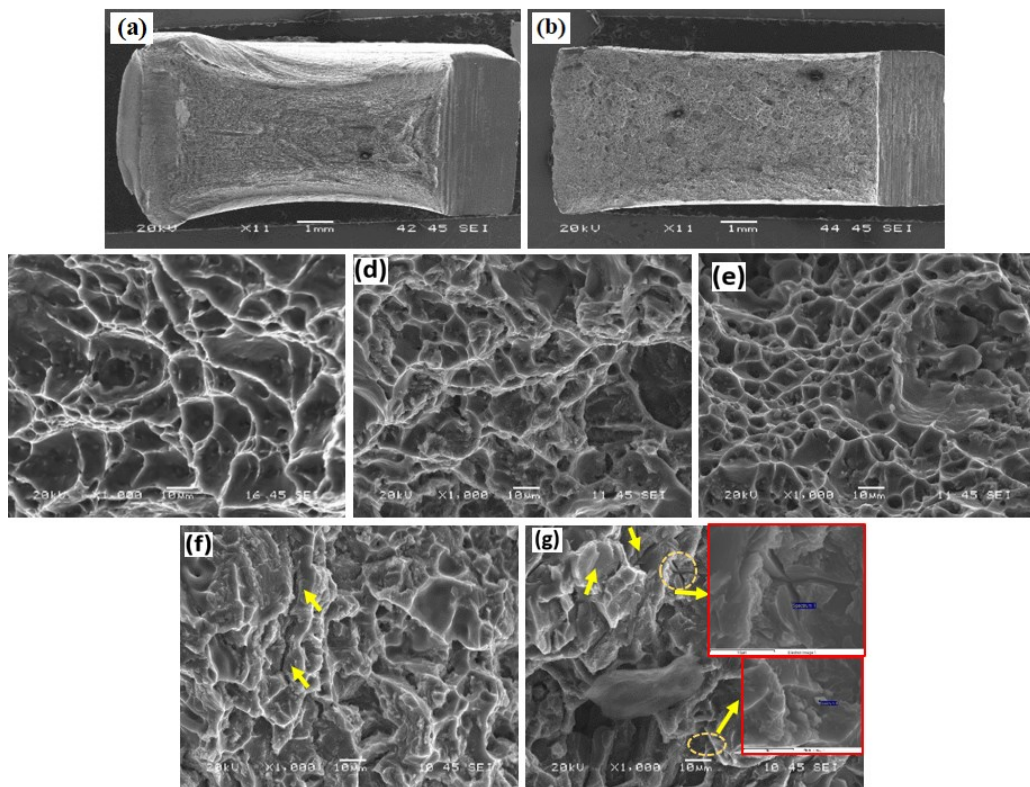


Figure 4.12. Fracture surfaces of the impact samples under as-welded condition: Macroviews of the (a) HAZ and (b) ER4043 joint in the first pass. Macroviews of the (c) HAZ, (d) and (e) ER4043 joint in the second pass. Macroviews of the FMg1.4 joint in the (f) first and (g) second passes.

### 4.3.3 Comparison of the welding efficiency of various Al-Mg-Si alloys

Table 4.4 shows a comparison of the welding efficiency of the newly developed fillers with previously reported fusion welding efficiencies of various Al-Mg-Si alloys under AW and PWHT conditions. The welding efficiency under the AW condition when the commercial fillers ER4043 or ER4943 are used for various Al-Mg-Si 6xxx-based materials with different thicknesses ranges from 33.6 to 69.7%, with an average value of 54.6%. The average efficiency of the different 6xxx alloy welds was consistent with that of the newly developed fillers ( Figure 4.9(c)). This suggests that the welding efficiency under the AW condition was almost independent of the welding technique (tungsten inert gas (TIG) vs. gas metal arc welding (GMAW)), the base materials, and their thickness. The fractures of the tensile samples commonly occurred in the FZ or HAZ. This is primarily attributed to the occurrence of weldment flaws or defects in the FZs and an insufficient strengthening source in the FZs (using ER4043/4943 fillers), which results in a considerable reduction in the FZ strength. When the FZ becomes stronger, such as when using the new fillers in this work, the weakest region of the welding is transferred to the HAZ, where the precipitation strengthening of the 6xxx alloys is largely demolished.

Generally, PWHT weldments exhibit much better welding efficiency than AW weldments. This is due to the formation of the  $\beta''/\beta'$  strengthening phase in the FZ and the strength recovery of the HAZ. The fracture of the tensile samples for all 6xxx alloys occurred only in the FZ because the heat treatment removed the HAZ. Under the PWHT conditions, the welding efficiency when the ER4043/493 fillers are used for various 6xxx alloys ranged from 51.5 to 85.5%, with an average value of 70.7%. The average welding efficiency of the newly developed fillers with the base material AA6011 was 90.1% ( Figure 4.9(c)), whereas

the new FMg0.6 filler exhibited the highest efficiency of 93.8% among all welded materials listed in Table 4.4. This is primarily attributed to the higher Mg content in the new filler metals and, hence, the higher precipitation-strengthening effect in the FZ compared to the ER4043/493 reference fillers (Table 4.3).

Table 4.4. Comparison of the welding efficiency for various Al-Mg-Si alloy fusion welding in both AW and PWHT conditions.

	No	BM (thickness)	Filler	Technique	Efficiency, %	Fracture	Reference
AW	1	6061 (6mm)	4043	TIG	33.6	FZ	[43]
	2	6061 (3 mm)	4943	TIG	58.1	FZ	[44]
	3	6082 (3 mm)	4043	TIG	48.3	FZ	[45]
	4	6082 (3 mm)	4043 (0.35Ti)	TIG	57.1	FZ	[45]
	5	6082 (4mm)	4043	TIG	69.7	HAZ	[46]
	6	6061 (6.35 mm)	4043	GMAW	53.3	FZ	[47]
	7	6061(9 mm)	4043	GMAW	54.4	HAZ	[31]
	8	6061(9.5mm)	4043	GMAW	58.7	FZ	[48]
	9	6061 (12.7 mm)	4043	GMAW	56.1	FZ	[49]
	10	6011 (6 mm)	4043	GMAW	56.1	HAZ	This work
	11	6011 (6 mm)	4943	GMAW	55.5	HAZ	This work
	12	6011 (6 mm)	Mg1.4Mn	GMAW	54.7	HAZ	This work
	13	6011 (6 mm)	FMg0.6	GMAW	54.2	HAZ	This work
PWHT	1	6061 (2.5 mm)	4043	TIG	74.2	FZ	[50]
	2	6061 (6.36 mm)	4043	TIG	51.5	FZ	[51]
	3	6082 (3 mm)	4043 (0.35Ti)	TIG	61.5	FZ	[45]
	4	6082 (12 mm)	4043	TIG	64.3	FZ	[52]
	5	6061 (3 mm)	4043	GMAW	76.0	FZ	[53]
	6	6061 (6.35 mm)	4043	GMAW	85.1	FZ	[47]
	7	6061 (9 mm)	4043	GMAW	53.0	FZ	[31]
	8	6061 (12.7 mm)	4043	GMAW	62.3	FZ	[49]
	9	6005 (3.2 mm)	4043	GMAW	80.1	FZ	[54]
	10	6063 (6.4mm)	4043	GMAW	78.1	FZ	[54]
	11	6011 (6 mm)	4043	GMAW	76.7	FZ	This work
	12	6011 (6 mm)	4943	GMAW	85.5	FZ	This work
	13	6011 (6 mm)	Mg1.4Mn	GMAW	87.7	FZ	This work
	14	6011 (6 mm)	FMg0.6	GMAW	93.8	FZ	This work

#### 4.3.4 Discussion

In the present work, it was confirmed that using a commercial ER4043 filler (free of Mg) for welding a high-strength AA6011 alloy produced inferior strength and low welding efficiency because of the low dilution and insufficient Mg in the weldments. ER4943 filler with Mg increased to 0.4 wt.% improved the strength and welding efficiency. Further increasing the Mg and Mn contents in the newly developed fillers led to high dilution and an increase in the alloying elements (mainly Mg and Mn) in the FZ, resulting in higher solid solution strengthening and higher microhardness in the FZ under the AW condition. However, the softest region of the joint in the AW condition was the HAZ, because the highest amount of  $\beta''$ -MgSi strengthening precipitates were dissolved in the HAZ due to the high welding temperature [18]. The joint strength under AW conditions was controlled by the strength of the HAZ ( Figure 4.9(a)). Therefore, the new fillers with high Mg and Mn contents did not show a significant benefit under AW conditions in terms of strength and welding efficiency compared to the two reference fillers.

Because the newly developed fillers provided sufficient Mg in the FZ, a large volume fraction of fine  $\beta''$ -MgSi was precipitated in the FZ during PWHT (Figure 4.6), resulting in superior strength and higher welding efficiency compared to the reference fillers ( Figure 4.9(b, c)). The FMg0.6 filler, containing 0.6 wt.% Mg, achieved the best combination of strength and elongation and the highest welding efficiency among the four new fillers studied. Upon increasing the Mg content to 1.4 wt.% (such as in FMg1.4 and Mg1.4Mn fillers), the tensile strength remained at a similar level because the primary  $Mg_2Si$  could not fully dissolve in the FZ during the solution treatment due to the Mg solubility limit (Figure 4.5(f)). However, the elongation decreased remarkably for the higher-Mg fillers. The

increase in Mn content in the novel fillers at the same Mg content (Mg0.6Mn and Mg1.4Mn fillers) did not enhance the strength of the joints but rather reduced the elongation. Therefore, the Mg level in the filler metal plays a predominant role in improving the tensile strength and welding efficiency of high-strength AA6011 joints.

#### 4.3.5 Conclusions

1. During the welding of thick plates of high-strength AA6011 alloy using multiple passes, increasing the Mg and Mn contents of the Al-Si-Mg 4xxx filler metals resulted in sufficiently higher alloying elements in the FZ compared to the ER4043/ER4943 reference fillers, resulting in higher microhardness in the weldments.
2. Under the AW condition, the weakest region of the joint was the HAZ because the highest amount of  $\beta''$ -MgSi strengthening precipitates in the AA6011 alloy were dissolved. The joint strength was almost independent of the filler type and was controlled by the HAZ strength. The average welding efficiency of the as-welded joints was 54.4%.
3. The higher Mg contents in the newly developed fillers promoted the precipitation of a large volume fraction of fine  $\beta''$ -MgSi in the FZ during PWHT, resulting in superior strength and higher welding efficiency relative to the reference fillers. The Mg in the filler metals played a predominant role in improving the tensile strength and welding efficiency of the high-strength AA6011 joints.
4. The optimal Mg content of the filler metals was 0.6 wt.%. Upon further increasing the Mg content, the tensile strength remained at the same level, but the elongation decreased significantly. The novel fillers with 0.6% Mg content exhibited a complete

dissolution of  $Mg_2Si$  particles after PWHT, whereas the fillers with 1.4% Mg content retained undissolved  $Mg_2Si$  in the matrix owing to the Mg solubility limit. The increased Mn content in the filler metals had an insignificant effect on joint strength but caused a reduction in elongation.

5. The novel FMg0.6 filler containing 0.6% Mg achieved the best combination of strength and elongation after PWHT among all the filler metals studied. In addition, the FMg0.6 filler exhibited the highest welding efficiency of 94% when comparing the data collected for all the welded Al-Mg-Si 6xxx alloys.
6. The newly developed fillers adversely affected the impact toughness of the joints under both AW and PWHT conditions. After performing the PWHT, the impact toughness of the novel fillers improved but was still lower than that of the reference fillers.

#### 4.4 References

1. Mishra, R. S.; Ma, Z. Y. Friction stir welding and processing. *Mater. Sci. Eng. R Rep.*, **2005**, *50*, 1-78.
2. Norman, A. F.; Birley, S. S.; Prangnell, P. B. Development of new high strength Al–Sc filler wires for fusion welding 7000 series aluminium aerospace alloys. *Sci. Technol. Weld. Joining*, **2003**, *8*, 235-245.
3. Francis, J. A.; Bednarz, B.; Bee, J. V. Prediction of steady state dilution in multipass hardfacing overlays deposited by self shielded flux cored arc welding. *Sci. Technol. Weld. Joining*, **2002**, *7*, 95-101.
4. Sun, Y. L.; Hamelin, C. J.; Flint, T. F.; Vasileiou, A. N. Prediction of Dilution and Its Impact on the Metallurgical and Mechanical Behavior of a Multipass Steel Weldment. *J. Press. Vessel Technol.*, **2019**, *141*.
5. Vahid, H.; Kjell, H.; Leif, K. Bead by bead study of a multipass shielded metal arc-welded super-duplex stainless steel. *World Weld.*, **2020**, *64*, 283-299.
6. Shahi, A. S.; Sunil, P. Modelling of the effects of welding conditions on dilution of stainless steel claddings produced by gas metal arc welding procedures. *Mater. Process. Technol.*, **2008**, *196*, 339-344.
7. Mousavi, M. G.; Cross, C. E.; Grong, Ø.; Hval, M. Controlling weld metal dilution for optimised weld performance in aluminium. *Sci. Technol. Weld. Joining*, **1997**, *2*, 275-278.
8. Coniglio, N.; Cross, C. E.; Michael, T.; Iammers, M. Defining a critical weld dilution to avoid solidification cracking in aluminum. *Weld. J.*, **2008**, *87*, 237s-247s.
9. Ramanaiah, N.; Balakrishna, B.; Rao, K. P. Effect of Modified AA5356 Filler on Corrosion Behavior of AA6061 Alloy GTA Welds. *IJMER*, **2012**, *2*, 4429-33.
10. Ramanaiah, N.; Rao, K. P. Effect of modified AA4043 filler on corrosion behavior of AA6061 alloy GTA welds. *Int. J. Adv. Manuf. Technol.*, **2013**, *64*, 1545-1554.
11. Schmitt, W.; Sun, D.-Z.; Böhme, W. Evaluation of fracture toughness based on results of instrumented Charpy tests. *Int. J. Press. Vessel & Pip*, **1994**, *59*, 21-29.
12. Li, Z.; Samuel, A. M.; Samuel, F. H.; Ravindran, C. Parameters controlling the performance of AA319-type alloys: Part II. Impact properties and fractography. *Mater. Sci. Eng. A* . **2004**, *367*, 111-122.

13. Basavakumar, K.; Mukunda, P.; Chakraborty, M. Impact toughness in Al–12Si and Al–12Si–3Cu cast alloys—Part 1: Effect of process variables and microstructure. *Int. J. Impact Eng.*, **2008**, *35*, 199-205.
14. Murali, S.; Raman, K. S.; Murthy, K. S. S. Effect of magnesium, iron (impurity) and solidification rates on the fracture toughness of Al7Si0.3Mg casting alloy. *Mater. Sci. Eng., A*, **1992**, *151*, 1-10.
15. Abuhasel, K. A.; Ibrahim, M. F. A.; Elgallad, E. M.; Samuel, F. H. On the impact toughness of Al–Si cast alloys. *Mater. Des.*, **2016**, *91*, 388-397.
16. Elsebaie, O.; Samuel, A. M.; Samuel, F. H. Effects of Sr-modification, iron-based intermetallics and aging treatment on the impact toughness of 356 Al–Si–Mg alloy. *J. Mater. Sci.*, **2011**, *46*, 3027-3045.
17. Mosneaga, V.; Mizutani, T.; Kobayashi, T.; Toda, H. Impact toughness of weldments in Al–Mg–Si alloys. *Mater. Trans.*, **2002**, *43*, 1381-1389.
18. Ahmed, M.; Javidani, M.; Mirakhorli, F.; Maltais, A.; Chen, X. G. Developing High-Strength Al-Si-Mg Filler Metals for Aluminum Fusion Welding. *J. Mater. Eng. Perform.*, **2023**, *32*, 2218-2227.
19. Brungraber, R. J.; Nelson, F. G. Effect of welding variables on aluminum alloy weldments. *Weld. Res. Counc.*, **1973**, *52*, 97s.
20. Seifeddine, S.; Svensson, I. L. The influence of Fe and Mn content and cooling rate on the microstructure and mechanical properties of A380-die casting alloys. *Metall. Res. Technol.*, **2009**, *27*.
21. Beroual, S.; Boumerzoug, Z.; Paillard, P.; Borjon-Piron, Y. Effects of heat treatment and addition of small amounts of Cu and Mg on the microstructure and mechanical properties of Al-Si-Cu and Al-Si-Mg cast alloys. *J. Alloys Compd.*, **2019**, *784*, 1026-1035.
22. Moustafa, M. A. Effect of iron content on the formation of  $\beta$ -Al5FeSi and porosity in Al–Si eutectic alloys. *Mater. Process. Technol.*, **2009**, *209*, 605-610.
23. Kumar, S.; Grant, P. S.; O'Reilly, K. A. Q. Fe bearing intermetallic phase formation in a wrought Al–Mg–Si alloy. *Trans. Indian Inst. Met.*, **2012**, *65*, 553-557.
24. Liu, Y. L.; Kang, S. B. The solidification process of Al–Mg–Si alloys. *J. Mater. Sci.*, **1997**, *32*, 1443-1447.
25. ASM-International, Heat Treating—Heat Treating of Aluminum Alloys. ASM International: 1991.

26. Vissers, R.; Huis, M. A. V.; Jansen, J.; Zandbergen, H. W. The crystal structure of the  $\beta'$  phase in Al–Mg–Si alloys. *Acta Mater.*, **2007**, *55*, 3815-3823.
27. Gupta, A. K.; Lloyd, D. J.; Court, S. A. Precipitation hardening in Al–Mg–Si alloys with and without excess Si. *Mater. Sci. Eng., A*, **2001**, *316*, 11-17.
28. Wang, Q. G.; Davidson, C. J. Solidification and precipitation behaviour of Al-Si-Mg casting alloys. *J. Mater. Sci.*, **2001**, *36*, 739-750.
29. Girelli, L.; Tocci, M.; Gelfi, M.; Pola, A. Study of heat treatment parameters for additively manufactured AlSi10Mg in comparison with corresponding cast alloy. *Mater. Sci. Eng. A* . **2019**, *739*, 317-328.
30. Nam, S. W.; Lee, D. H. The effect of Mn on the mechanical behavior of Al alloys. *Met. Mater.*, **2000**, *6*, 13-16.
31. Pérez, J. S.; Ambriz, R. R.; López, F. F. C. Recovery of mechanical properties of a 6061-T6 aluminum weld by heat treatment after welding. *Metall. Mater. Trans. A*, **2016**, *47*, 3412-3422.
32. Ahmed, M.; Javidani, M.; Maltais, A.; Chen, X.-G. Welding of AA6061-T6 Sheets Using High-Strength 4xxx Fillers: Effect of Mg on Mechanical and Fatigue Properties. *Materials*, **2023**, *16*, 3832.
33. Wang, L.; Liu, Y.; Yang, C.; Gaos, M. Study of porosity suppression in oscillating laser-MIG hybrid welding of AA6082 aluminum alloy. *J. Mater. Process. Technol.*, **2021**, *292*, 117053.
34. Pedersen, L.; Arnberg, L. The effect of solution heat treatment and quenching rates on mechanical properties and microstructures in AlSiMg foundry alloys. *Metall. Mater. Trans. A*, **2001**, *32*, 525-532.
35. Fahlström, K.; Blackburn, J.; Karlsson, L. Low Porosity in Cast Magnesium Welds by Advanced Laser Twin-Spot Welding. *Mater. sci. appl.*, **2018**, *10*, 53-64.
36. Fahlström, K.; Blackburn, J.; Karlsson, L. Effect of Laser Welding Parameters on Porosity of Weldsin Cast Magnesium Alloy AM50. *MAMS*, **2018**, *1*, 25-32.
37. Bo, L.; Xiangxiang, H.; Rui, X.; Yuliang, Z.; Yemao, L. Evolution of iron-rich intermetallics and its effect on the mechanical properties of Al–Cu–Mn–Fe–Si alloys after thermal exposure and high-temperature tensile testing. *jmr&t*, **2023**, *23*, 2527-2541.
38. Ibrahim, M. F.; S.A.Alkahtani; Abuhasell, K. A.; Samuel, F. H. Effect of intermetallics on the microstructure and tensile properties of aluminum based alloys: Role of Sr, Mg and Be addition. *Mater. Des.*, **2015**, *86*, 30-40.

39. Tocci, M.; Donnini, R.; Angella, G.; Pola, A. Tensile behavior and impact toughness of an AlSi3MgCr alloy. *Procedia Struct. Integr.*, **2017**, *3*, 517-525.
40. Merlin, M.; Timelli, G.; Bonollo, F.; Garagnani, G. L. Impact behaviour of A356 alloy for low-pressure die casting automotive wheels. *J. Mater. Process. Technol.*, **2009**, *209*, 1060-1073.
41. Zhang, D. L.; Zheng, L. H.; StJohn, D. H. Effect of a short solution treatment time on microstructure and mechanical properties of modified Al–7wt.% Si–0.3 wt.% Mg alloy. *J. Light Met.*, **2002**, *2*, 27-36.
42. Ambriz, R. R.; Jaramillo, D.; Garcia, C. Fracture energy evaluation on 7075-T651 aluminum alloy welds determined by instrumented impact pendulum. *Trans. Nonferrous Met. Soc. China*, **2016**, *26*, 974-983.
43. Rojas, H.; Molina, A.; Valdez, S.; Campillo, B. The impact of heat input on the microstructures, fatigue behaviors, and stress lives of TIG-welded 6061-T6 alloy joints. *Mater. Res. Express*, **2020**, *7*, 126512.
44. Bethea, J. F. Gas Tungsten Arc Welding of Aluminum Alloys with Nanocomposite 4943 Filler Material. UCLA, 2019.
45. Babu, N. K.; Talari, M. K.; Dayou, P.; Zheng, S.; Jun, W. Influence of titanium–boron additions on grain refinement of AA6082 gas tungsten arc welds. *Mater. Des.*, **2012**, *40*, 467-475.
46. Ericsson, M.; Sandström, R. Influence of welding speed on the fatigue of friction stir welds, and comparison with MIG and TIG. *Int. J. Fatigue*, **2003**, *25*, 1379-1387.
47. Dewan, M. W.; Wahab, M. A.; Okeil, A. M. Influence of weld defects and postweld heat treatment of gas tungsten arc-welded AA-6061-T651 aluminum alloy. *J. Manuf. Sci. Eng.*, **2015**, *137*, 051027.
48. Ambriz, R. R.; Mesmacque, G.; Ruiz, A.; Amrouche, A. Effect of the welding profile generated by the modified indirect electric arc technique on the fatigue behavior of 6061-T6 aluminum alloy. *Mater. Sci. Eng., A*, **2010**, *527*, 2057-2064.
49. Ambriz, R. R.; Barrera, G.; García, R.; López, V. H. The microstructure and mechanical strength of Al-6061-T6 GMA welds obtained with the modified indirect electric arc joint. *Mater. Des.*, **2010**, *31*, 2978-2986.
50. Haryadi, G. D.; Dewa, R. T.; Ekaputra, I. M. W.; Suprihanto, A. Investigation of post-weld heat treatment (T6) and welding orientation on the strength of TIG-welded AL6061. *Open Eng.*, **2020**, *10*, 753-761.

51. Dewan, M.; Liang, J.; Wahab, M.; Okeil, A. Post-weld residual stresses and heat treatments of gas tungsten arc welded aluminum alloy AA6061-T651. *WJE*, **2013**, *10*, 11-22.
52. Wang, B.; Xue, S.; Ma, C.; Wang, J.; Lin, Z. Effects of porosity, heat input and post-weld heat treatment on the microstructure and mechanical properties of TIG welded joints of AA6082-T6. *Metals*, **2017**, *7*, 463.
53. Ramaswamy, A.; Malarvizhi, S.; Balasubramanian, V. Post-weld heat treatment effects on the tensile properties of cold metal arc welded AA 6061-T6 aluminum joints. *Mater. Test.*, **2020**, *62*, 69-76.
54. Menzemer, C. C.; Hilty, E.; Morrison, S.; Minor, R.; Srivatsan, T. S. Influence of post weld heat treatment on strength of three aluminum alloys used in light poles. *Metals*, **2016**, *6*, 52.

## 5. Chapter 5: Comparison of Mechanical, Fatigue and Corrosion Properties of Fusion-Welded AA6011-T6 Plates Using Three Different Filler Wires

(internal review)

### Abstract

This study systematically examined the welding performance of three filler wires, ER4043, ER5356 and newly developed FMg0.6, in the gas metal arc welding of AA6011-T6 plates. An extensive analysis of the microstructure, mechanical properties, fatigue resistance, and corrosion behavior of AA6011 weldments was conducted. The ER4043 and FMg0.6 joints exhibited finer grain sizes in the fusion zone compared to ER5356 joint. The as-welded ER5356 and FMg0.6 joints exhibited elevated hardness and tensile strength compared to ER4043 joint. Notably, the fractures in the former two occurred within the heat affected zone, while the ER4043 joint experienced fractured within the FZ. The FMg0.6 joint demonstrated the highest overall strength among all joints with superior fatigue resistance in both as-welded and PWHT conditions. In the as-welded state, the ER5356 joint displayed the highest weight loss, whereas in the PWHT condition, it suffered the highest corrosion rate, attributed to the precipitation of  $\beta$ -Al<sub>2</sub>Mg<sub>3</sub> at the grain boundaries. The FMg0.6 joint, characterized by a high-volume fraction of eutectic Mg<sub>2</sub>Si in the as-welded state, exhibited a higher corrosion rate compared to ER4043 joint. However, the PWHT proved effective in enhancing corrosion resistance of the FMg0.6 joint. Given its highest tensile properties, superior fatigue properties and satisfactory corrosion resistance —particularly with PWHT— the newly developed FMg0.6 filler emerges as a promising candidate for welding high-strength 6xxx alloys.

**Keywords:** aluminum fusion welding; filler wires; microstructure; mechanical properties; fatigue resistance; corrosion behavior

## 5.1 Introduction

Aluminum alloys, particularly 6xxx series alloys like AA6061 and AA6011, play a pivotal role in diverse industries such as architecture, automotive, and transportation, owing to their high mechanical properties and resistance to corrosion. To ensure the widespread applicability of high-strength AA6xxx alloys, it is crucial to be easily weldable. Despite its susceptibility to hot cracking, this challenge can be effectively mitigated by incorporating ER5356 or ER4043 filler materials during fusion welding. The success of this mitigation strategy, however, hinges on meticulous welding design and the expertise of skilled personnel [1, 2]. Fusion welding remains as the predominant method for joining aluminum components, with conventional arc welding techniques, such as metal inert gas (MIG) welding and tungsten inert gas (TIG) welding [3].

The mechanical properties of the welded joints are influenced by several factors, including welding parameters, base metal (BM), and the type of filler wires. Among these factors, the filler type stands out as a predominant element in determining both the mechanical and the materials properties of joints. Commercial fillers such as ER4043 (Al–5Si) and ER5356 (Al–5Mg) are commonly employed to achieve satisfactory welding efficiency. The choice of ER4043 filler, for instance, induces changes in the chemistry of the melt pool, leading to a decrease in joint strength and an unfavorable color match for anodized applications. Conversely, when utilizing ER5356, there is a positive aspect in terms of anodization color matching. However, this advantage comes at the expense of the joint corrosion resistance, high-temperature stability, and weld pool fluidity [2, 4]. In the context of fillet weld, ER5356

emerges as a more suitable choice when compared to ER4043, primarily due to superior shear strength. Furthermore, ER4043 tends to exhibit enhanced weldability and a slightly reduced sensitivity to cracking, attributed to its higher Si content. Welds with ER4043 typically feature enhanced cosmetic appearance, smoother surfaces, reduced spatter, and less smut [5]. In a study by Naing et al. [6], it was observed that the repair joint formed with ER5356 filler exhibited higher tensile strength compared to the repair joint utilizing ER4043 filler. Recognizing the potential for enhancement, researchers have explored modifications to the chemical of these commercial fillers. Various attempts have been made to improve these fillers, and one notable approach involves incorporating ceramic nanoparticles into aluminum alloy filler materials. This modification aims to enhance mechanical properties and address welding issues like cracking [7]. However, in a study involving the addition of  $TiB_2$  nanoparticles into AA 4943 and utilizing TIG technique [8], the results indicated only marginal improvements in mechanical properties compared to standard filler.

Corrosion stands out as a critical concern, particularly in welded joints experienced a corrosive environment such as sea water, when it comes to aluminum and its alloys. The protective layer of  $Al_2O_3$ , with a micrometer-scale thickness on the surface, plays a crucial role in shielding the bulk alloys from extensive oxidation [9, 10]. Despite this protective measure, AA6xxx alloys are susceptible to localized corrosion attacks when exposed to aggressive environments. This vulnerability can be primarily attributed to the presence of Fe-rich intermetallics and the existence of  $Mg_2Si$  [11]. Zhang et al. [12] investigated the corrosion tendencies of AA6061-T6 joints produced through laser-arc hybrid welding were. Their results revealed that this welding led to the formation of dendritic structures in the fusion zone, accompanied by the segregation of alloying elements. Additionally, notable

occurrences of severe pitting occurred in the FZ, and intergranular cracking was observed in the HAZ. To enhance the corrosion resistance in welded joints, strategies involve reducing precipitate size, dissolving coarsened precipitates, or controlling precipitate size, location, and distribution [13]. Nam et al. [14] found surfaces with finer grains exhibited higher corrosion resistance, attributed to an increased formation of a passive protective film. In contrast, Osorio et al. [15] reported that coarse-grained regions might resist corrosion better due to fewer corrosion sites. By investigating the galvanic corrosion of laser-welded AA6061 aluminum alloy, Rahman et al. [16] reported that the cathodic process occurring at the FZ contributes to a high corrosion susceptibility. Yan et al. [10] conducted the potentiodynamic polarization tests on the welded AA6061 using ER4043 and ER5356 fillers. Their findings indicated that the corrosion current density of the ER4043 joints was slightly higher than that of the ER5356 joints.

The corrosion susceptibility of heat-treatable aluminum alloys can be attributed to the precipitation of different phases, which affects chemical activity. This susceptibility is further influenced by the factors such as composition, heat treatment, grain characteristics, precipitate distribution, environmental conditions, and applied loading [13, 17]. The application of post weld heat treatment (PWHT) stands as an effective method for improving both the mechanical and chemical characteristics of the fusion-welded joints. This is achieved by reducing residual stresses and modifying the microstructure of heat-treatable aluminum alloys [18]. In multi-pass welding, the high heat input gradually degrades the microstructure in the HAZ, exposing the welded area to temperatures in the solution treatment and overaging range. This demands the necessity of applying PWHT to mitigate the cumulative impacts of these thermal cycles [2, 19].

The objective of this study was to conduct a comprehensive investigation of the welding performance high-strength AA6011-T6 thick plates using the commercial fillers of ER4043 and ER5356, and the newly developed FMg0.6 filler. The investigation encompassed assessing tensile properties and the fatigue characteristics of the welded joints in both their as welded and in PWHT conditions. Furthermore, corrosion resistance was evaluated for the BM, HAZ, and all FZs. The aim was to elucidate the chemical attributes of the joints and provide a comprehensive analysis with relevance to industrial applications.

## 5.2 Experimental Procedure

Wrought 6011-T6 aluminum plates of 500 mm x 75 mm x 6 mm were produced by DC casting and extrusion and used as a BM. The BM was cast at 730 °C followed by homogenization at 560 °C for 3hr. Then it was extruded at 500 °C with water rinsing at the exist. After that, the extruded plates were naturally aged at RT followed by aging at 177 °C for 8 hr. They were then heat-treated to T6 and used as BM. The plates were welded using the MIG technique. The extruded plates were welded using the MIG technique using two commercial filler wires, ER4043 and ER5356, and a novel filler named FMg0.6. Table 5.1 presents the chemical composition of the BM and three filler wires. The production route of the filler wires was detailed in our previous paper [20]. The welding was performed using a Fronius Transpulse Synergic 5000-CMT mounted on a Motoman UP50N robot. Before welding, the plates were prepared by cutting then cleaning with acetone, followed by clamping in a butt joint configuration with a single V groove. To fill the groove space between two sheets with the filler wire, the welding process involved two passes with specific parameters listed in Table 5.2. After welding, the post-weld heat treatment (T6) was applied for a part of samples, consisting of a solution treatment at 550°C for 1 hour followed

by water quenching, and subsequently natural aging for 24 hours, followed by artificial aging at 180°C for 8 hours. This heat treatment was optimized to restore the mechanical properties lost during the welding process and regain the original strength of the BM in T6 condition prior to welding.

After welding, an X-ray radiography test (XRT) was performed. Tensile and fatigue samples were selected from low porosity zones (less than 1%) to minimize its effect on properties. Microstructure was examined optical microscopy (OM) and scanning electron microscopy (SEM). Microhardness profiles were measured using an NG-1000 CCD microhardness tester, applying a 50-gram load with a 20-second dwell time. The HV profiles were performed 1 mm from the root side (first pass) and at 1 mm from the cap side (second pass). Tensile and high cyclic fatigue tests were conducted on Instron 8801 servo-hydraulic machine, both in as-welded and PWHT conditions. The tensile test was performed at a crosshead speed of 1 mm/min and room temperature, using standard subsized samples. Fatigue tests were carried out at ambient temperature, applying a sinusoidal waveform with a frequency of 30 Hz and a cyclic stress ratio of 0.1. The tensile and fatigue samples were machined according to ASTM E8-04 and ASTM E466-96, respectively, as shown in Figure 5.1. The fatigue S-N curves were plotted using the ISO 12107:2003 statistical approach. As aluminum alloys typically lack a fatigue limit, the fatigue tests were halted after  $10^7$  cycles.

The Potentiodynamic polarization (PD) test was conducted at ambient temperature utilizing the Flat Cell Kit, with a naturally aerated 3.5% NaCl solution (w/w) serving as the electrolyte. A three-electrode system was utilized, comprising a mesh platinum counter electrode, a saturated Ag/AgCl reference electrode, and the cold-mounted samples as the working electrode. The FZs were cut alone and separated from the HAZ by cutting at the

fusion line. The whole FZ (both passes) was taken as one working electrode. The HAZ was taken with length of 10 mm from the fusion line and width as the BM thickness (6 mm). The BM samples were cut from cross-section of the unwelded plates with the same area as the HAZ (10 x 6 mm<sup>2</sup>). The BM, HAZ, and the FZs in both AW and PWHT conditions underwent cold mounting and polishing, followed by a 2-minute cleaning with acetone and methanol to remove any grease or atmospheric dust prior to initiating the PD test. The values of the current were normalized with the actual surface area of the electrode to calculate the current density for each electrode. The PD measurements were conducted after stabilization the open-circuit potential (OCP) of the working electrodes in the solution of 3.5% wt. NaCl for 1 hour. PD measurements were carried out with a sweeping rate of 1 mV/s, ranging from an initial potential of -1175 mV to 200 mV versus the reference electrode. The measured current density in the PD test was used to compute the corrosion rate with Eq. (1) according to ASTM G102.

$$Corrosion\ rate = 3.27 \times \frac{i_{corr} \times EW}{\rho} \left( \frac{\mu m}{year} \right) \quad (1)$$

Where  $i_{corr}$  is the corrosion current density, EW and  $\rho$  are the equivalent weight and density of Al, respectively.

The BM, HAZ, and the FZs in AW and PWHT conditions were cold mounted then polished. Then the samples were cleaned with acetone and methanol for 2 minutes to fully clean from any grease or atmospheric dust before starting the test. The immersion test was performed based on GBT19746-2005 standard using test specimens of the size of 50 mm × 10 mm × 5 mm with keeping the FZ in the middle of the sample length for the welded joints as shown in Figure 5.2(a). The specimens were mechanically ground with SiC papers (240 to 1200

mesh) and cleaned with pure alcohol. They were then weighed precisely using an electronic balance ( $\pm 0.01$  mg) before being immersed in a naturally aerated 3.5% NaCl solution, placed about 30 mm below the liquid level in glass jars (see Figure 5.2 (b)). To remove corrosion products, the samples were treated with a chromic acid solution at 80°C, following the GBT 16545-1996 standard. The mass loss test was conducted on three samples simultaneously, and the result was the average value [21].

Table 5.1: Chemical compositions of BM and three filler wires (wt.%).

	Si	Mg	Mn	Fe	Cu
<b>BM (6011)</b>	0.92	0.75	0.45	0.17	0.64
<b>ER 4043</b>	4.97	0.024	0.02	0.16	-
<b>ER 5356</b>	0.06	5	0.1	0.15	0.01
<b>FMg0.6</b>	6.23	0.6	0.23	0.14	0.011

Table 5.2: The welding parameters used.

	Current (Amp.)		Voltage (V)		Travel speed (m/min)		Wire feed speed (m/min)	
	Pass 1	Pass 2	Pass 1	Pass 2	Pass 1	Pass 2	Pass 1	Pass 2
<b>5356</b>	132	87	18.8	17.2	0.5	0.27	5	3.2
<b>ER4043 &amp; FMg0.6</b>	163 $\pm$ 4	110 $\pm$ 5	21.5 $\pm$ 0.5	22 $\pm$ 0.7	0.5	0.27	4.5 $\pm$ 0.3	3.2

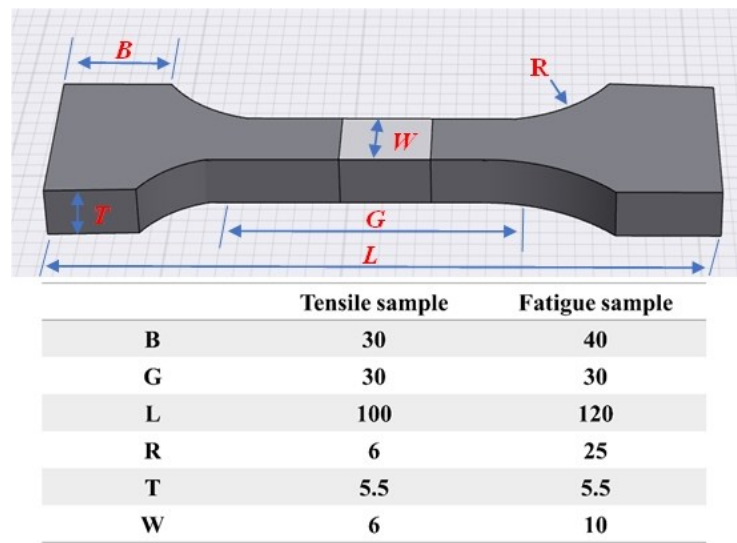


Figure 5.1. Dimensions of the tensile and fatigue samples in mm.

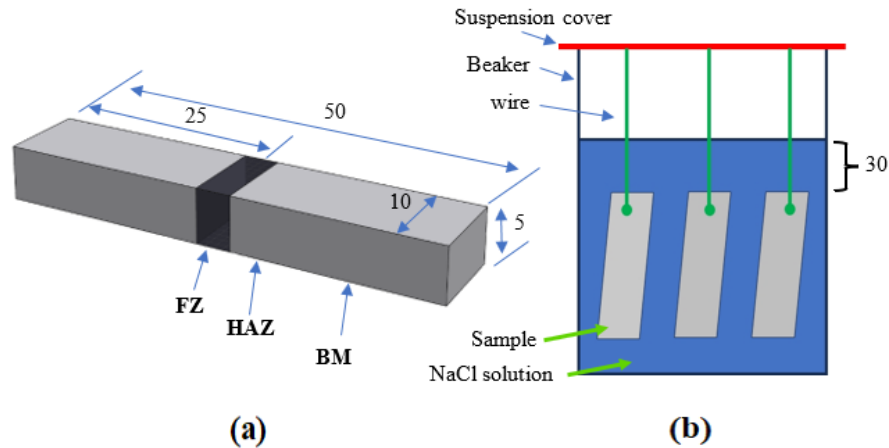


Figure 5.2. Schematic drawing of the immersion test, (a) sample dimensions, and (b) the test set up. All dimensions are in mm.

## 5.3 Results and discussion

### 5.3.1 Microstructure of the Joint

Figure 5.3 illustrates the grain morphologies analyzed using OM under polarized light in the BM, HAZ and FZ. The BM shows elongated grains in the direction of the extrusion with an average size of  $106.8 \mu\text{m}$  (Figure 5.3(a)). Between the HAZ and FZ there was a recrystallized zone (RZ) in the side of HAZ, and its width was influenced by the heat input from the welding arc. Typically, the region after the RZ experiences partial recrystallization zone due to the temperature gradient with smaller grain size than that of the BM [22]. In 4xxx filler joints, the width of the RZ was approximately  $407 \mu\text{m}$ , which is wider than that of ER5356 joints ( $346 \mu\text{m}$ , Figure 5.3(b) and (c)). This change in the RZ is attributed to the higher welding current in both passes used in the 4xxx fillers than that used in the ER5356 filler, as indicated in Table 5.2. The RZs in ER5356 and the 4xxx fillers displayed similar grain sizes,  $16.5 \pm 2$  and  $14.7 \pm 3 \mu\text{m}$ , respectively, due to fast cooling rate [23, 24]. In the

FZ of ER5356 joint (Figure 5.3(d) and (e)), the grain size in the first pass was  $219.6 \pm 28 \mu\text{m}$ , which were significantly smaller than that in the second pass ( $410.2 \pm 44 \mu\text{m}$ ). This difference is ascribed to the greater heat input (132 Amp) and a faster cooling rate during the first pass, in contrast to the relatively lower heat input in the second pass (87 Amp) and slower cooling rate in the second pass [25, 26]. Similarly, in the FZs of 4xxx filler joints ((Figure 5.3(f) and (g)), the grain size in the first pass was smaller than that of the second pass ( $231.8 \pm 35 \mu\text{m}$  vs  $347.79 \pm 49 \mu\text{m}$ ) due to the differences in the heat input and cooling rate. The grain morphology between the two passes showed epitaxial grain growth, illustrated in Figure 5.3(h). For the porosity, the average equivalent pore diameter in the first pass was almost similar in all filler joints,  $54 \pm 8 \mu\text{m}$ . In the second pass, ER4043 and FMg0.6 filler joints had smaller pore size than that of ER5356 joint ( $63 \pm 17 \mu\text{m}$  vs  $103 \pm 21 \mu\text{m}$ ). This behavior is attributed to that the high cooling rate in the 4xxx filler joints gives rise of producing smaller pore size, while the low cooling rate in ER5356 joint produced larger pores according to [27].

The microstructures of the BM and FZs under as welded condition are shown in Figure 5.4. BM microstructure contains  $\alpha\text{-Al(FeMn)Si}$ ,  $\text{Mg}_2\text{Si}$ , and  $\text{Q-AlMgSiCu}$  intermetallic phases. Due to the extrusion process, the Fe-rich  $\alpha\text{-Al(FeMn)Si}$  was oriented in the extrusion direction (Figure 5.4(a) and (b)). The microstructure of the ER5356 joint consists of  $\beta\text{-Al}_2\text{Mg}_3$  and  $\text{Mg}_2\text{Si}$  phases (Figure 5.4(c)) [28, 29]. The ER5356 filler has no Si in its composition, and however, few granular  $\text{Mg}_2\text{Si}$  particles were formed due to the diffusion of Si from the BM dilution [30]. The main phases in ER4043 joint are eutectic Si, Fe-rich intermetallics, and  $\text{Mg}_2\text{Si}$  (Figure 5.4(d)). It can be observed that the Fe-rich intermetallics have two forms, namely the platelet-like  $\beta\text{-AlFeSi}$  and the less harmful  $\alpha\text{-Al(FeMn)Si}$ .

FMg0.6 joint has similar phase types as the ER4043 joint ((Figure 5.4(e)). However, the volume fraction of  $Mg_2Si$  in FMg0.6 joint is higher relative to ER4043 joint ( $0.75 \pm 0.21\%$  vs  $0.15 \pm 0.08\%$ ). Similar trend was observed in the volume fraction of  $\alpha-Al(FeMn)Si$ ,  $1.68 \pm 0.32\%$  and  $0.88 \pm 0.24\%$  for FMg0.6 and ER4043 joints, respectively, due to the addition of 0.25% Mn in FMg0.6 filler (see Table 5.1), which modified the harmful  $\beta$ -Fe intermetallic to less harmful  $\alpha$ -Fe intermetallic, as shown in Figure 5.4 (e) [31].

The microstructures of the FZs after PWHT are shown in Figure 5.4(f-h). The ER5356 joint shows the formation of  $\beta-Al_2Mg_3$  at the grain boundaries and some dispersed within the grains Figure 5.4(f) [32, 33]. Since the 5xxx alloy is not heat-treatable, performing the PWHT can homogenize the matrix microstructure leading to better mechanical properties as depicted in the following sections [33]. In the 4xxx filler joints Figure 5.4(g) and (h)), the PWHT shows a significant effect on the matrix. All the  $Mg_2Si$  phases in both joints 6 were completely dissolved in the microstructure. Moreover, the eutectic Si morphology was transformed from fibrous structure in the as welded condition to spheroid morphology [30]. The Fe-rich intermetallics experienced partial fragmentation [34-36].

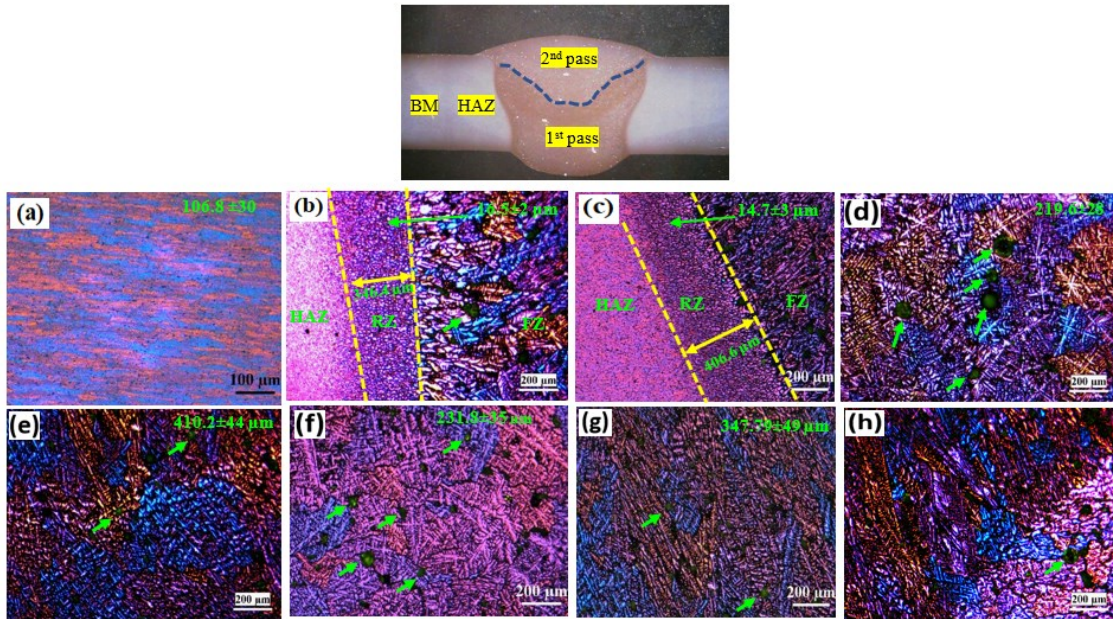


Figure 5.3. Grain morphologies of the different zones under as welded condition. FMg0.6: (a) BM, (b) and (c) recrystallized zones (RZ) in ER5356 and ER4043 joints, respectively; (d) and (e) the FZs in the 1<sup>st</sup> and 2<sup>nd</sup> passes in ER5356 joint, respectively; (f) and (g) the FZs in the 1<sup>st</sup> and 2<sup>nd</sup> passes in FMg0.6 joints, respectively; (h) the boundary between the 1<sup>st</sup> and the 2<sup>nd</sup> passes in ER4043 joints. The green arrows point to the porosity.

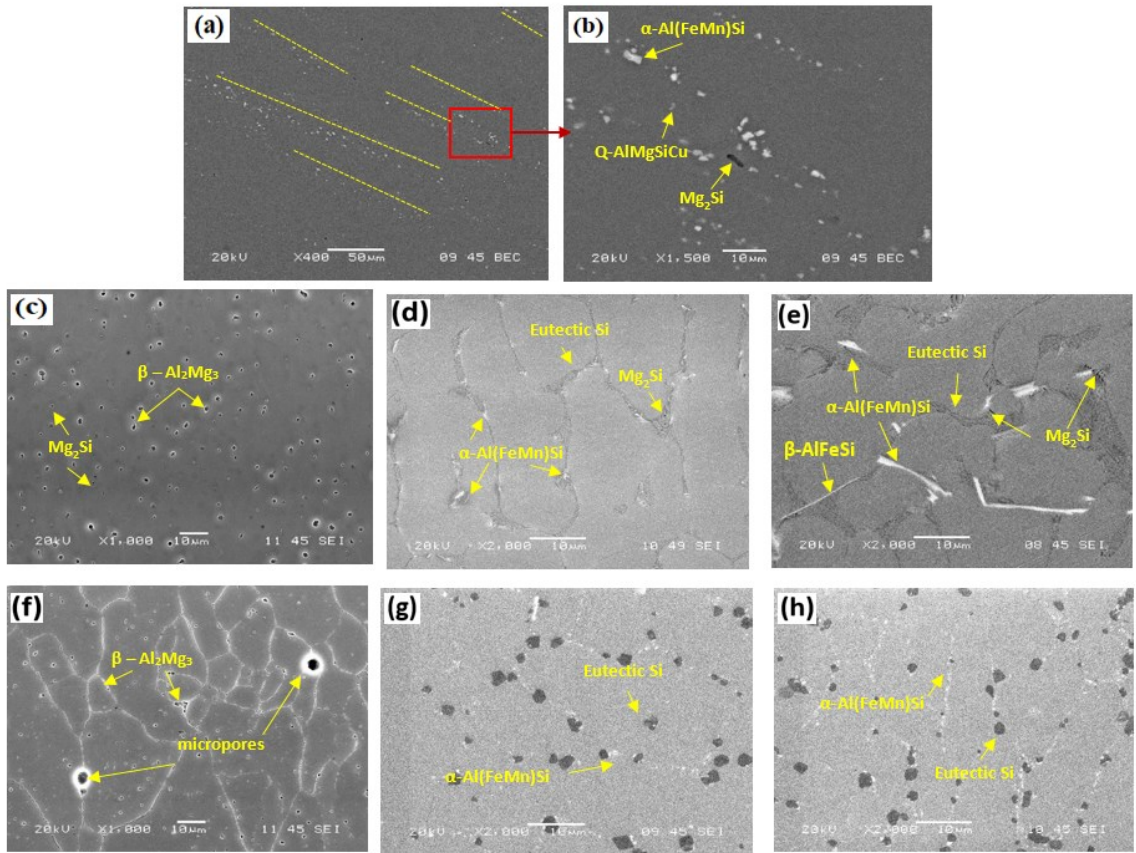


Figure 5.4. (a) and (b) microstructure of the BM. (c), (d), and (e) microstructures of the 2<sup>nd</sup> pass of ER5356, ER4043, and FMg0.6 joints under the as welded condition, respectively. (f), (g) and (h) microstructures of the 2<sup>nd</sup> pass of the ER5356, ER4043, and FMg0.6 joints after PWHT, respectively. All phases were identified with the SEM-EDX.

### 5.3.2 Microhardness

The microhardness profiles of the three filler joints under as welded condition are illustrated in Figure 5.5(a) and (b). The highest HV was observed in the BM,  $145 \pm 3$  HV. The HAZ between the FZ and BM exhibited the softest region with approximately 74 HV. This softening result is due to an overaging induced by the heat input from the welding arc [37, 38]. With movement from the HAZ (the softest zone) to the FZ, the HV gradually increased due to dissolution of the original  $\beta''$ -Mg<sub>2</sub>Si precipitates in BM, leading to solution

strengthening. In contrast, the HV from the BM to the softest zone depicts decreasing due to enhancing the effect of the welding heat on the dissolution of  $\beta''$ -Mg<sub>2</sub>Si precipitates [20]. The HVs in the FZ of the first pass of the ER4043 joint and in both passes of ER5356 joints show similar values,  $78 \pm 3$  HV, whereas the HV in the FZ of FMg0.6 joint depicts an increase in the hardness value,  $88 \pm 2$  HV. The similarity in HV of both passes of ER5356 is attributed to the limited solubility of the Mg in the matrix at room temperature. According to Pozank et al. [39], the solubility of Mg in FCC-Al is less than 1 wt.% leading to the same Mg content in the matrix of the both passes. The second passes of ER5356 and FMg0.6 joints depicts slight difference in HV values of  $85 \pm 5$  and  $89.2 \pm 4$  HV, respectively, as shown in Figure 5.5(b). The HV of ER4043 has the lowest value in the second pass,  $66 \pm 2$  HV, due to the low Mg in the filler and low BM HV dilution [38]. The higher HV in FMg0.6 joint in all passes can be attributed to the added Mg (0.6%) in its composition.

The HV profiles of all joints after PWHT are shown in Figure 5.5(c) and (d). The HV results in ER4043 joint exhibited large variation between the two passes. The first pass displayed a greater HV value compared to the second pass ( $135 \pm 3$  vs  $100 \pm 5$  HV). This discrepancy can be attributed to the increased BM dilution in the first pass in comparison to the second pass, resulting in a higher concentration of precipitates in the first pass. The ER5356 filler shows similar HV in both passes,  $100 \pm 3$  HV, due to the limitation of Mg solubility as the same in the as welded case. It is worth to mention that the HV of ER5356 is higher than that of the as welded condition ( $80 \pm 5$  HV) due to the applied heat treatment, which leads to homogenize the microstructure and reduce the residual stress came from the welding process [29]. Furthermore, the addition of few Si contents in both passes from the BM dilution leads to formation Mg<sub>2</sub>Si precipitates during PWHT [40-42]. The newly developed filler, FMg0.6,

shows the highest HV with  $145 \pm 2$  HV compared to two commercial fillers. The high HV in FMg0.6 joint is attributed to the high Mg content in its composition, which leads to sufficient precipitation of coherent nanosized  $\beta''$  precipitates as explained in our previous works [20, 30]. With applying PWHT, the HAZ disappeared in all joints, which led to retrieving all precipitates and hence the mechanical properties.

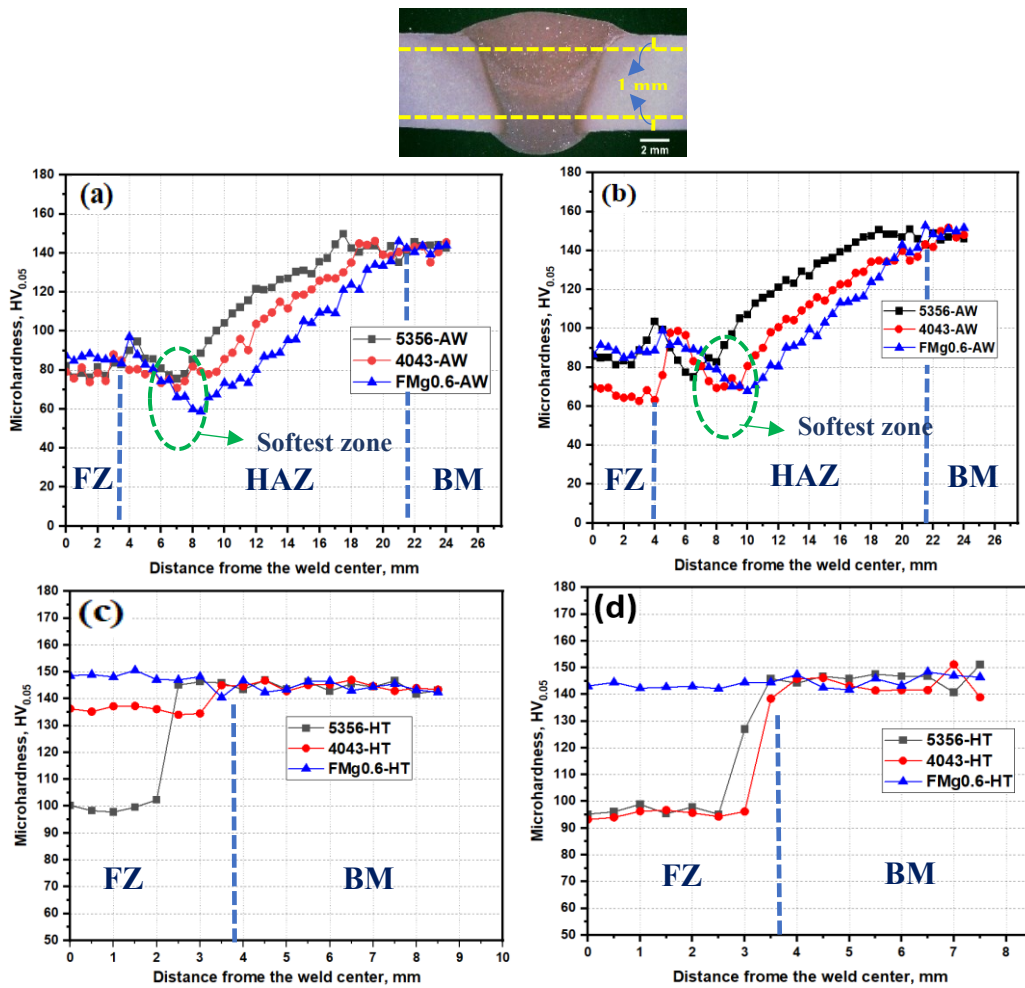


Figure 5.5. Microhardness profiles, (a) and (b) for as welded condition in the first and second passes. (c) and (d) after PWHT in the first and second passes.

### 5.3.3 The tensile Properties

Figure 5.6(a) shows the tensile properties of the as welded joints. The BM depicts the highest ultimate tensile strength (UTS) and yield strength (YS) of  $437 \pm 6$  and  $397 \pm 10$  Mpa, respectively. The ER5356 and FMg0.6 joints exhibited similar values of UTS and YS, measuring  $240 \pm 2$  and  $148 \pm 5$  MPa, respectively. This similarity occurs because the HAZ represents the softest zone in both joints and has the lowest HV (Figure 5.5(a)), where the fracture occurs in the tensile sample (see the insets in Figure 5.6(a)). The ER4043 joint shows the lowest UTS and YS,  $230 \pm 7$  and  $135 \pm 5$  Mpa, respectively, and the fracture occurred in the FZ. This result is consistent with the HV result since the FZ of ER4043 exhibited the lowest HV in the second pass (Figure 5.5(b)) due to less dilution from the BM and no Mg in ER4043 filler composition. Although the grain sizes in each pass of ER4043 and FMg0.6 are in the same range (see Figure 5.3), the tensile strength of FMg0.6 joint is higher compared to ER4043 due to the added Mg in the filler, which increases the solution strengthening of the joint [20, 30]. The elongation of the BM has the highest value of  $23 \pm 3\%$ . All three joints show lower elongation due to the inhomogeneous microstructures such as coarse equiaxed and columnar grains at the center and the fusion line, as well as the porosity in the FZs (Figure 5.3). ER4043 has the lowest elongation of  $10 \pm 0.8\%$  amount all three joints, while both ER5356 and FMg0.6 joints exhibit the similar elongation, approximately 12.

The tensile properties of the PWHTed joints are shown in Figure 5.6(b). The ER4043 joint has UTS and YS of  $335 \pm 12$  and  $282 \pm 8$  MPa, respectively, which is higher than that in the as welded condition because of formation of some nanosized  $\beta''$ -Mg<sub>2</sub>Si precipitates originated from the BM dilution [20, 38]. ER5356 joint exhibits the lowest UTS and YS of

305 ± 12 and 250 ± 8 MPa in PWHT condition. This is a result of the adverse influence of the brittle Al<sub>3</sub>Mg<sub>2</sub> phase at the grain boundaries (Figure 5.4(f)) [10]. However, the strength of ER5356 joint surpasses the strength in the as-welded condition. This enhancement in strength is ascribed to the homogenization effect of the heat treatment and the potential formation of a few β''-Mg<sub>2</sub>Si precipitates due to silicon diffusion from the BM dilution [41, 42]. The highest strength in the welded joints was observed in FMg0.6 joint with UTS and YS of 410 ± 6 and 387 ± 6 MPa, respectively. This high strength of FMg0.6 joint was achieved via the precipitation of a high number β''-Mg<sub>2</sub>Si precipitates after PWHT as reported in our previous works [20, 30, 36]. It is worth mentioning that the dilution in the 2<sup>nd</sup> pass is low due to the geometry of the groove and using thick BM. The role of the high Mg in FMg0.6 filler compensates the decrease in the dilution, and supports the FZ in FMg0.6 joint with enough Mg content to make it efficient in T6 aging treatment [43, 44]. ER4043 depicts the highest elongation of 8.7 ± 0.8 % among all welded joints. The elongations of the FMg0.6 and ER5356 joints are 6.8 ± 1 % and 5.7 ± 1.5 %. Respectively, showing reduction in elongation relative to ER4043. The precipitation of the brittle β-Al<sub>3</sub>Mg<sub>2</sub> in ER5356 joint (Figure 5.4(f)) and the formation of micropores near these precipitates result in a premature material fracture and reduction in the elongation as reported by Wen et al. [45].

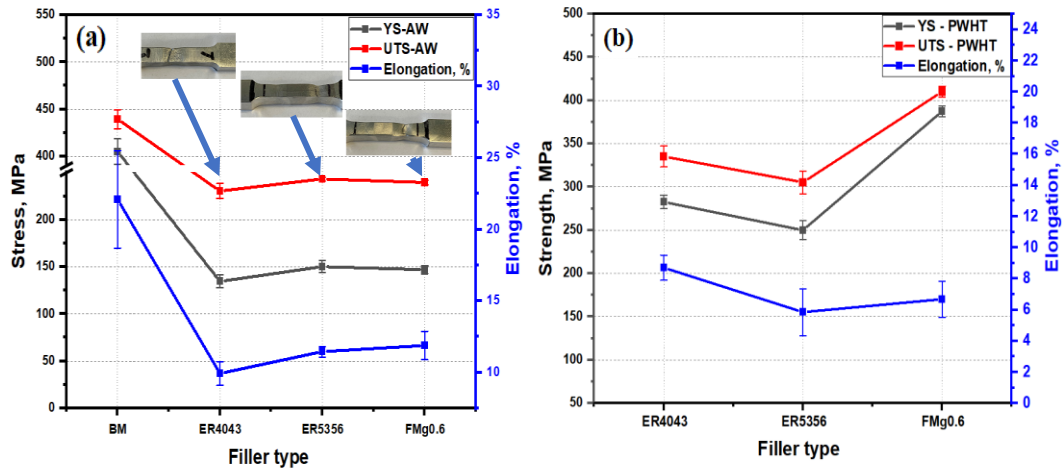


Figure 5.6. The tensile properties of the joints: (a) in the as welded condition, and the insets showing the typical fractures occurred in the tensile sample; (b) in the PWHT condition.

### 5.3.4 Fatigue Properties of the Joint

The fatigue properties in the as welded condition are shown in Figure 5.7(a). The BM represents the highest fatigue strength compared to the welded joints due to very low flaws and microdefects in the matrix [38]. It is common in metallic alloys that the higher tensile strength improves cyclic performance and fatigue behavior of materials, assuming a good surface condition and less influence from microdefects [10, 30]. Fractures during tensile testing are found in different zones for ER4043, ER5356, and FMg0.6 joints, however, fatigue failures consistently occur in the FZ for all joints due to the presence of welding defects such as micropores and coarse grains. ER5356 joint represents the lowest fatigue strength due to the high porosity size compared to ER4043 and FMg0.6 joints (Figure 5.3), as confirmed by Yan et al. [10]. FMg0.6 joint shows the highest fatigue strength compared to two commercial fillers. Thus the order of the fatigue strength can be defined as  $FMg0.6 > ER4043 > ER5356$ . The higher fatigue properties in FMg0.6 relative to ER4043 joint is

related to the hindering effect of the dislocation motion by the Mg solute atoms in the Al matrix during the cyclic loading as reported in our previous work [30].

Figure 5.7(b) depicts the fatigue properties of the PWHTed joints. The fatigue strengths of the PWHTed samples were improved significantly relative to the as welded joints (Figure 5.7 (a)), as also confirmed by Perez et al. [38]. The order of the fatigue strength after PWHT is the same as in the as welded condition: FMg0.6 > ER40433 > ER5356. The fatigue strengths in the heat-treated ER4043 and FMg0.6 joints were enhanced due to the strengthening effect of  $\beta''$ -Mg<sub>2</sub>Si precipitates. Increasing the Mg in FMg0.6 joint results in a higher density of  $\beta''$ -Mg<sub>2</sub>Si precipitates compared to ER4043, hence contributing a higher fatigue strength [36]. Nanosized  $\beta''$  precipitates contribute to high fatigue strength through two mechanisms. Firstly, they serve as barriers to dislocation movement during cyclic loading, resulting in the shearing of these precipitates. This impediment prevents dislocations from accumulating and forming microvoids at grain boundaries [38, 46]. Secondly, when a dislocation reaches the crack tip, it can enlarge the crack size by one Burgers vector. Slowing down dislocation motion prolongs the time it takes for dislocations to reach the tip, consequently leading to a higher fatigue life [30]. In ER5356 joint, due to the homogenization effect of the heat treatment, the fatigue strength was enhanced compared to the as welded condition, and however, its values were still lower compared to the heat-treated ER4043 and FMg0.6 joints, which is probably attributed to the precipitation of the brittle  $\beta$ -Al<sub>3</sub>Mg<sub>2</sub> phase at grain boundaries and [18] and fewer  $\beta''$ -Mg<sub>2</sub>Si precipitates in the matrix due to lack of Si solutes.

The fatigue fracture surfaces of the PWHTed joints are shown in Figure 5.8. The fatigue fracture normally consists of three zones: the initiation zone, the propagation zone, and the

final fracture zone. For all joints, the initiation zone locates the surface or near surface porosity Figure 5.8(a), (d) and (g)), as reported by many researchers [10, 18, 47]. The propagation zone starts directly from the initiation zone (pores) and ends when the total crack length reaches the critical size as indicated by the yellow dashed lines, where the final fracture zone continues up to the end of the sample. The striation width was measured at 1 mm from the initiation zone in all welded joints, which represents the incremental increase in the fatigue crack with each cyclic loading, referring to the fatigue crack propagation rates. the striation widths were measured to be  $431\pm 27$ ,  $573\pm 63$ , and  $715\pm 51$  nm for the FMg0.6, ER4043, and ER5356 joints, respectively. Therefore, the fatigue crack propagation rates remarkably increased from FMg0.6 via ER4043 to ER5356 joints. The newly developed filler, FMg0.6 joint, exhibits the lowest fatigue crack propagation rate, which gives the highest fatigue life as result of the modification its composition with the addition of Mg in the filler. ER5356 joint depicts highest crack propagation rate because few precipitates can retard the dislocation motion, just the Mg solutes can do it. When the propagation zone is finished, the remaining part of the fatigue sample cannot endure cyclic loads, leading to a normal fracture resembling that of a tensile test when the UTS is surpassed. The final fracture zone of ER4043 joint shows larger dimples compared to that of FMg0.6 joint due to low Mg content in ER4043 filler. At the bottom of all dimples in ER4043 and FMg0.6 joints, fractured Si particles were observed, indicating the mechanism of dimples formation due to brittle Si particles. The final fracture zone of ER5356 joint shows smaller size and more shallow dimples compared to E4043 joint due to the existence of  $\beta$ - $\text{Al}_2\text{Mg}_3$  particles [48].

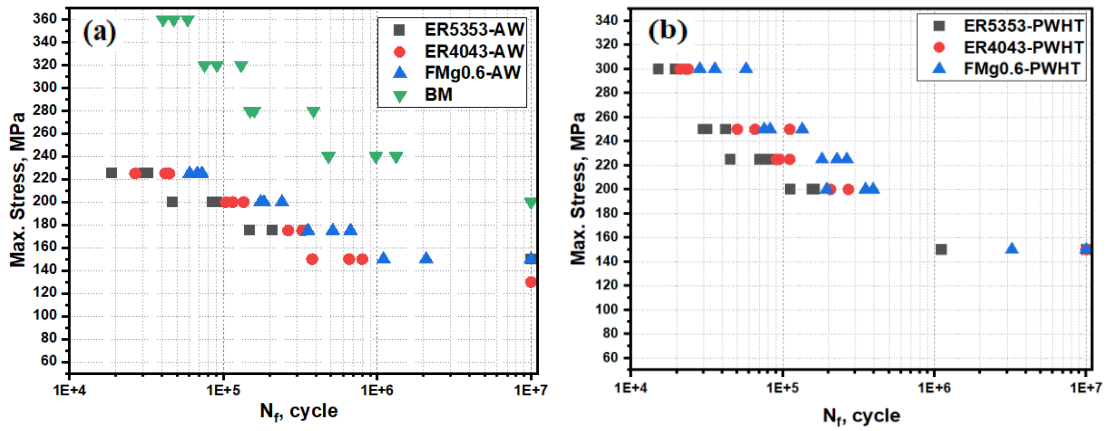


Figure 5.7. The S-N curves of the welded joints, (a) in as welded condition, and (b) in the PWHT conditions.

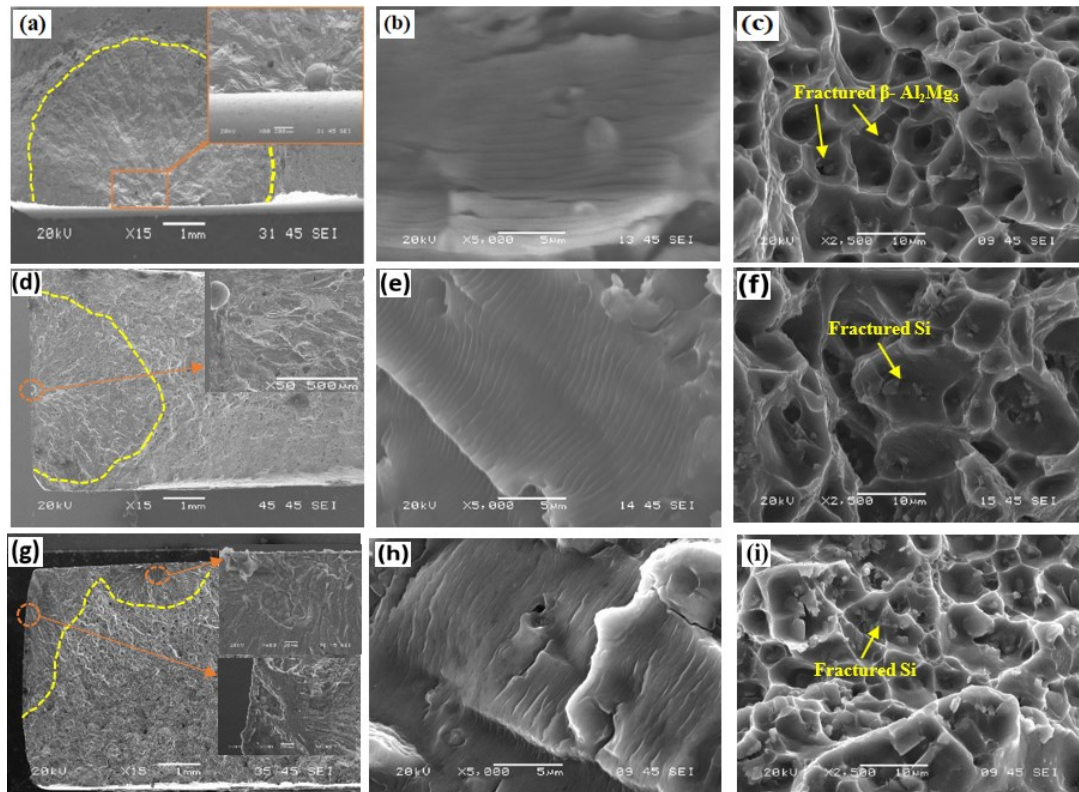
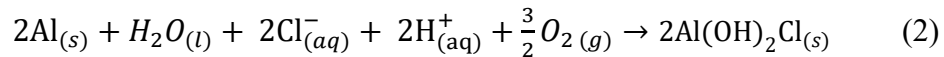


Figure 5.8. Fatigue fractures in the PWHT condition: (a), (b) and (c) the initiation, propagation, and final zones of ER5356 joint. (d), (e) and (f) the initiation, propagation, and final zones of ER4043 joint; (g), (h) and (i) the initiation, propagation, and final zones of FMg0.6 joint.

### 5.3.5 Corrosion Resistance of the Joint

#### 5.3.5.1 Potentiodynamic polarization

Figure 5.9(a) displays the typical potentiodynamic polarization (PD) curves of the BM and the as welded joints. All corrosion parameters are summarized in Table 5.3 for both as welded and PWHT conditions. The corrosion parameters were measured by Tafel extrapolation method according to ASTM G59-97 as shown in Figure 5.9 (c). The corrosion mechanism of aluminum in the salty and naturally aerated environment primarily involves the anodic dissolution of aluminum and the cathodic reduction of oxygen. The overall reaction can be expressed by Eq. (2) [49, 50]:



The anodic polarization branch of the curves (from the corrosion potential,  $E_{corr}$ , and moving in the positive direction) have similar behavior indicating the same mechanism of corrosion in the salty medium. The BM shows the highest  $E_{corr}$  of -602.9 mV, and the lowest corrosion rate of 24.25  $\mu\text{m}/\text{Y}$ , representing the highest corrosion resistance compared to the welded joints. The HAZ exhibits a diminished corrosion resistance relative to the BM with a corrosion rate of 113.5  $\mu\text{m}/\text{year}$ . This reduction in the corrosion resistance is caused by many small grains in the RZ and the partially recrystallized part of the HAZ (Figure 5.3(b) and (c)), which increase the grain boundary area and hence the susceptibility to intergranular corrosion (IGC) [51]. The ER5356 joint depicts the lowest  $E_{corr}$  of -666.7 mV and the highest corrosion rate of 167.18  $\mu\text{m}/\text{Y}$ . Excessive Mg content in ER5356 joint leads to reduce the corrosion resistance because of the low reduction potential of Mg relative to the that of Al [52, 53]. FMg0.6 joint shows higher corrosion rate compared to ER4043 joint

(99.45 vs 78.33  $\mu\text{m}/\text{Y}$ ). This is attributed to the high contents of eutectic  $\text{Mg}_2\text{Si}$  and Fe-rich intermetallics in FMg0.6 joint relative to ER4043 joint (Figure 5.4(d) and (e)). The eutectic  $\text{Mg}_2\text{Si}$  and Fe-rich intermetallic particles act as anodes and cathodes, respectively, relative to the matrix leading to more corrosion with high contents of such phases [16, 18, 53].

The PD curves of the PWHTed samples are shown in Figure 5.9 (b). The anodic and cathodic reactions are the same in the as welded condition. All corrosion parameters are summarized in Table 5.3 for both as welded and PWHT conditions. ER5356 joints exhibits the lowest corrosion resistance with  $E_{\text{corr}}$  of -680.36 mV and the corrosion rate of 178.76  $\mu\text{m}/\text{Y}$ . This occurs due to the formation of the anodic susceptibility of  $\beta\text{-A}_3\text{Mg}_2$  at the grain boundaries and its sensitization effect [32, 33, 54]. It can be observed that the PWHT leads to increase the corrosion resistance relative to the as welded condition in both ER4043 and FMg0.6 joints (Table 5.3). This behavior is due to the dissolution the eutectic  $\text{Mg}_2\text{Si}$  and the partial fragmentation of the Fe-rich intermetallics in the matrix (Figure 5.4(g) and (f)) [55]. The ER4043 and FMg0.6 joints show slight difference in the corrosion rates (60 vs 53  $\mu\text{m}/\text{Y}$ ), which are lower than those on the as welded condition by 23% and 46.8 %, respectively. Overall, the joint with the newly developed FMg0.6 demonstrates excellent corrosion resistance similar to the commercial ER4043.

### 5.3.5.2 Surface morphologies of the corrosion tested samples

Figure 5.10(a-d) shows the macroscopic images of corroded surfaces of the BM and as welded joints after performing the PD tests. The BM has the lowest content of pits compared to the welded joints (Figure 5.10(a)). The HAZ exhibits a great number of pits in contrast to the BM (Figure 5.10(e)) because of its smaller grain size relative to that of the BM and elevated presence of grain boundaries hosting both anodic and cathodic phases [9]. The 2<sup>nd</sup> passes of the ER4043 and FMg0.6 joints were selected to show the significant differences between both in Figure 5.10(b) and (c). ER4043 joint has a lower number of pits than FMg0.6 joint due to lower content of eutectic Mg<sub>2</sub>Si. ER5356 joint suffers from the worst pitting corrosion because the high Mg content in the matrix leads to more dissociation of the Mg in the solution. Furthermore, the dispersed  $\beta$ -Al<sub>2</sub>Mg<sub>3</sub> phase in the as welded condition acts as anodes, promoting the pit formation in the FZ (Figure 5.4(a)). Additionally, the 1st pass of ER5356 joint has less Mg content relative to the 2<sup>nd</sup> pass due to the high dilution. This difference in the Mg leads to significant difference in the potential of each pass. Therefore, much more pits in the 2nd pass are found and the most severe material loss is observed in the boundary (Figure 5.4(d)) [16, 54].

The macro views of the PWHTed joints after the PD tests are shown in Figure 5.10 (f-h). The pit contents are reduced in ER4043 and FMg0.6 joints compared to that in the as welded condition. This is because of reducing the anodic acting phases in the matrix, such as the eutectic Mg<sub>2</sub>Si and modifying the spheroid Si particles as well as the partial fragmentation of the Fe-rich intermetallics (see Figure 5.4(c) and (f)) [56]. ER5356 joint shows more severe and higher pit contents in both passes relative to the as welded condition due to dispersion of the anodic behaved  $\beta$ -Al<sub>2</sub>Mg<sub>3</sub> at the grain boundaries and within the grains (Figure 5.4(d)).

Figure 5.11 illustrates in detailed pitting corrosion in both as welded and PWHTed joints. The BM pits are elongated in the extrusion direction ( Figure 5.11(a) ) due to distribution of the intermetallics in the extrusion direction (Figure 5.4(a)) [57]. The intermetallics, such as Q-AlMgSiCu and the Fe-rich phases act as cathodic relative to the matrix, and hence the material between the distributed phases were dissociated. In the areas other than the pits, the fine intermetallic particles still act as cathode to the matrix, and micro-pits are nucleated around such intermetallics (see the inset of Figure 5.11 (a)). In HAZ, the IGC and pits are observed along the grain boundaries due to the presence anodic  $Mg_2Si$ , which precipitated in this zone and totally dissolved in the NaCl solution (Figure 5.11 (b)) [13, 58]. The EDs analysis in B and C points depicts almost pure Al at the pit core and the corrosion products in HAZ (Table 5.4). The as welded ER4043 and FMg0.6 joints in the 2<sup>nd</sup> pass (exampled in Figure 5.11(c)), exhibit a dendritic structure susceptible to localized corrosion, a phenomenon consistently observed across all tested samples, particularly alongside eutectic Si and Fe-rich intermetallic phases (see Table 5.4) with minimal depth of penetration into the material [55]. The morphology of the pits in the 1<sup>st</sup> pass of the ER4043 and FMg0.6 joints was found to be resemble to the morphology in the 2<sup>nd</sup> pass. Figure 5.11 (e) illustrates a case of aggressive corrosion observed in as-welded ER5356. In this joint, pits are found not only at the dispersed  $\beta-Al_2Mg_3$  phase but also throughout the matrix, leading to the coalescence of these pits and sever damage to the FZ material.

Figure 5.11(d) represents the morphology of the pitting corrosion in the 1<sup>st</sup> and 2<sup>nd</sup> passes in the ER4043 and FMg0.6 joints after PWHT. The fine and spheroidized Si

particles as well as the fine Fe intermetallics lead to localized dissolving the matrix around such particles, as seen in the attached image in Figure 5.11 (d). Moreover, the larger Fe-rich intermetallic particles, the deeper pit formed around them (Figure 5.11 (d)). Figure 5.11 (f) examples the pitting corrosion in ER5356 in the PWHT condition, featuring a wider distribution, coalescence, and deeper pits compared to the as welded condition ( Figure 5.11 (d)). Additionally, the occurrence of IGC attributed to the presence of  $\beta$ -Al<sub>2</sub>Mg<sub>3</sub>, distinguishing it from ER4043 and FMg0.6 joints.

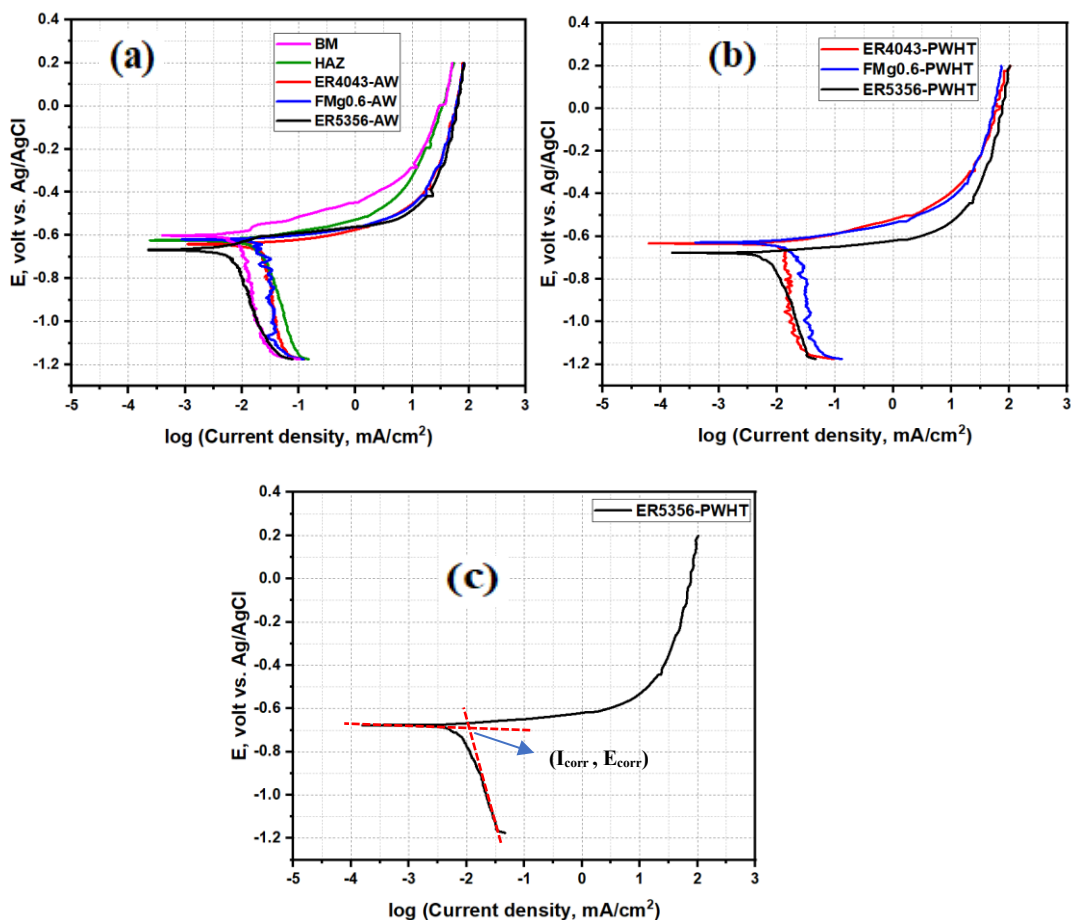


Figure 5.9. Potentiodynamic polarization curves (a) in as welded, (b) in PWHT conditions, and (c) an example shown The Tafel extrapolation for  $I_{\text{corr}}$  and  $E_{\text{corr}}$  estimation.

Table 5.3. The corrosion parameters from the potentiodynamic polarization test.

Sample	$E_{corr}$ (mV)	$I_{corr}$ ( $\mu\text{A}/\text{cm}^2$ )	Corrosion rate ( $\mu\text{m}/\text{y}$ )
BM	-602.91	2.23	24.31
HAZ	-623.2	10.42	113.58
ER5356-AW	-666.15	13.35	145.52
ER4043-AW	-635.02	7.19	78.37
FMg0.6-AW	-620.27	9.13	99.52
ER4043-HT	-630.07	5.51	60.06
FMg0.6-HT	-628.12	4.85	52.87
ER5356-HT	-680.35	16.4	178.76

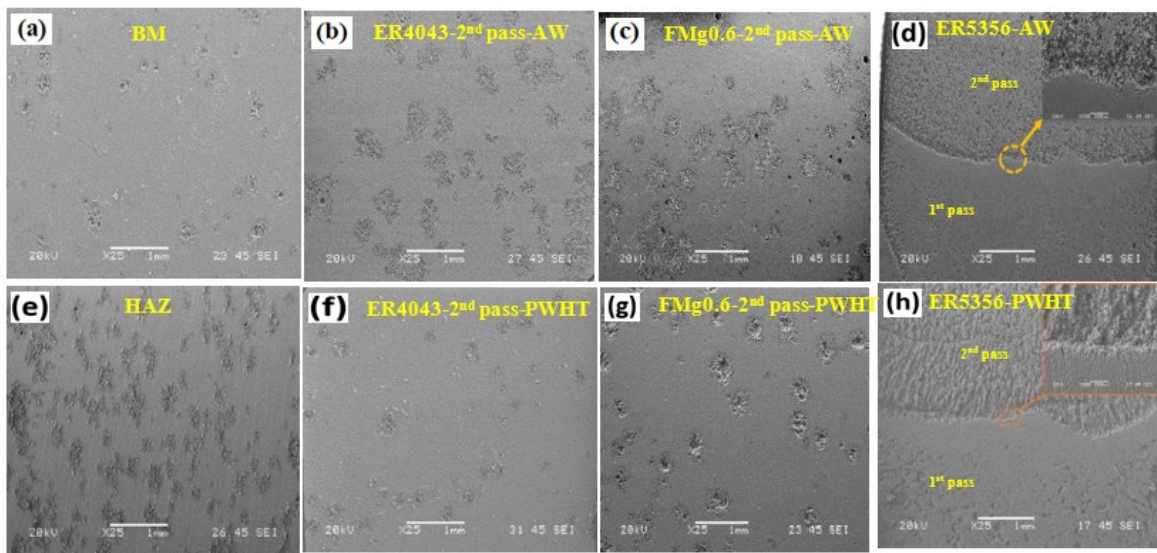


Figure 5.10. Macroscopic images of the pitting corrosion in the corroded surfaces of (a) the BM, (e) the HAZ, (b), (c) and (d) the welded joints in the as welded condition; (f), (g) and (h) the welded joints in in the PWHT condition.

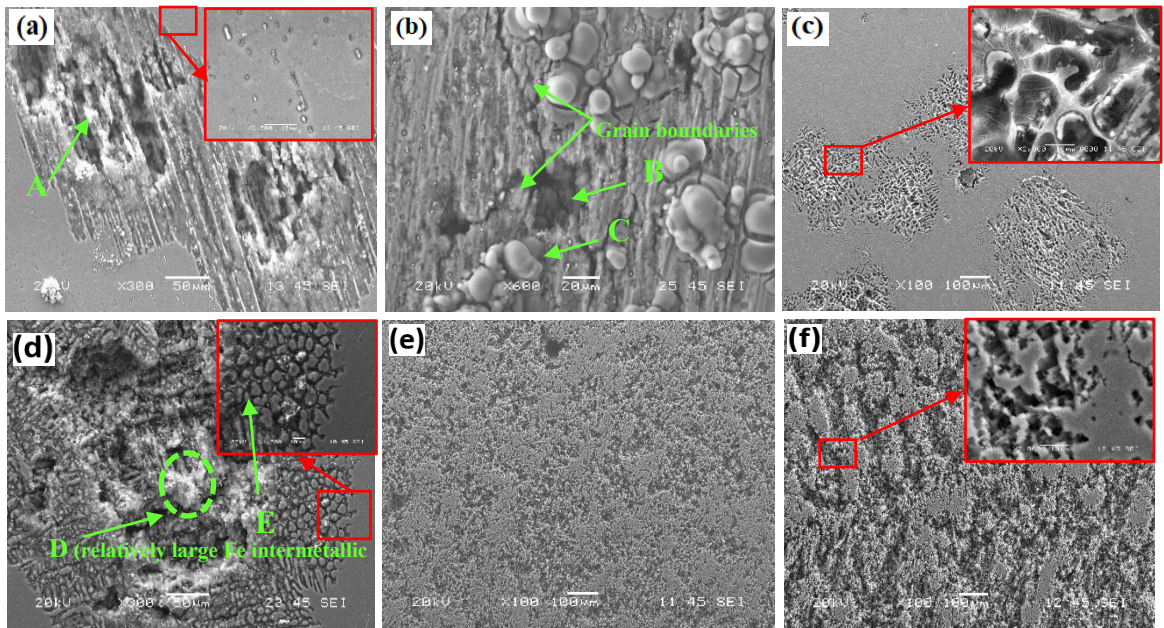


Figure 5.11. Surface morphology of pits after polarization in 3.5 wt.% NaCl solution, (a) BM, (b) HAZ, (c) and (d) 1st pass of ER4043 in as welded and PWHTed cases, respectively, (e) and (f) 2nd pass of FMg0.6 in as welded and PWHTed cases, respectively, and (g) 1st pass of ER5356 in PWHTed case.

Table 5.4. EDs analysis of the corroded BM, HAZ and welded joints

	Al	Si	Mg	Mn	Fe	Cu	O	Cl
<b>A</b>	63.32	2.12	1.1	-	-	2.53	30.93	-
<b>B</b>	100	-	-	-	-	-	-	-
<b>C</b>	27.35	-	-	-	-	-	52.61	20.05
<b>D</b>	73.8	6.09	-	2.01	2.57	-	15.54	-
<b>E</b>	82.19	4.28	-	-	-	-	13.53	-

### 5.3.5.3 The immersion test

The immersion test is a common method used to evaluate the corrosion behavior of welded aluminum alloys via the weight loss over a certain period. The weight losses from the immersion tests in the as welded condition are shown in Figure 5.12(a). The higher the weight loss, the lower the corrosion resistance achieved. The study examines weight loss in

welded joints through immersion tests. The BM had the lowest weight loss due to its high corrosion resistance, indicated by its high corrosion potential ( $E_{\text{corr}}$ ). The ER5356 welded joint exhibited the highest weight loss over time because its FZ acts as an anode relative to the BM and HAZ, leading to increased corrosion. This joint had significant potential differences between the BM and FZ ( $E_{\text{corr}}(\text{BM}) > E_{\text{corr}}(\text{FZ})$ ), and between the HAZ and FZ ( $E_{\text{corr}}(\text{HAZ}) > E_{\text{corr}}(\text{FZ})$ ), promoting corrosion as shown in Table 5.3. Conversely, the ER4043 and FMg0.6 joints initially showed lower weight loss compared to ER5356 with an increase over the period of 20 days due to the electrolyte corrosion. After 30 days, the weight loss of the ER4043 joint remained stable, and the FMg0.6 joint showed only a slight increase, possibly due to oxide layer formation [9, 59]. Lower potential differences between the BM and FZ in these joints contributed to less weight loss compared to the ER5356 joint.

Figure 5.12(b) shows the immersion test results in the PWHTed joints. The weight losses in all PWHTed joints are generally lower compared to the as welded condition, due to the removing effect of the HAZ and all HAZ become similar to the BM, and hence the reduction of the exposed anodic zone to be only the FZ. Moreover, the PWHT leads to modification of the microstructure by dissolving all the eutectic Mg<sub>2</sub>Si and spheroidization of the eutectic Si. This leads to reducing the microgalvanic cells between the phases and the matrix, hence lower corrosion potentials were obtained compared to the as welded condition (see Table 5.3). For each immersion period, the weight losses of the three joints are almost similar. This is because of the limited area of the anode (FZ), which leads to reduction of the diffusion rate of Al ions in the electrolyte, hence low Al oxidation kinetics [60]. The weight losses of all PWHTed joints ( $3 \pm 0.3$  mg) are lower than that of the BM ( $4 \pm 0.5$  mg) at the

immersion time of 10 days (see Figure 5.12(a) and (b)). This finding is attributed to the fact that the BM acts as cathode relative to the FZs and hence low weight loss in each joint due to low exposed anodic area (FZ). In the case of BM without welding, it acts no cathode, instead, large area is available for the general corrosion to occur. The weight loss increases with more time exposure as more time can give the chance for more Al oxidation.

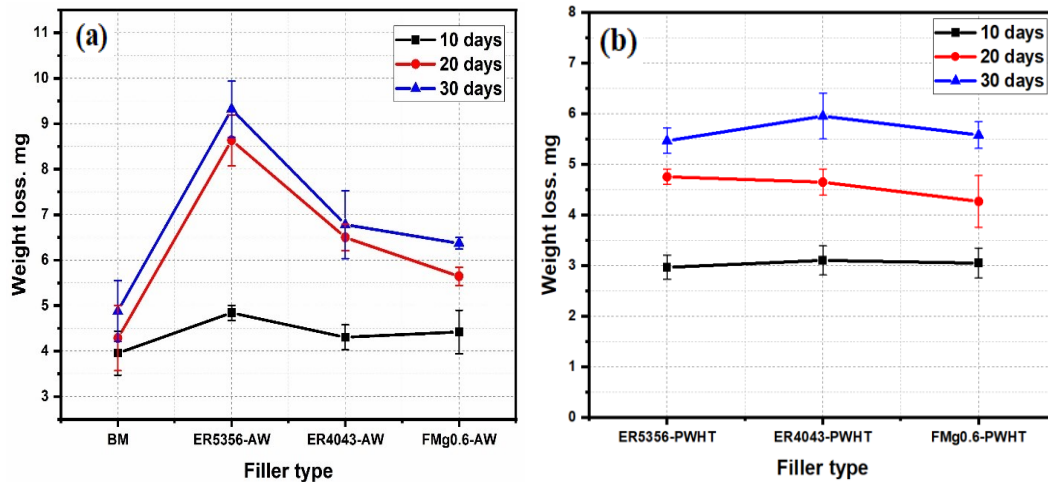


Figure 5.12. Results of the immersion corrosion tests (a) in as welded and (b) in PWHT conditions.

### 5.3.6 Discussion

The above results confirmed that the use of commercial ER4043 and ER5356 fillers for welding a high-strength AA6011 alloy resulted in inferior tensile and fatigue strengths. This is attributed to the low dilution and insufficient Mg content in the weldments of ER4043, along with the non-heat-treatable nature and presence of brittle  $\beta$ -Al<sub>2</sub>Mg<sub>3</sub> in ER5356 joint. The augmentation of Mg in FMg0.6 filler results in an increased Mg content in the FZ, leading to high solid solution strengthening, and hence high microhardness under the as welded condition. The strength of both ER5356 and FMg0.6 joints in their as welded

condition is primarily determined by the strength of the HAZ, where the high quantity of strengthening precipitates  $\beta''$ -MgSi dissolved due to the elevated welding temperature [38]. Consequently, FMg0.6 with a high Mg content does not significantly improve tensile strength under as welded condition compared to ER5356. In the case of as-welded ER4043 joint, tensile strength is marginally lower than that of as-welded FMg0.6 joint due to the relative low Mg content in the FZ. Regarding fatigue strength, FMg0.6 joint demonstrates superior performance compared to the commercial fillers due to its higher Mg content relative to ER4043 and the absence of brittle  $\beta$ -Al<sub>2</sub>Mg<sub>3</sub> phase presented in ER5356. In terms of corrosion properties, as-welded FMg0.6 exhibits better performance than ER5356 but slightly inferior to ER4043.

In comparison to the used commercial ER4043 and ER5356 fillers, the PWHTed FMg0.6 joint exhibited superior tensile strength relative to the used commercial fillers in the PWHT condition (see Figure 5.6(b)) due to precipitation of high number density of nano-scaled  $\beta''$ -MgSi in the FZ of FMg0.6 joint during PWHT. The lower strength in PWHTed ER4043 and ER5356 is attributed to low Mg content in the FZ and precipitation of the brittle  $\beta$ -Al<sub>2</sub>Mg<sub>3</sub>, respectively. FMg0.6 joint also showed the highest fatigue strength as well as the highest fatigue life compared to both commercial fillers. The highest fatigue properties of FMg0.6 joint is attributed to the high number density of the coherent precipitates  $\beta''$ -MgSi which hinder the dislocation movement and prolong the fatigue life [46]. The corrosion performance of both ER4043 and FMg0.6 joints is remarkably increased after PWHT because of dissolving the eutectic Mg<sub>2</sub>Si. While the PWHTed ER5356 suffers from high corrosion rate attributed to precipitation of the  $\beta$ -Al<sub>2</sub>Mg<sub>3</sub> at the grain boundaries, the

PWHTed FMg0.6 joint shows similar corrosion rate and weight loss relative to that of ER4043 joint. Therefore, the incorporation of 0.6% Mg in FMg0.6 significantly enhances both tensile and fatigue properties with satisfactory corrosion resistance when welding high-strength AA6011 joints.

#### 5.4 Conclusions

1. The ER4043 and FMg0.6 joints exhibited finer grain sizes in the fusion zone compared to ER5356 joint in the as welded condition. After the PWHT, the ER5356 joint exhibited the precipitation of the brittle  $\beta$ -Al<sub>2</sub>Mg<sub>3</sub> at the grain boundaries and inside of grains. In contrast, the ER4043 and FMg0.6 joints underwent spheroidization of eutectic Si and partial fragmentation of the Fe-rich intermetallics.
2. Due to the high Mg contents in the FZs, the as-welded ER5356 and FMg0.6 joints displayed higher microhardness and tensile strength compared to the ER4043 joints. Fractures in the former occurred in the softest HAZ, whereas the fracture in ER4043 joint happened in the FZ. After PWHT, the FMg0.6 joint presented the highest tensile strength among the three joints studied.
3. The FMg0.6 joint presented the highest fatigue strength and life compared to both ER4043 and ER5356 commercial joints in both as-welded and PWHT conditions, attributed to the modification of its composition with the added Mg. The striation widths of the PWHTed samples were in the order of FMg0.6 < ER4043 < ER5356,

indicating the lowest fatigue crack propagation rate in FMg0.6 joint. The fatigue strength and life of the PWHTed joints were significantly improved relative to their as-welded counterparts.

4. The ER5356 joint exhibited the lowest corrosion resistance among the three joints studied in all conditions. In the as welded state, the FMg0.6 joint displayed a slightly higher corrosion rate compared to ER4043 joint, attributable to a high-volume fraction of eutectic  $Mg_2Si$ . After PWHT, the corrosion resistances of both ER4043 and FMg0.6 joints were improved to the similar level.
5. Considering overall welding performance, including high tensile properties, superior fatigue strength and satisfactory corrosion resistance, the FMg0.6 joint outperformed the other two commercial ER4043 and ER5356 joints studied. As a result, the newly developed FMg0.6 filler wire emerges a promising filler metal for welding high strength 6xxx alloys.

## 5.5 References

1. Benedyk, J., Aluminum alloys for lightweight automotive structures. In *Materials, design and manufacturing for lightweight vehicles*, Elsevier: 2010; pp 79-113.
2. Sokoluk, M.; Yao, G.; Pan, S.; Cao, C.; Li, X., High Strength Nanotreated Filler Material for TIG Welding of AA6061. In *Light Metals 2020*, Springer: 2020; pp 380-385.
3. Verma, R. P.; Pandey, K.; Sharma, Y. Effect of ER4043 and ER5356 filler wire on mechanical properties and microstructure of dissimilar aluminium alloys, 5083-O and 6061-T6 joint, welded by the metal inert gas welding. *Proc Inst Mech Eng B J Eng Manuf*, **2015**, *229*, 1021-1028.
4. Fattahi, M.; Rostami, M.; Amirkhanlu, F.; Arabian, N.; Ahmadi, E.; Moayedi, H. J. D. Fabrication of aluminum TIG welding filler rods reinforced by ZrO<sub>2</sub>/reduced graphene oxide hybrid nanoparticles via accumulative roll bonding. *DRM*, **2019**, *99*, 107518.
5. [https://esab.com/ca/nam\\_en/esab-university/blogs/should-i-use-4043-or-5356-filler-alloy/](https://esab.com/ca/nam_en/esab-university/blogs/should-i-use-4043-or-5356-filler-alloy/).
6. Naing, T. H.; Muangjunburee, P. Metallurgical and mechanical characterization of MIG welded repair joints for 6082-T6 aluminum alloy with ER 4043 and ER 5356. *Trans. Indian Inst. Met.*, **2022**, *75*, 1583-1593.
7. Sokoluk, M.; Cao, C.; Pan, S.; Li, X. Nanoparticle-enabled phase control for arc welding of unweldable aluminum alloy 7075. *Nat. Commun*, **2019**, *10*, 98.
8. Bethea, J. F. Gas Tungsten Arc Welding of Aluminum Alloys with Nanocomposite 4943 Filler Material. master of engineering, University of California, Los Angeles, 2019.
9. Hu, Z.; Wan, L.; Lü, S.; Zhu, P.; Wu, S. Research on the microstructure, fatigue and corrosion behavior of permanent mold and die cast aluminum alloy. *Mater. Des.*, **2014**, *55*, 353-360.
10. Yan, S.; Xing, B.; Zhou, H.; Xiao, Y.; Qin, Q.-H.; Chen, H. Effect of filling materials on the microstructure and properties of hybrid laser welded Al-Mg-Si alloys joints. *Mater. Charact.*, **2018**, *144*, 205-218.
11. Bach, L.; Son, D.; Phong, M.; Thang, L.; Bian, M.; Nam, N. A study on Mg and AlN composite in microstructural and electrochemical characterizations of extruded aluminum alloy. *Compos. B. Eng.*, **2019**, *156*, 332-343.

12. Zhang, D.-Q. J., Xin Gao, Li-Xin Joo, Hyung Goun Lee, Kang Yong Effect of laser–arc hybrid welding on fracture and corrosion behaviour of AA6061-T6 alloy. *Mater. Sci. Eng. A* . **2011**, *528*, 2748-2754.
13. Majeed, T.; Mehta, Y.; Siddiquee, A. N. Precipitation-dependent corrosion analysis of heat treatable aluminum alloys via friction stir welding, a review. *Proc. Inst. Mech. Eng., Part C*, **2021**, *235*, 7600-7626.
14. Nam, N.; Dai, L.; Mathesh, M.; Bian, M.; Thu, V. Role of friction stir welding–traveling speed in enhancing the corrosion resistance of aluminum alloy. *Mater. Chem. Phys.*, **2016**, *173*, 7-11.
15. Osório, W. R.; Freire, C. M.; Garcia, A. The role of macrostructural morphology and grain size on the corrosion resistance of Zn and Al castings. *Mater. Sci. Eng. A* . **2005**, *402*, 22-32.
16. Rahman, A. M.; Kumar, S.; Gerson, A. Galvanic corrosion of laser weldments of AA6061 aluminium alloy. *Corros. Sci.*, **2007**, *49*, 4339-4351.
17. Donatus, U.; Thompson, G.; Omotoyinbo, J.; Alaneme, K.; Aribó, S.; Agbabiaka, O. Corrosion pathways in aluminium alloys. *Trans. Nonferrous Met. Soc. China*, **2017**, *27*, 55-62.
18. Fadaeifard, F. M., Khamirul Amin Garavi, Farhad Al-Falahi, Muath Sarrigani, Gholamreza Vahedi. Effect of post weld heat treatment on microstructure and mechanical properties of gas tungsten arc welded AA6061-T6 alloy. *Trans. Nonferrous Met. Soc. China*, **2016**, *26*, 3102-3114.
19. Haryadi, G. D.; Kim, S. J. Influences of post weld heat treatment on fatigue crack growth behavior of TIG welding of 6013 T4 aluminum alloy joint (Part 1. Fatigue crack growth across the weld metal). *J. Mech. Sci. Technol*, **2011**, *25*, 2161-2170.
20. Ahmed, M.; Javidani, M.; Mirakhorli, F.; Maltais, A.; Chen, X. G. Developing High-Strength Al-Si-Mg Filler Metals for Aluminum Fusion Welding. *J. Mater. Eng. Perform.*, **2023**, *32*, 2218-2227.
21. Peng, W. W., Guangxin Lu, Rui Lian, Quanyong Zhang, Jieyu The Evaluation on Corrosion Resistance and Dross Formation of Zn–23 wt% Al–0.3 wt% Si–x wt% Mg Alloy. *Coatings* **2019**, *9*, 199.
22. Lumsden, J.; Mahoney, M.; Pollock, G. In *Corrosion behavior of friction stir welded high strength aluminum alloys*, Proc. Tri-Service Corrosion Conf., Defense Technical Information Center Complication Part Notice ADP015941, San Antonio, TX, USA, 2002; pp 296-307.
23. Ma, R. F., K Yang, JG Liu, XS Fang, HY Grain refinement of HAZ in multi-pass welding. *J. Mater. Process. Technol.*, **2014**, *214*, 1131-1135.

24. Lezaack, M. B.; Simar, A. Avoiding abnormal grain growth in thick 7XXX aluminium alloy friction stir welds during T6 post heat treatments. *Mater. Sci. Eng. A* . **2021**, *807*, 140901.
25. Wang, B.; Xue, S.; Ma, C.; Wang, J.; Lin, Z. Effects of porosity, heat input and post-weld heat treatment on the microstructure and mechanical properties of TIG welded joints of AA6082-T6. *Metals*, **2017**, *7*, 463.
26. Easton, M. A. S., David H Improved prediction of the grain size of aluminum alloys that includes the effect of cooling rate. *Mater. Sci. Eng. A* . **2008**, *486*, 8-13.
27. Wang, B. Z., Mingshan Wang, Junsheng. Quantifying the effects of cooling rates and alloying additions on the microporosity formation in Al alloys. *Mater. Today Commun.*, **2021**, *28*, 102524.
28. Leo, P.; Renna, G.; Casalino, G.; Olabi, A. Effect of power distribution on the weld quality during hybrid laser welding of an Al–Mg alloy. *Opt. Laser Technol.*, **2015**, *73*, 118-126.
29. Leo, P.; D'Ostuni, S.; Casalino, G. Hybrid welding of AA5754 annealed alloy: Role of post weld heat treatment on microstructure and mechanical properties. *Mater. Des.*, **2016**, *90*, 777-786.
30. Ahmed, M.; Javidani, M.; Maltais, A.; Chen, X.-G. Welding of AA6061-T6 Sheets Using High-Strength 4xxx Fillers: Effect of Mg on Mechanical and Fatigue Properties. *Materials*, **2023**, *16*, 3832.
31. Seifeddine, S.; Svensson, I. L. The influence of Fe and Mn content and cooling rate on the microstructure and mechanical properties of A380-die casting alloys. *Metall. Res. Technol.*, **2009**, *27*.
32. Choi, I.-K.; Cho, S.-H.; Kim, S.-J.; Jo, Y.-S.; Kim, S.-H. Improved corrosion resistance of 5xxx aluminum alloy by homogenization heat treatment. *Coatings*, **2018**, *8*, 39.
33. Lin, Y.-K. W., Shing-Hai Chen, Ren-Yu Hsieh, Tso-Sheng Tsai, Liren Chiang, Chia-Chin. The effect of heat treatment on the sensitized corrosion of the 5383-H116 Al-Mg alloy. *Materials*, **2017**, *10*, 275.
34. Kumar, S.; Grant, P. S.; O'Reilly, K. A. Q. Fe bearing intermetallic phase formation in a wrought Al–Mg–Si alloy. *Trans. Indian Inst. Met.*, **2012**, *65*, 553-557.
35. Moustafa, M. A. Effect of iron content on the formation of  $\beta$ -Al<sub>5</sub>FeSi and porosity in Al–Si eutectic alloys. *Mater. Process. Technol.*, **2009**, *209*, 605-610.

36. Ahmed, M.; Javidani, M.; Maltais, A.; Chen, X.-G. Microstructure and Mechanical Properties of High-Strength AA6011 Aluminum Alloy Welding with Novel 4xxx Filler Metals. *Materials*, **2024**, *17*, 380.
37. Oskouei, R. H.; Ibrahim, R. The effect of a heat treatment on improving the fatigue properties of aluminium alloy 7075-T6 coated with TiN by PVD. *Procedia Eng.*, **2011**, *10*, 1936-1942.
38. Pérez, J. S.; Ambriz, R. R.; López, F. F. C. Recovery of mechanical properties of a 6061-T6 aluminum weld by heat treatment after welding. *Metall. Mater. Trans. A*, **2016**, *47*, 3412-3422.
39. Poznak, A.; Freiberg, D.; Sanders, P., Automotive wrought aluminium alloys. In *Fundamentals of aluminium metallurgy*, Elsevier: 2018; pp 333-386.
40. Liu, K.; Algendy, A.; Gu, J.; Chen, X.-G. In *Evolution of Microstructure and Dispersoids in Al-Mg 5xxx Alloys Under Wire+ Arc Additive Manufacturing and Permanent Mold Casting*, TMS 2021 150th Annual Meeting & Exhibition Supplemental Proceedings, 2021; Springer: pp 165-175.
41. Ha, S. H.; Yoon, Y. O.; Kim, S. K. In *Effects of Si Addition on the Microstructure and Tensile Property of Al-xMg Alloys with Al<sub>2</sub>Ca during Heat Treatment (x: 5 and 7 Mass%)*, Mater. Sci. Forum, 2017; Trans Tech Publ: pp 109-113.
42. Johannesson, B.; Cáceres, C. Effect of Si additions and heat treatment on the mechanical behaviour of an Al-5Mg casting alloy. *Int. J. Cast Met. Res.*, **2004**, *17*, 94-98.
43. Coniglio, N.; Cross, C. E.; Michael, T.; Iammers, M. Defining a critical weld dilution to avoid solidification cracking in aluminum. *Weld. J.*, **2008**, *87*, 237s-247s.
44. Mousavi, M. G.; Cross, C. E.; Grong, Ø.; Hval, M. Controlling weld metal dilution for optimised weld performance in aluminium. *Sci. Technol. Weld. Joining*, **1997**, *2*, 275-278.
45. Wen, W.; Zhao, Y.; Morris, J. G. The effect of Mg precipitation on the mechanical properties of 5xxx aluminum alloys. *Mater. Sci. Eng., A*, **2005**, *392*, 136-144.
46. Liu, H.; Yang, S.; Xie, C.; Zhang, Q.; Cao, Y. Microstructure characterization and mechanism of fatigue crack initiation near pores for 6005A CMT welded joint. *Mater. Sci. Eng., A*, **2017**, *707*, 22-29.
47. Ma, M. L., Ruilin Qin, Jin Wang, Bin Liu, Huiqun Yi, Danqing. Effect of weld reinforcement on tensile and fatigue properties of 5083 aluminum metal inert gas (MIG) welded joint: Experiments and numerical simulations. *Int. J. Fatigue*, **2021**, *144*, 106046.

48. Ren, L.; Gu, H.; Wang, W.; Wang, S.; Li, C.; Wang, Z.; Zhai, Y.; Ma, P. Effect of Mg content on microstructure and properties of Al–Mg alloy produced by the wire arc additive manufacturing method. *Materials*, **2019**, *12*, 4160.
49. Zhang, D.-Q.; Li, J.; Joo, H. G.; Lee, K. Y. Corrosion properties of Nd: YAG laser–GMA hybrid welded AA6061 Al alloy and its microstructure. *Corros. Sci.*, **2009**, *51*, 1399-1404.
50. Badawy, W. A. A.-K., FM El-Azab, AS. Electrochemical behaviour and corrosion inhibition of Al, Al-6061 and Al–Cu in neutral aqueous solutions. *Corros. Sci.*, **1999**, *41*, 709-727.
51. Won, S. S., Bosung Park, Jong Min Kim, Hyo Kyu Song, Kuk Hyun Min, Seok-Hong Ha, Tae Kwon Park, Kwangsuk Corrosion behaviors of friction welded dissimilar aluminum alloys. *Mater. Charact.*, **2018**, *144*, 652-660.
52. Adeosun, S.; Sekunowo, O.; Balogun, S.; Obiekea, V. Corrosion behaviour of heat-treated aluminum-magnesium alloy in Chloride and exco environments. *Int. J. Corros.*, **2012**, *2012*.
53. Wei, R. P.; Liao, C.-M.; Gao, M. A transmission electron microscopy study of constituent-particle-induced corrosion in 7075-T6 and 2024-T3 aluminum alloys. *Metall. Mater. Trans. A*, **1998**, *29*, 1153-1160.
54. Gupta, R. K. Z., Ruifeng Davies, Chris Huw John Birbilis, Nick. Influence of Mg content on the sensitization and corrosion of Al-xMg (-Mn) alloys. *Corrosion*, **2013**, *69*, 1081-1087.
55. Nikseresht, Z.; Karimzadeh, F.; Golozar, M.; Heidarbeigy, M. Effect of heat treatment on microstructure and corrosion behavior of Al6061 alloy weldment. *Mater. Des.*, **2010**, *31*, 2643-2648.
56. Abuaisa, R., *Corrosion behaviour of friction stir welded AA5xxx aluminium alloys*. The University of Manchester (United Kingdom): 2013.
57. Chen, G. C., Qiang Wang, Bo Du, Zhi-ming. Microstructure evolution and tensile mechanical properties of thixoformed high performance Al-Zn-Mg-Cu alloy. *Metals and Materials International*, **2015**, *21*, 897-906.
58. Xie, W. H., Te Yang, Chunli; Fan, C.; Lin, S.; Xu, W. Comparison of microstructure, mechanical properties, and corrosion behavior of Gas Metal Arc (GMA) and Ultrasonic-wave-assisted GMA (U-GMA) welded joints of Al–Zn–Mg alloy. *J. Mater. Process. Technol.*, **2020**, *277*, 116470.
59. Zaid, B.; Saidi, D.; Benzaid, A.; Hadji, S. Effects of pH and chloride concentration on pitting corrosion of AA6061 aluminum alloy. *Corros. Sci.*, **2008**, *50*, 1841-1847.

60. Cramer, S. C. J., BS Corrosion: Fundamentals, Testing, and Protection, Volume 13A, ASM Handbook. *J. Therm. Spray Technol.*, **2003**, 12, 459.

## 6. Chapter 6: General conclusions and recommendations

### 6.1 General Conclusions

In this project, the composition of the commercial filler, ER4043 was modified via different contents of Mn and Mg. The modified fillers were used to weld two BMs of different thicknesses, AA6061-T6 (2 mm) and AA6011-T6 (6 mm). In addition, the commercial fillers such as ER4043, ER4943, and ER5356 were utilized to compare and test the welding performance and the mechanical properties of the new fillers.

- The new Al-Si-Mg 4xxx filler metals exhibited weldability similar to that of the ER4043 commercial filler in welding thin and thick 6xxx BMs. The Mg contents in the FZs of the new fillers were much higher than that of the reference fillers due to increasing Mg content in the new fillers. Furthermore, welding thick AA6011 BM through multiple passes, enhance the Mg and Mn contents in the Al-Si-Mg 4xxx filler metals led to a substantial increase in the alloying elements within the FZ compared to the ER4043 and ER4943 reference fillers.
- In the as-welded condition, the joint of ER4043 with AA6011 BM experienced fracture within the FZ. While all the as-welded samples with all BMs demonstrated comparable mechanical strength, it was notably lower than that of the BM. The strength of the FZs surpassed the minimum strength of the HAZ for any given filler. Consequently, all the welded samples exhibited fractures at the HAZ, identified as the weakest zone in the joints due to recrystallization and the dissolution/coarsening of strengthening precipitates.
- In the PWHTed joints of AA6061 BM, the mechanical strength of all joints, regardless of the Mg content, reached the same level as the BM, achieving 100%

welding efficiency in the joints of AA6061 BM. While the joints of the AA6011 BM were developed to higher strength relative to the as welded conditions but lower than the BM strength. The strength of the newly developed fillers gives the same strength level with average efficiency of 91.5%. The high Mg contents in the new fillers supported the precipitation of a high-volume fraction of fine  $\beta''$ -MgSi in the FZ during PWHT, leading to enhanced strength and superior welding efficiency compared to the reference fillers.

- In the joints of AA6061 BM, the joints made by novel fillers with high Mg content (0.6-1.4 wt.%) displayed higher fatigue strengths and longer fatigue lives compared to the joint made by the reference filler in both as welded and PWHT conditions. The joint with the filler containing 1.4 wt.% Mg exhibited the highest fatigue strength and best fatigue life. While in the joints of AA6011 BM, The FMg0.6 joint presented the highest fatigue strength compared to the commercial joints in the as welded and PWHT condition as result of the modification of its composition with the added Mg.
- The Porosity in the FZs of AA6061 BM negatively impacted fatigue life, with joints using novel fillers exhibiting longer fatigue lives for small pore sizes and the influence of porosity becoming dominant for large pore sizes, regardless the Mg content. In all BMs, the porosity close to the sample surface were identified as a significant factor in porosity-related crack initiation during cyclic loading. PWHT revealed clear slip bands and fatigue striation in the welding zone, with the joint using the novel filler containing higher Mg contents displaying narrower striation

width, indicative of a lower crack propagation rate and a longer fatigue life compared to the reference filler joint.

- In the joints of AA6011 BM, the optimal Mg content for the filler was found to be 0.6 wt.% (FMg0.6 filler), with high tensile strength but a decrease in the elongation. FMg0.6 exhibited complete dissolution of  $Mg_2Si$  particles after PWHT, while those with 1.4% Mg retained undissolved  $Mg_2Si$  due to the Mg solubility limit. The higher the Mg in the newly developed fillers, the lower the impact toughness in the welded joints was found. The PWHT enhanced the impact toughness compared to the as-welded condition, however, lower than that of the joints of the reference fillers.
- The ER5356 joint exhibited the lowest corrosion resistance in all conditions. In the as-welded state, the FMg0.6 joint displayed a higher corrosion rate than the ER4043 joint due to the elevated volume fraction of primary  $Mg_2Si$ . Following PWHT, the corrosion resistances of ER4043 and FMg0.6 joints improved because of the homogenized distribution of precipitates within the FZs and the removal of the HAZ. In the PWHT condition, both ER4043 and FMg0.6 joints demonstrated similar corrosion resistance, hence the FMg0.6 is a promising filler regarding to the mechanical and the corrosion properties.

## 6.2 Recommendations

In this project, the effect of modification of the commercial ER4043 composition with Mg and Mn was systematically investigated. The welding performance was found to be the same as the commercial fillers in the thin and thick 6xxx BMs. Furthermore, the efficiency in welding the thin AA6061 reached 100% of this BM strength. However, there yet remains several additional issues that are worth investigating. The following recommendations can be drawn for future work in this field:

- The elongation and the impact toughness with using the high Mg fillers was reduced relative to that of the reference fillers. Therefore, modification of the new filler composition with the Sr can lead to modification of the eutectic Si and hence improving the joint elongation and the impact toughness in all conditions. Moreover, the corrosion resistance is expected to be improved due to reduction of the Si particle size.
- Moreover, using the new fillers with the high strength and thick BM, AA6011, gave a maximum efficiency of 93.5% with the filler of FMg0.6. The latter mentioned efficiency is good relative to the reference fillers, however, better efficiency with joint strength closer to that of the high BM strength is required in the industrial scale. So, further modification along with the Mg addition can improve the welding efficiency. This modification can be addition of nanoscale ceramic particles of the TiC or Al<sub>2</sub>O<sub>3</sub>.

- In this study, AA6011 BM with 6 mm thickness was used. The results showed that the rich new fillers with Mg have compensated for the reduction of the BM dilution, especially in the second pass. However, more progressive passes (such as the third and fourth passes) in thick and high strength BMs suffer from nil dilution. Therefore, another check can be done with using higher thickness AA6011 BM such as 9 or 12 mm thicknesses for more revealing the effect of the new fillers in welding ultra thicker BMs.
- Finally, the newly developed fillers illustrated high welding efficiency and high mechanical properties with the BMs of 6xxx aluminum alloys. However, using high strength 7xxx was not involved in this study. Therefore, trying welding this BM series with the newly developed fillers can reveals their advantages and limitations (if found) with the 7xxx BMs.

**Appendix I:** The general description of the newly developed fillers wires fabrication

The newly developed fillers were fabricated by using the steps in figure I.1. Billets with 100 mm diameter was DC cast. Then the billets were cut into small billets with suitable length of 200 mm. Next, the heat treatment starts with homogenization for 10 hr at 530 °C followed by cooling with the rate of 350 °C/hr. before starting the extrusion process, the billets were rapidly reheated in an induction furnace in about 1 min. to reach a final temperature of 510 °C. finally the heated billets were extruded into filler wires with a diameter of 1.5 mm.

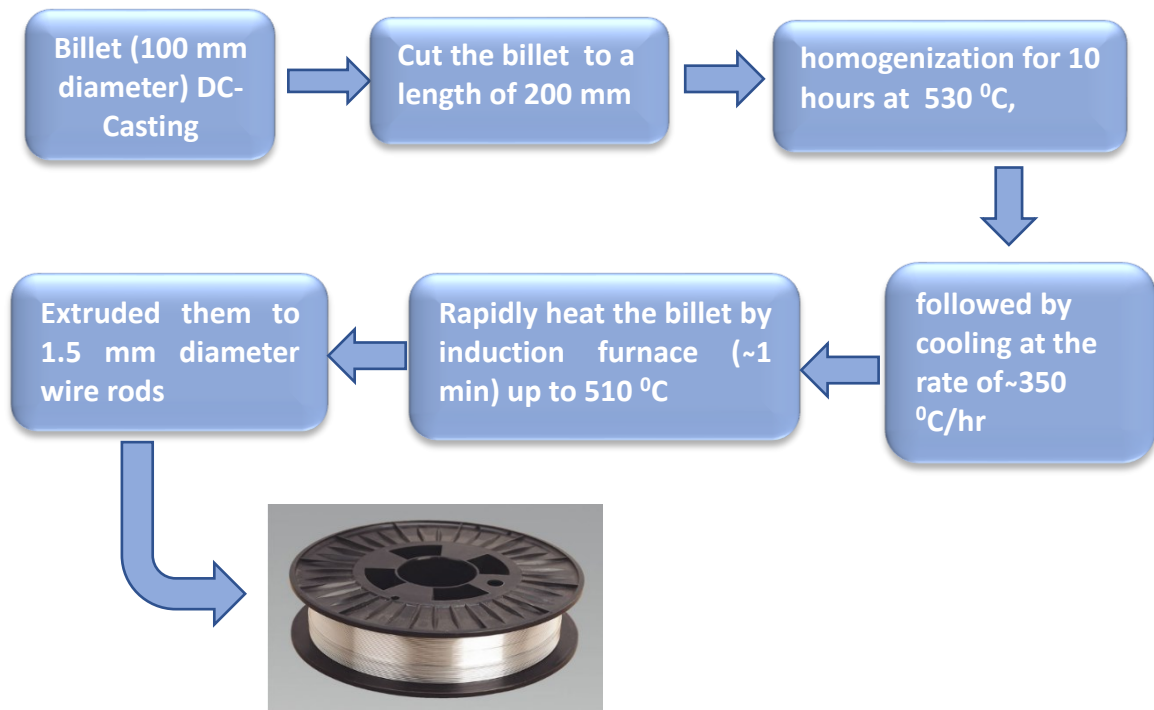


Figure I.1. the manufacturing procedures of the newly developed fillers wires

**Appendix II:** The correlation of the strength in parts I and II.

To verify the strength of the FZ, a new method was developed as the standard sample was fractured away from the FZ. So, a new modified tensile sample with double edges round notch in the FZ, was used as shown in the chapter 2 (Figure 2.2(b)). The samples with the modification were fractured at the center of the FZ ( see Figure 2.11(b)). It is impossible to estimate average true stress-logarithmic true strain data beyond the onset of the diffuse necking. After the onset of necking, a nonuniform deformation field, called plastic instability, starts to develop just after a maximum load. The stress state and deformation in the necked region are analogous to those in the notch of a circumferentially notched tensile specimen. After a non-uniform deformation field develops in the necked region of a tensile specimen, an analytic solution is used for true stress. After applying the correction to the true stress, the corrected true stress –strain curve can be converted to the engineering stress-strain curve just up to the maximum load. By applying a correction on the true stress according to equations (1) and (2) [59].

$$\zeta(\varepsilon_p) = \begin{cases} 1 & \text{for } \varepsilon_p \leq 1.4n \\ \alpha\varepsilon_p^2 + \beta\varepsilon_p + \gamma & \text{for } \varepsilon_p > 1.4n \end{cases}$$

$$\alpha = -0.0704n - 0.0275$$

$$\beta = 0.4550n - 0.2926$$

$$\gamma = 0.1592n + 1.024$$

Eq (1)

$$\sigma_{eq} = \sigma_{a.av} \zeta(\varepsilon_p)$$

Eq (2)

Where  $\zeta$  represents the correction factor as a function of the true plastic strain,  $\epsilon_p$ , and  $n$  is the strain hardening exponent.  $\sigma_{eq}$  is the true stress after correction.  $\sigma_{a,av}$  is the true stress calculated from the tensile machine. Then according to Figure II.1, the engineering strain at max. load is higher than any monitored strain for all samples. So, with conversion all engineering strains to true strains, the true strain at the max. load will be higher than any true strains. As the strain hardening exponent is equal to the true strain at the max. load, the value of  $1.4n$ , for all curves in as welded and PWHT condition, is higher than the plastic strain  $\epsilon_p$ . So, based on equation (1), the correction factor,  $\zeta$ , can be considered as one. Based on this result, the engineering stress-strain can be calculated directly from the tensile machine.

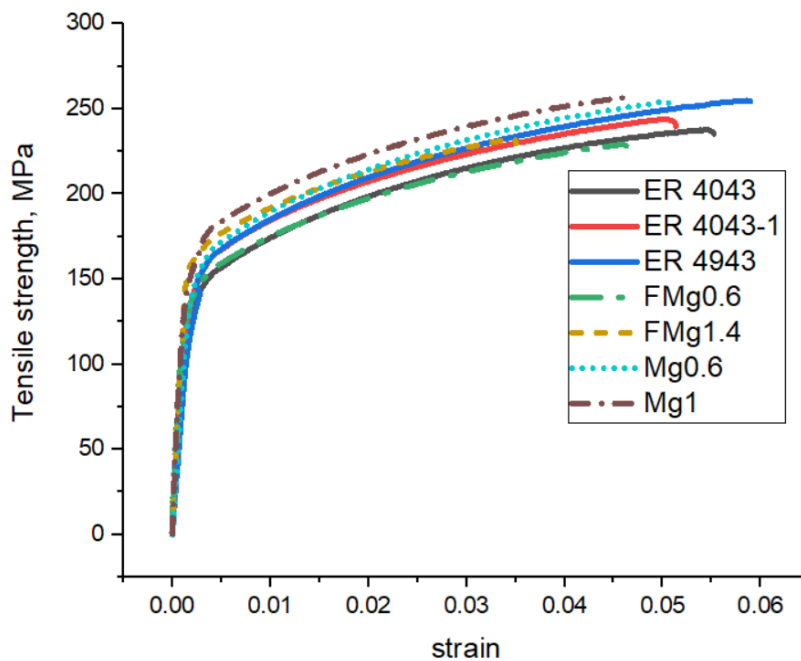


Figure II.1. Stress-strain curves of the FZs in the as welded condition (AA6061-T6 BM).

**Appendix II** : support chapter 3 and chapter 4,

**1. The BM (AA6011-T6) fabrication**

**a. DC casting of Billet with dimensions :**

- Length : 405 mm
- Diameter : 101.6 mm (4'')

**b. Casting parameters:**

- Number of billets cast per drop : 4
- Metal temperature : 730 °C
- Casting speed : 120 mm/min.

**c. Homogenization heat treatment:**

- Soak time: 3h
- Soak temperature: 560 °C
- Cooling rate: Fast air cool

**d. Extrusion parameters:**

- Target preheat temperature: 500 °C
- Ram speed: 8 mm/s
- Exit speed : 10 m/min
- Butt length : 36 mm
- Extrusion ratio : 20
- Plate dimensions : 75 x 6 mm
- No stretching after extrusion

**e. Aging:**

- 24 hr natural aging minimum
- Soak time : 8 hr
- Soak temperature : 177 °C

## 1. The BM (AA6011-T6) and welding wires cleaning prior to the welding

- After machining the edges of the BM plates, cleaning of the BM was done according to the following procedures in the order:
  - a. Cleaning with acetone to remove any grease.
  - b. Removing of oxides will be removed using stainless steel brush
  - c. Re-cleaning with acetone prior to the welding.
  - d. The BM was welded within less than 5 hours after finishing the cleaning procedures.
  
- For Filler metals preparation, the rest of the extruded wires from the previous part of the welding project were used in this study . Due to long storage of the filler wires (about 14 months), degreasing and oxide removal were applied according to the following procedures.
  - a. The filler wires were pickled in a cleaning reagent (50% water + 50% HNO<sub>3</sub>) at room temperature for 15 min.
  - b. Then the pickled wires were rinsed with warm water, then dried in the air.
  - c. For removing the humidity, Filler wires were stored in the oven with controlled atmosphere of zero humidity at 30- 40 °C for 5 hours to reduce the contamination of humidity.
  - d. Prior to welding, the wires were cleaned by acetone.

## List of Publications

### JOURNAL ARTICLES

1. Ahmed, M., Javidani, M., Mirakhorli, F., Maltais, A., & Chen, X. G. (2023). Developing High-Strength Al-Si-Mg Filler Metals for Aluminum Fusion Welding. **Journal of Materials Engineering and Performance**, 32(5), 2218-2227, doi: 10.1007/s11665-022-07286-2.
2. Ahmed, M., Javidani, M., Maltais, A., & Chen, X. G. (2023). Welding of AA6061-T6 Sheets Using High-Strength 4xxx Fillers: Effect of Mg on Mechanical and Fatigue Properties. **Materials**, 16(10), 3832, doi.org/10.3390/ma16103832.
3. Ahmed, M., Javidani, M., Maltais, A., & Chen, X. G (2024). Microstructure, and mechanical properties of high-strength AA6011 aluminum alloy welding with novel 4xxx filler metals. **Materials**,17(2), 380, doi: org/10.3390/ma17020380
4. Ahmed, M., Javidani, M., Maltais, A., & Chen, X. G. Comparison of Mechanical, Fatigue and Corrosion Properties of Fusion-Welded AA6011-T6 Plates Using Three Filler Wires, **under the internal review**.

### CONFERENCE PAPERS

1. Ahmed, M., Javidani, M., Mirakhorli, F., Maltais, A., & Chen, X. G. (2023, August). Novel High-Strength Al-Si-Mg Filler Wires for Aluminum Welding. In Conference of Metallurgists (pp. 331-340). Cham: Springer Nature Switzerland.

### ***SCIENTIFIC POSTERS***

1. The effect of alloying elements on the mechanical and chemical properties of 4xxx filler alloys for aluminum welding, (REGAL 2019).
2. The impact of Mn and Mg content on mechanical properties and performance of 4xxx Al alloys weld wires, (REGAL 2020).
3. On the development of high-performance filler materials for fusion welding of aluminum-based alloys, (REGAL 2021).
4. Developing novel 4xxx filler metals for aluminum welding: impact of Mn and Mg on microstructure evolution and mechanical properties, (REGAL 2022).